Tampere University

Joona Rissanen

DESIGN OF A CHIRPED PULSE AMPLIFICATION SYSTEM BASED ON TAPERED FIBER AMPLIFIER

Master of Science Thesis
Faculty of Engineering and Natural Sciences
Examiners: Dr. Regina Gumenyuk
Dr. Valery Filippov
April 2020

ABSTRACT

Joona Rissanen: Design of a Chirped Pulse Amplification System based on Tapered Fiber Amplifier
Master of Science Thesis
Tampere University
Master's Degree Programme in Science and Engineering
April 2020

High-power ultrafast lasers are novel tools with plenty of potential applications, especially in materials processing. Fiber lasers, in particular, can fulfill the robustness, cost-efficiency and high-average-power requirements of industrial operation. However, nonlinear effects such as self-phase modulation and stimulated Raman scattering severely limit the peak power available directly from a normal fiber amplifier. The primary way to overcome these limitations is chirped pulse amplification in which a weak seed pulse is first temporally stretched, then amplified, and finally recompressed to ultrashort duration. Additionally, peak power can be scaled up by using an active fiber with large effective mode area but that causes new difficulties in obtaining single-mode beam quality. A simple technique to avoid those problems is to use a tapered double-clad fiber, whose core size grows from standard single-mode dimensions to multiple times larger towards the output while maintaining fundamental mode operation throughout.

This thesis describes a laser system design relying on both of these techniques, tapered double-clad fiber and chirped pulse amplification, to generate high-peak power pulses at 1 µm. The laser system includes an experimentally built semiconductor saturable absorber mirror mode-locked polarization maintaining fiber seed laser at 1040 nm and a numerically investigated amplifier chain, including a tunable chirped fiber Bragg grating stretcher, a pulse picker, two single-mode preamplifiers, a tapered power amplifier and a transmission grating compressor. The seed laser's ring cavity is based on numerous iterations of experimental testing with different intra-cavity filters, fiber lengths and output coupling ratios to obtain a broad spectrum. The design of the rest of the chirped pulse amplification system is based on practical experience with tapered fiber amplifiers and theoretical calculations. This thesis covers the choices and compromises relevant to each element in the laser system in detail.

The numerical model developed for the dispersive elements and the fiber amplifiers combines both rate equation simulations to compute gain and generalized nonlinear Schrödinger equation simulations to handle ultrafast pulse propagation in optical fibers. Using that model, the seed pulses are propagated sequentially through each component and fiber piece in the amplifier chain and finally, through the compressor with the aim of maximizing peak power at the output. A direct comparison to experimental results is still pending, but the model appears to give physically sensible results in the limited cases where a comparison is possible to similar fiber amplifiers tested in the past.

The main limitation of the developed chirped pulse amplification system is revealed by the simulations to be self-phase modulation in the tapered power amplifier, especially when combined with the irregular pulse shape from stretching the experimental seed laser pulse. The resulting complicated nonlinear phase shift cannot be properly compensated in the compressor, which leads to strong side pulses. Using Gaussian seed pulses with 5.4 nm spectral width, the numerical model predicts that the chirped pulse amplification system can generate 52 µJ, 480 fs pulses at a B-integral of 12.4 rad.

Keywords: chirped pulse amplification, fiber laser, ultrashort pulses, tapered double-clad fiber

TIIVISTELMÄ

Joona Rissanen: Venytettyjen pulssien vahvistusjärjestelmä perustuen paksunevaan valokuituvahvistimeen
Diplomityö
Tampereen yliopisto
Teknis-luonnontieteellinen tutkinto-ohjelma
Huhtikuu 2020

Ultranopeilla suurteholasereilla on monia potentiaalisia sovelluskohteita erityisesti materiaalintyöstössä, jossa niiltä vaaditaan luotettavuutta, kustannustehokkuutta ja mahdollisimman suurta keskiarvotehoa. Kaikkiin näihin vaatimuksiin pystyvät vastaamaan varsinkin kuitulaserit. Suoraan kuitulaserista tai -vahvistimesta saatavaa piikkitehoa rajoittavat kuitenkin ankarasti epälineaariset ilmiöt kuten itseisvaihemodulaatio (self-phase modulation) ja stimuloitu Raman-sironta. Tärkein menetelmä näiden rajoitusten ohittamiseksi on venytettyjen pulssien vahvistustekniikka (chirped pulse amplification), jossa sisään tuleva heikko pulssi ensin venytetään pidemmäksi aikatasossa, sitten vahvistetaan ja lopulta kompressoidaan takaisin ultralyhyeen mittaansa. Tämän lisäksi piikkitehoa voi kasvattaa entisestään käyttämällä vahvistimessa moodin pinta-alaltaan suurta valokuitua, mikä kuitenkin vaikeuttaa yksimuotoisen säteenlaadun aikaansaamista. Yksinkertainen tekniikka tämän ongelman ratkaisemiseksi on paksuneva kaksivaippainen valokuitu (tapered double-clad fiber), jonka ytimen koko kasvaa pituussuunnassa yksimuotokuidun mitoista moninkertaiseksi tultaessa ulostuloa kohti säteen säilyessä samalla täysin yksimuotoisena.

Tämä diplomityö kuvailee lasersysteemin, joka hyödyntää näitä molempia tekniikoita suuren piikkitehon pulssien tuottamiseen 1 µm aallonpituudella. Systeemi sisältää kokeellisesti rakennetun muotolukitun kuitulaserin 1040 nm aallonpituudella perustuen saturoituvasti absorboivaan puolijohdepeiliin (SESAM) ja polarisaation säilyttäviin valokuituihin. Pulssien lähteenä toimivan laserin lisäksi systeemiin kuuluu numeerisilla simulaatioilla testattu kuituvahvistinketju sisältäen säädettävän kuitu Braggin hila venyttäjän, nopean optisen kytkimen toistotaajuuden laskemiseen, kaksi yksimuotokuituesivahvistinta, paksunevasta valokuidusta tehdyn tehovahvistimen sekä läpäisyhilakompressorin. Kokeellisen laserlähteen rengaskaviteetin komponentit kuten kapea suodin (band pass filter), ulostulon suuruus ja kuitujen mitat on valittu kattavan kokeellisen testauksen jälkeen leveäspektristen pulssien tuottamiseksi. Vahvistinosan suunnitelma taas perustuu kokemukseen vastaavien vahvistinten kanssa työskentelystä sekä teoreettisiin laskelmiin. Suunnitelmassa tehdyt valinnat ja kompromissit käydään tässä työssä yksityiskohtaisesti läpi.

Dispersiivisille komponenteille ja kuituvahvistimille kehitetty numeerinen malli yhdistää aktiivikuidun vahvistusta kuvaavat yhtälöt ja yleistetyn epälineaarisen Schrödinger-yhtälön pulssien etenemisen kuvaamiseksi optisessa kuidussa. Mallia käyttäen pulssit kuljetetaan lasersysteemin läpi komponentti ja kuitu kerraallaan tavoitteena maksimoida piikkiteho kompressoinnin jälkeen. Mallin suora vertailu kokeellisiin mittauksiin ei ole vielä ollut mahdollista, mutta malli antaa fysikaalisesti järkeviä tuloksia niiltä osin kun ne ovat verrattavissa aiemmin testattuihin vastaavanlaisiin kuituvahvistimiin.

Kuvatun venytettyjen pulssien vahvistusjärjestelmän suurimmaksi rajoitteeksi paljastui simulaatioiden myötä itseisvaihemodulaatio paksunevassa valokuidussa erityisesti yhdistettynä epäsäännölliseen pulssin muotoon, joka saadaan venyttämällä kokeellisen laserlähteen pulsseja. Seurauksena olevaa monimutkaista epälineaarista vaihetta ei ole mahdollista kompensoida hilakompressorissa, mikä näkyy voimakkaina sivupulsseina. Käyttämällä Gaussista lähtöpulssia 5.4 nm spektrinleveydellä numeerinen malli ennustaa lasersysteemin pystyvän tuottamaan 52 µJ, 480 fs pulsseja B-integraalin arvolla 12.4 rad.

Avainsanat: venytettyjen pulssien vahvistus, kuitulaser, ultralyhyet pulssit, paksuneva kaksivaippainen valokuitu

PREFACE

I would like to thank my colleagues at Tampere University and Ampliconyx Oy for the opportunity to write this thesis on such a fascinating topic as ultrafast fiber lasers. Special thanks go to my thesis supervisor Dr. Regina Gumenyuk for always being there for my questions and concerns. On Ampliconyx side, I am grateful to Dr. Valery Filippov and Dr. Maxim Odnoblyudov for their constant support, encouragement and interest in my work. My long-term colleague and friend Teppo Noronen taught me how to build tapered fiber amplifiers and so much more. Without him, this thesis would have looked very different. Additionally, I wish to thank Andrei Fedotov, Dr. Vasily Ustimchik and Xinyang Liu for companionship in the sometimes-tedious lab work and Dr. Mikko Närhi for stimulating discussions on fiber laser modelling.

Tampere, 19th April 2020

Joona Rissanen

CONTENTS

LIST OF FIGURES

LIST OF TABLES

LIST OF SYMBOLS AND ABBREVIATIONS

Γ	overlap integral
Λ	grating period
α	absorption
β	propagation constant
γ	nonlinear coefficient
λ	wavelength
$\Delta\nu$	frequency bandwidth
ν	frequency
ω	angular frequency
$\varphi(\omega)$	spectral phase
$\phi(t)$	temporal phase
$\sigma_{a,e}$	absorption/emission cross section
τ	upper state lifetime
θ_D	diffraction angle
θ_I	incidence angle
θ_L	Littrow angle
ζ	saturation parameter
A	core area
$A(z,t)$	complex amplitude
A_{eff}	nonlinear effective area
a	fiber core radius
ANDi	All-Normal-Dispersion
AOM	Acousto-Optic Modulator
ASE	Amplified Spontaneous Emission
B	B-integral
c	speed of light
CCC	Chirally-Coupled-Core (Fiber)
CFBG	Chirped Fiber Bragg Grating
CPA	Chirped Pulse Amplification

CVBG	Chirped Volume Bragg Grating
CW	Continous Wave
D	dispersion parameter
$E(\mathbf{r}, t)$	electric field
EOM	Electro-Optic Modulator
$F(x, y)$	transverse electric field distribution of a fiber mode
f	focal length
f_R	Raman contribution to nonlinearity
FBG	Fiber Bragg Grating
FFT	Fast Fourier Transform
FWHM	Full-Width-at-Half-Maximum
g	gain
GNLSE	Generalized Nonlinear Schrödinger Equation
$H(\mathbf{r}, t)$	magnetic field
h	Planck constant
$h_R(\tau)$	Raman response function
$i(r)$	normalized transverse irradiance distribution of a radially symmetric fiber mode
IR	Infrared
J_n	nth order Bessel function of the first kind
K_n	nth order modified Bessel function of the second kind
k	wavenumber
L	length
l	fiber background loss
LMA	Large-Mode-Area (Fiber)
m	diffraction order
$N_{1,2}$	ion population in the lower (1) and upper (2) energy levels
N_t	doping concentration in fiber
n_2	nonlinear refractive index
n	refractive index
NA	Numerical Aperture
NALM	Nonlinear Amplifying Loop Mirror
NLSE	Nonlinear Schrödinger Equation
NOLM	Nonlinear Optical Loop Mirror

NPR	Nonlinear Polarization Rotation
P	power
PCF	Photonic Crystal Fiber
PM	Polarization Maintaining
r	radial coordinate
$S(\omega)$	spectral power
SBS	Stimulated Brillouin Scattering
SESAM	Semiconductor Saturable Absorber Mirror
SLM	Spatial Light Modulator
SPM	Self Phase Modulation
SRS	Stimulated Raman Scattering
t, T	time coordinate
TDCF	Tapered Double-Clad Fiber
TOD	Third Order Dispersion
UV	Ultraviolet
I	irradiance
V	V-parameter or normalized frequency
v_g	group velocity
v	speed
VBG	Volume Bragg Grating
WDM	Wavelength Division Multiplexer
XPM	Cross Phase Modulation

1 INTRODUCTION

Consisting of a vast number of identical photons, a laser beam represents concentrated energy in one of its purest forms. In space, this electromagnetic energy can be focused into a tiny spot roughly the size of a wavelength while, in time, the width of an ultrashort laser pulse can approach a single optical cycle. The resulting enormous local electric field readily interacts with matter to break and reorganize even the strongest chemical bonds [1], to drive numerous nonlinear transformations [2] and to probe events of extremely short duration [3].

The field of ultrafast lasers, informally understood as lasers generating pulses of roughly 1 ps or shorter, that devises these incredible tools is flourishing with constant advances reported in the achievable peak power and pulse width. Early ultrafast lasers were severely limited because nonlinear effects, most importantly self-focusing, destabilized the high-peak-power laser beam propagating in the amplifying medium. The solution to this problem was presented in 1985 by Donna Strickland and Gerard Mourou [4] in the form of the chirped pulse amplification (CPA) technique, for which they we were awarded the Nobel Prize for Physics in 2018. The technique essentially involves stretching a weak seed pulse dispersively, then passing the now lengthened pulse through the gain medium where its peak power remains relatively low, and finally compressing the pulse to its original duration by taking advantage of the relative coherence of its wavelength components. Though a collection of additional techniques for scaling pulse energy have been introduced [5, 6], CPA remains the standard workhorse of high-power ultrafast lasers.

Ultrafast lasers are also rapidly becoming more commonplace and practically useful devices outside the academic laboratories, especially in materials processing. Ultrafast laser processing has two main benefits compared to using CW or nanosecond-pulsed lasers. First, ultrashort pulses allow for more precise and energy-efficient sculpting of the material to generate micro- and even nano-scale structures with minimal heat-affected zone [1, 7]. The physics behind the superiority of high-peak-power pulses lies in the different interaction timescales of photons, electrons and phonons in the target material. When a laser pulse strikes the work piece, its energy is first absorbed by electrons at the very short femtosecond timescale of photon-electron interaction. However, it takes typically at least 10 ps for the electrons to transfer their energy to the lattice via electron-phonon collisions [7]. If the pulse duration is below this timescale of electron-phonon interaction, sublimation of the material starts only after the whole pulse has been absorbed. This eliminates losses incurred with longer pulses or CW radiation due to scat-

tering or absorption of laser light in the plasma or vapor generated over the work piece. The plasma then has time to disperse before the next pulse hits the material. Energy is not lost to thermal diffusion either because the high peak power results in the target spot sublimating before thermal diffusion into the surrounding material can take place. Furthermore, the sublimated atoms carry the deposited energy away with them because the phonon-phonon interactions are even slower than the electron-phonon interactions. This minimizes the amount of melted material and the size of the heat-affected zone around the processed area, enabling high-quality microstructuring even in metals with high thermal conductivity. As a result, the affected minimal depth of material is determined only by the optical, not thermal, penetration depth in the material, which is typically only tens of nanometers for metals.

The second major benefit of ultrashort pulses involves processing of optically transparent materials, such as glass and certain polymers. These materials do not normally absorb light, but the high intensities near the waist of a focused beam of ultrashort pulses result in strong nonlinear multi-photon absorption. If this absorption results in a phase change, three-dimensional structures can be written in transparent materials by changing the waist position with suitable beam delivery optics. The generated structures can be smaller than the diffraction limit of light because the nonlinear absorption occurs only in the narrow focal volume at the center of the beam where the optical intensity is at its highest. Two-photon polymerization [1] is a representative application example that demonstrates ultrafast laser processing of transparent materials.

To be successful in these kinds of practical applications, an ultrafast laser must not only provide high-quality short energetic pulses but also be robust, reliable and cost-effective. This calls for ultrafast fiber lasers, whose continuous wave (CW) counterparts already dominate the industrial laser market in more traditional use cases. Compared to the already established ultrafast bulk solid-state lasers, fiber lasers promise alignment-free operation, easy thermal management [8] and the use of mass-producible components. Performance-wise, fiber lasers excel at high-average-power operation, resulting in fast processing time. However, fiber lasers have struggled with generating high-energy pulses since the light has to propagate a long distance confined in the narrow core in the solid-state glass medium, with nonlinear effects such as self-phase modulation (SPM) and stimulated Raman scattering (SRS) severely limiting the achievable peak power [9].

Because of the numerous other advantages of using fiber lasers, several techniques have been developed to increase the size of the propagating mode to reduce peak irradiance inside the fiber, while also avoiding beam quality degradation associated with multiple transverse mode operation. These techniques include standard large-mode-area (LMA) fibers available at up to 30 µm core diameters, where single-mode beam quality is reached by suppressing the higher order modes with bend losses [10] or by carefully exciting only the fundamental mode [11]. Chirally-coupled-core (CCC) fiber [12] is a different approach that includes one or more helical side cores around the main core to couple out the higher order modes and allows reaching single-mode operation in core sizes of over

50 µm [13]. Being entirely solid state, chirally-coupled core fibers are splicing compatible with standard fibers. Another effective technology is photonic crystal fiber (PCF) [14], the large-pitch variant of which can reach single-mode beams from even $>$100 µm core [15], but the fiber then becomes a rigid rod. Because the PCF structure contains air holes that would collapse during splicing, signal light must be coupled into the fiber in free-space, which is sensitive to alignment, leading to a loss of many of the benefits associated with normal fiber lasers.

The above-mentioned specialty fiber technologies have been used to demonstrate numerous chirped-pulse amplification systems in the scientific literature. Želudevičius et al. [16] obtained 400 fs, 50 µJ pulses at 100 kHz repetition rate at 1065 nm using a chirally-coupled-core power amplifier with 33 µm core diameter. Wan et al. [17] have demonstrated both a 705 fs, 0.85 mJ, 1030 nm laser operating at 100 kHz using rod-type photonic crystal fiber with 100 µm core diameter and a high-average-power 1.05 kW 69 MHz laser whose output was compressible to 800 fs pulse duration using commercial standard LMA fiber with 30 µm core diameter as the final amplifier. While the authors of [17] diverted only a fraction of the output beam for compression, Eidam et al. [18] have reported a complete CPA system generating 830 W at 78 MHz after compression. The compressed pulse duration was 640 fs. The same group has also demonstrated a high-pulse-energy CPA system [19] generating 2.2 mJ, 480 fs pulses at 5 kHz repetition rate, which translates to a 3.8 GW peak power. Both of their laser systems were based on PCF power amplifiers.

Missing from the CPA system demonstrations is yet another specialty fiber technology, tapered double-clad fibers (TDCF), which have been developed at Tampere University [20] and are currently being commercialized by Ampliconyx Oy. Tapered double-clad fibers resemble normal LMA fibers in that they are manufactured from similar preforms. However, the diameter of a tapered fiber changes along its length, which gives it several advantages over standard LMA fibers. The thin input end can be single-mode and thus normally spliceable to a signal fiber without exciting higher-order modes. A tapered fiber's diameter grows slowly towards the output end where the core size can exceed that of standard LMA or CCC fibers without compromising beam quality. Multimode pump light can be conveniently coupled in from the thick end, so most of the amplification takes place where the core size is large.

The target of this thesis was to design an ultrafast CPA fiber laser system based on a tapered double-clad fiber amplifier for materials processing applications that could in the future be refined into a commercial product. The work presented here consists of an experimental part and a theoretical part based on numerical modelling. More specifically, a mode-locked low-power fiber laser generating seed pulses for subsequent amplification was realized experimentally, while the rest of the CPA system design was explored by way of extensive numerical simulations, the results of which can be later used to guide the building of the whole high-power ultrafast laser system in practice. The developed simulation tools will also be of value in the future since they can be applied to other

setups besides the one described here.

This thesis is structured into five chapters including this Introduction. Chapter 2 covers the theoretical background relevant to ultrafast fiber lasers and amplifiers and the chirped pulse amplification technique. Chapter 3 presents the high-level design of the CPA system studied in this thesis and the choices and compromises involved in arriving at the design. The main results are then reported in Chapter 4, including experimental data for the seed laser and simulation results for the rest of the laser system. Finally, Chapter 5 concludes the thesis with the main outcomes and possible future work related to this research.

2 THEORY

Understanding a fiber-based chirped pulse amplification laser system requires extensive theoretical background knowledge in optical fibers, fiber amplifiers, ultrashort pulses and dispersive elements used to stretch and compress those pulses. This section aims to provide that understanding in a concise way.

2.1 Optical fiber types in a fiber laser system

An optical fiber is a dielectric waveguide in the form of a long, thin strand of glass, typically fused silica (amorphous SiO_2). The most basic optical fiber has a small core surrounded by a larger cladding, which has a lower refractive index than the core. The refractive index difference can confine suitably launched light to propagate along the length of the fiber inside the core. Intuitively, the wave guidance can be thought of as the result of total internal reflection at the core-cladding boundary. The core diameters of most optical fibers are of the same order of magnitude as the wavelength of the propagating light, which means that the ray optics approach breaks down and diffraction must be taken into account. While diffraction tries to expand the propagating beam of light, refraction at the core-cladding boundary tries to keep the light in the core. For certain transverse distributions of electric field amplitude, diffraction and refraction balance each other out exactly allowing such distributions to propagate in the fiber unchanged. These distributions are known as the fiber modes, and the number of allowed modes and their shapes depend on the structure of the fiber. Therefore, structural differences in the sizes and refractive indexes of the core and the cladding(s) allow classifying optical fibers into single-mode, large-mode-area, multi-mode and double-clad fibers.

Single-mode fibers support only one mode, the fundamental mode. A single-mode fiber must fulfill the single-mode condition $V \leq 2.405$ where the normalized frequency V (also known as V-parameter) is defined as

$$V = \frac{2\pi}{\lambda} a \sqrt{n_{core}^2 - n_{clad}^2} = \frac{2\pi}{\lambda} a \mathrm{NA} \tag{2.1}$$

where λ is the wavelength of the propagating light, a is the core radius and the numerical aperture $\mathrm{NA} = \sqrt{n_{core}^2 - n_{clad}^2}$ is defined by the refractive indexes of the core and the cladding. To fulfill the single-mode condition, a fiber must have a small core and/or

a low numerical aperture. Equation (2.1) also tells that increasing the wavelength decreases the V-parameter. Thus, each fiber has a so-called cut-off wavelength, which is the shortest wavelength, at which the fiber is still single-mode. The cut-off wavelength of a single-mode fiber must naturally be shorter than the intended wavelength of operation.

Single-mode fibers have several advantages that make them the most widely used subclass of optical fibers by a wide margin. First and foremost, the fundamental mode has close to diffraction-limited beam quality making the output beam focusable into a tight spot, which is a highly desirable property in laser systems. Additionally, the output beam shape is independent of how light was launched into the fiber and does not deteriorate if the fiber is bent, though poor launching conditions or excessive bending will cause a loss of optical power. In pulsed applications, single-mode fibers avoid the problem of modal dispersion where the pulse duration would increase due to different modes propagating at different velocities.

On the other hand, single-mode fibers have several disadvantages. For example, they cannot be used to guide radiation from low-brightness non-diffraction-limited sources effectively. In fiber lasers, the tight confinement of the fundamental mode in the small core can give rise to excessive optical nonlinearity, restricting the use of single-mode fibers to low-power fiber lasers and amplifiers. Overcoming these limitations necessitates the use of fibers with larger cores, which violate the single-mode condition.

Multi-mode fibers are the opposite of single-mode fibers in that they typically support hundreds of transverse modes. For this purpose, a multi-mode fiber must have a large core, typically $\geq 50\,\mu m$ in diameter and a high numerical aperture of ≥ 0.15. It is easy to launch light into a multi-mode fiber but the beam quality of a launched diffraction-limited beam would suffer greatly since numerous modes would be excited at the fiber's input and mode-coupling during propagation would change the mode content even further. Therefore, the output beam quality of a typical multi-mode fiber is necessarily bad. However, multi-mode fibers are essential in fiber laser systems for pump power delivery from high-power multi-mode laser diodes.

The middle ground between single-mode fibers and multi-mode fibers is occupied by the so called large-mode-area fibers. They are designed for an increased cross-sectional fundamental mode area, while aiming for close to single-mode beam quality at the same time. Compared to strictly single-mode fibers, LMA fibers have larger cores typically up to $30\,\mu m$ in diameter and lower numerical apertures. Though the decrease in numerical aperture partly offsets the increase in core size, LMA fibers have V-numbers in excess of 2.405 and thus support a few higher order modes in addition to the fundamental mode. Still, LMA fibers are capable of single-mode operation with proper handling. In particular, this means launch conditions that excite only the fundamental mode. Additionally, the fiber should be coiled with a suitable bend radius, which results in losses to the more weakly guided higher-order modes while leaving the fundamental mode almost unaffected. The lower the numerical aperture is, the more sensitive the fiber modes are to bend losses and the easier it is to obtain good beam quality. However, bend losses can

make the fundamental mode lossy as well, which sets a lower acceptable limit to bend radius. The fabrication of LMA fibers also requires careful control of refractive indexes in the core and cladding because the fundamental mode is very sensitive to random refractive index fluctuations caused by imperfections when the numerical aperture is low. Therefore, such fibers are considerably more expensive than more traditional single-mode or multi-mode fibers.

Active fibers contain laser-active ions in their core and can amplify optical signals when the ions are excited to a suitable metastable energy level with an optical pump beam. Their basic geometry can be that of a single-mode, multi-mode or LMA fiber but the choice between single-mode and multi-mode pump sources separates them additionally into single-clad (= core-pumped) and double-clad (= cladding-pumped) fibers. In a single-clad active fiber, the pump beam propagates in the core together with the amplified signal and must therefore also be diffraction-limited if the core is single-mode. In contrast, a double-clad fiber contains a second inner cladding around the core, which acts as a waveguide for the pump radiation. The outer cladding that confines the pump beam is typically made of either low-index polymer or fluorine-doped glass resulting in a pump NA of at most 0.48. The maximum diffraction-limited output power from a semiconductor laser diode is approximately 1 W, which limits the operation of core-pumped fiber lasers and amplifiers to low average powers. High-power operation requires double-clad active fibers, which can be pumped by powerful multi-mode pump diodes. Double-clad fiber amplifiers are said to work as brightness converters since they transform the low-brightness pump light into diffraction-limited signal beam.

The fiber geometry also affects its polarization properties. In an ideal single-mode fiber, the core supports two polarization modes which, in theory, propagate independently at the same phase velocity in the absence of any birefringence. However, a real fiber exhibits weak residual birefringence resulting from stresses in the glass material. Additionally, the birefringence can vary unpredictably due to external factors, such as bending and temperature changes. This leads to coupling of the two polarization modes, essentially randomizing the output polarization [21].

However, many laser systems benefit from stable, linear output polarization. From the end user's perspective, linear polarization is required for coherent interactions such as nonlinear frequency-doubling. In materials processing, stable linear p-polarization allows maximal energy transfer to the work piece when the beam is incident at close to Brewster's angle, while unstable polarization would lead to large fluctuations in absorbed power. From a laser manufacturer's perspective, problems caused by unpredictable polarization state are equally easy to identify. For example, mode-locked fiber lasers are very sensitive to polarization changes caused by environmental disturbances leading to fluctuations of both the pulse duration and the spectrum. Additionally, many optical components have considerable polarization-dependent losses or phase retardation. For instance, acousto-optic modulators contain a birefringent crystal, which can act as a high order waveplate, while diffraction gratings typically exhibit large losses when the polar-

ization vector is not aligned with the grating grooves and both components are therefore best used with correctly oriented linear polarization.

All these challenges can be overcome by making the whole laser system to operate in a single well-defined polarization state. In a fiber laser, this requires the exclusive use of special polarization maintaining (PM) fibers, which can preserve an input linear polarization of the fundamental mode by breaking the fiber's circular symmetry for example by adding so called stress rods on both sides of the core. The stress rods are made of glass with a different thermal expansion coefficient from the rest of the material, which creates "frozen-in" stress in the fiber during its fabrication. The stress makes the fiber's core slightly birefringent by the photo-elastic effect. The birefringence mostly prevents coupling between the two polarization modes so the input polarization is preserved if light is launched into the fiber with polarization matching one of those modes (in the plane of the rods or perpendicular to it). For an arbitrary input polarization state, a PM fiber acts as a long waveplate and the output polarization will be unpredictable. For this reason, joining two PM fibers together requires careful alignment of the stress rods by rotating the fibers.

2.2 Fundamental fiber mode

The balance of diffraction and refraction gives rise to a finite number of modes or fixed electric field amplitude distributions that can propagate in the core of an optical fiber. Many fiber lasers and amplifiers are based on single-transverse-mode operation, in which the fiber only supports the lowest order fundamental LP_{01} mode or if higher-order modes are allowed, they are suppressed by selective excitation at the fiber's input, by bending or by some other means. Ultrafast lasers aim to generate as high peak intensities as possible, which requires concentrating the laser pulse's energy both in time and in space. As the fundamental fiber mode closely matches a free space Gaussian beam and thus possesses the best achievable focusability, ultrafast fiber lasers almost always aim for single-transverse mode operation. Therefore, understanding only the fundamental fiber mode is often a sufficient starting point for the mathematical description of ultrafast fiber lasers. This section covers the basic properties of the LP_{01} mode based on the theory of weakly-guiding step-index fibers.

The radially symmetric fundamental mode is characterized by its normalized transverse intensity distribution $i(r)$ and its propagation constant β. In principle, these are found starting from Maxwell's equations and solving the resulting Helmholtz equation in cylindrical coordinates with the boundary conditions imposed by the fiber's waveguide structure. Since this derivation is well documented elsewhere [22, 23], it makes sense to only present and discuss the end result for the fundamental mode here.

The shape of the fundamental mode resembles and is commonly approximated as a Gaussian. However, the actual functional form is based on Bessel functions and given in eq. (2.2).

$$i(r) = \begin{cases} \frac{1}{\pi}\left[\frac{v}{aV}\frac{J_0(ur/a)}{J_1(u)}\right]^2, & r < a \\ \frac{1}{\pi}\left[\frac{u}{aV}\frac{K_0(vr/a)}{K_1(v)}\right]^2, & r \geq a \end{cases} \tag{2.2}$$

where a is the core radius of the fiber, $J_{0,1}$ are Bessel functions of the first kind, $K_{0,1}$ are modified Bessel functions of the second kind, V is the normalized frequency or V-parameter introduced in eq. 2.1. v and u are dimensionless convenience parameters defined as

$$\begin{aligned} v &= a\sqrt{\beta^2 - k_{clad}^2} \\ u &= a\sqrt{k_{core}^2 - \beta^2} \end{aligned} \tag{2.3}$$

which satisfy the relation

$$v^2 + u^2 = V^2 \tag{2.4}$$

in which $k_{core} = \frac{2\pi}{\lambda} n_{core}$ and $k_{clad} = \frac{2\pi}{\lambda} n_{clad}$ are the wavenumbers in the core and the cladding, respectively, at the wavelength of interest λ. Equation (2.2) can be used to calculate the mode shape in a specific fiber at a specific wavelength by requiring that $i(r)$ be continuous at the core-cladding boundary $r = a$. One way to do that is to take the propagation constant β as a variable and solve for a β_0 between k_{core} and k_{clad} that fulfills the continuity criterion. When there are multiple solutions (corresponding to higher order radially symmetric LP_{0x} modes), the largest propagation constant is the correct solution for the fundamental mode, which resides mostly in the core and thus has the highest effective refractive index. Alternatively, either u or v could be directly taken as the variable (with the other one calculated from eq. (2.4)) and then solved similarly. This way, the mode shape can be found without knowing the exact refractive indexes of the core and the cladding; only the numerical aperture $\mathrm{NA} = \sqrt{n_{core}^2 - n_{clad}^2}$ is needed. Thus the mode shape, unlike the propagation constant, does not depend on the absolute refractive indexes.

Three parameters determine the mode shape: the core radius and the numerical aperture of the fiber and the wavelength of the propagating light. The operation wavelength of a fiber laser or amplifier is typically fixed by the intended application, leaving the fiber's core size and NA as free design parameters. The choice of these parameters is further limited by the requirement to keep the fiber single-mode. For that purpose, the numerical aperture and core radius must be small enough to fulfill the single-mode condition $V \leq 2.405$. Any increase in core size must therefore be coupled with a proportional decrease in

NA to maintain near-diffraction-limited beam quality. In LMA fibers, which are not strictly single-mode, minimizing the number of supported modes is still important for good output beam quality.

Like the intensity distribution, the propagation constant β is also wavelength-dependent, both through eqs. (2.1)–(2.3) and through the wavelength-dependence of the refractive indexes, meaning that different wavelengths propagate at different phase velocities. This gives rise to dispersion, which is of utmost importance in the propagation of ultrashort pulses in optical fibers and will be discussed in greater detail in section 2.6.2.

The fundamental mode shape affects the operation of fiber amplifiers in two ways. First, the overlap between the mode and the core determines how strongly the mode interacts with the laser active ions in the core. The overlap Γ of the fundamental mode with a core of radius a can be integrated as

$$\Gamma = 2\pi \int_0^a i(r) r dr \tag{2.5}$$

Possible values of Γ range from 0 (mode completely outside the core) to 1 (mode completely inside the core). Increasing either the numerical aperture or the core radius confines the mode more tightly in the core, resulting in a larger overlap. In some special fibers, the laser active ions can be located outside the core, in which case the overlap must be explicitly calculated between the mode and the actual ion distribution, but the importance of the mode shape is equally true. The discussion of gain and absorption in active fibers in section 2.4 will make extensive use of the overlap Γ.

The second reason why understanding the mode shape is crucial is because it affects the peak irradiance and the onset of nonlinear effects at high powers. The more spread-out the mode is, the higher power can propagate in the fiber without significant nonlinearity. The "spread-outness" is quantified as the effective mode area A_{eff}. For an arbitrary mode with a transverse electric field distribution $F(x, y)$ it is defined as

$$A_{\text{eff}} = \frac{\left[\iint_{-\infty}^{\infty} |F(x,y)|^2 dxdy\right]^2}{\iint_{-\infty}^{\infty} |F(x,y)|^4 dxdy} \tag{2.6}$$

This equation can be simplified for any radially symmetric mode, such as the fundamental mode, to

$$A_{\text{eff}} = 2\pi \frac{\left[\int_0^\infty i(r) r dr\right]^2}{\int_0^\infty i(r)^2 r dr} \tag{2.7}$$

where $i(r)$ is the transverse modal intensity distribution introduced earlier. Increasing the core size and decreasing the numerical aperture enlarges the effective area, weakening nonlinear effects.

The fiber mode is a very useful abstraction since it allows treating the propagation of light in optical fibers as a purely one-dimensional problem. The following sections take full advantage of this fact.

2.3 Active fiber as gain medium

Light amplification in optical fibers is based on laser-active trivalent rare-earth ions in the core where they can interact with the propagating light. Such a fiber, referred to as either a rare-earth-doped optical fiber or simply active fiber, can store energy in the form of electronic excitation. Energy can be deposited by promoting the ions to a metastable energy level with an optical pump beam at a wavelength that the ions can absorb. This energy can then be released to amplify a signal beam at a longer wavelength. This section discusses the properties of optical fibers as gain media and is roughly divided into two parts. The first part examines the unique advantages of the fiber geometry compared to other gain media, which have led to a great proliferation of fiber lasers in practical applications. The second part covers the spectroscopy of the laser active ions used in light-amplifying optical fibers.

In a sense, an active fiber is an optically pumped solid-state laser medium like any crystalline laser rod or disk. However, the long and thin geometry and the built-in waveguide structure set active fibers apart from their more traditional counterparts in multiple ways [24]. First, the strong interaction between the light and the rare-earth ions, caused by high optical irradiance in the small core, facilitates a high optical-to-optical conversion efficiency from pump to signal power with reduced waste heat generation. Thanks to the fibers' favorable surface-to-volume ratio, the generated heat is also easily dissipated. Consequently, fiber lasers and amplifiers do not suffer from thermal lensing, which is a major obstacle in traditional solid-state lasers, until at very high average powers. The absence of thermal lensing decouples the output beam shape from the average power level enabling the generation of high-power near-diffraction-limited beams. For the same reason, the cavity of a high-power fiber laser, unlike that of a bulk solid-state laser, does not require meticulous optimization for a specific output power level. The long propagation length in an active fiber is also beneficial by making large single-pass gains of tens of dB possible. This further favors the use of active fibers as traveling-wave optical amplifiers.

The waveguide nature of active fibers brings them several practical advantages not directly related to the physics of the gain medium but still definitely worth mentioning. First, most active fibers can be conveniently end-pumped with cost-efficient laser diodes. Second, there is a large selection of standard-sized fibers and fiber-coupled components available commercially owing to the growth of both the fiber laser and the optical telecommunication markets. As fibers can be joined together with low losses using fusion splicing, the above-mentioned advantages have enabled the building of compact, monolithic and totally alignment-free fiber laser devices.

Having discussed the geometrical aspects of active fibers, we now turn our attention to the rare-earth laser-active ions and their spectroscopic properties. In the periodic table of elements, the rare-earth elements used in active fibers are found among the lanthanide series. As trivalent ions, these elements have partly filled 4f shells, whose wave functions are localized closer to the core than the filled 5s and 5p shells and thus partly shielded from outside influence [25]. For this reason, optical transitions with multiple relatively narrow absorption and emission bands at wavelengths from UV to IR can occur between the 4f electronic states. Because the 4f-4f transitions are also electric dipole forbidden [26], the metastable states in rare-earth ions have long lifetimes from hundreds of microseconds up to the 10 ms lifetime in Er^{3+}, which makes rare-earth-doped glasses excellent energy storage media.

The exact absorption and emission spectra of rare-earth ions are determined by the splitting of the 4f states through interaction with the ion's other electrons and to a lesser extent with the host material ions (=crystal field). The dominant effect of atomic interactions dictates the transition wavelengths of a certain rare-earth element, which are therefore relatively independent of the host material. The weaker interaction with the crystal field, referred to as Stark splitting, then affects the finer features such as relative strengths and widths of the absorption and emission peaks. The resulting continuous energy bands are called Stark level manifolds.

The three most commonly used rare-earth elements in fiber laser technology are erbium, thulium and ytterbium, all of which have prominent transitions in the near-infrared region. Yb^{3+} ions emit light at around 980-1100 nm, Er^{3+} ions at around 1525-1610 nm and Tm^{3+} ions at around 1800-2100 nm. Erbium-doped fibers are used in telecommunications because the emission band coincides with the loss minimum of optical fibers at 1.55 µm. Thulium-doped fibers are used especially in eye-safe laser applications because the laser radiation at 2 µm is absorbed by water and cannot reach the retina. Ytterbium-doped fiber lasers and amplifiers hold the current high-power performance records owing to the many advantages of the Yb:silica gain medium. For this reason, the laser system designed in this thesis uses ytterbium-doped fibers as well. The advantages and the spectroscopy of Yb^{3+}:silica are covered next in more detail.

The first major advantage of ytterbium over the alternative laser-active ions is its simple energy band structure comprising only two Stark level manifolds. The lack of higher-lying energy levels prevents excited state absorption, which can be a significant loss

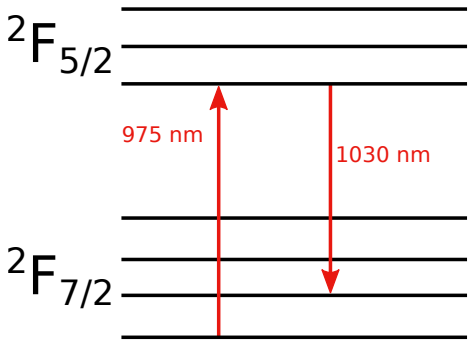

Figure 2.1. *The Yb^{3+} energy level structure after [27] with some transitions indicated.*

mechanism in other types of active fibers. The energy level structure of Yb^{3+}:silica is shown in fig. 2.1. The lower manifold ${}^2F_{7/2}$ contains four sublevels and the upper manifold ${}^2F_{5/2}$ three sublevels. However, the energies of these sublevels are broadened due to Stark splitting, giving raise to continuous absorption and emission spectra because the ions are embedded in the host glass material. As a result, there are multiple transitions that can lead to the absorption or emission of a photon at a specific wavelength.

Keeping track of all these transitions individually is unfeasible, which necessitates the use of the so-called effective transition cross sections in the mathematical description of active fibers. Effective transition cross sections are a theoretical abstraction that incorporates and averages over all the sublevels, their degeneracies and thermal populations that contribute to the laser transition at a certain wavelength to express the transition probability as a single number. Effective transition cross sections are a property of the rare-earth ion and the host material at a certain temperature. They are experimental data usually reported in academic papers or given by active fiber manufacturers. The importance of the thermal populations of ions requires the usually valid assumption that rapid non-radiative thermalization within the sublevels keeps them in thermal equilibrium despite the optical transitions between the manifolds. Unsurprisingly, the most probable transitions with the largest effective cross sections are the ones originating from the lowest sublevels, which have the largest thermal populations.

The use of effective transition cross sections and the simple energy band structure allow modelling the Yb^{3+} ion excitation as a two-level system where the effective absorption cross sections describe the transition probabilities from the lower to the upper level and the effective emission cross sections describe the reverse stimulated emission process. Figure 2.2 shows the effective absorption and emission cross sections for Yb^{3+}:silica at room temperature. Based on the spectra, possible pump wavelengths where the fiber can absorb range roughly from 840 nm to 1060 nm and possible emission wavelengths from 900 nm to 1200 nm. The choice of both pump and signal wavelengths will be reviewed shortly.

First however, it is instructive to discuss the nature of the Yb:silica gain medium in respect to the common classification of three- and four-level systems. In a three-level system, the lower laser level is the ground state and population inversion is reached only when over

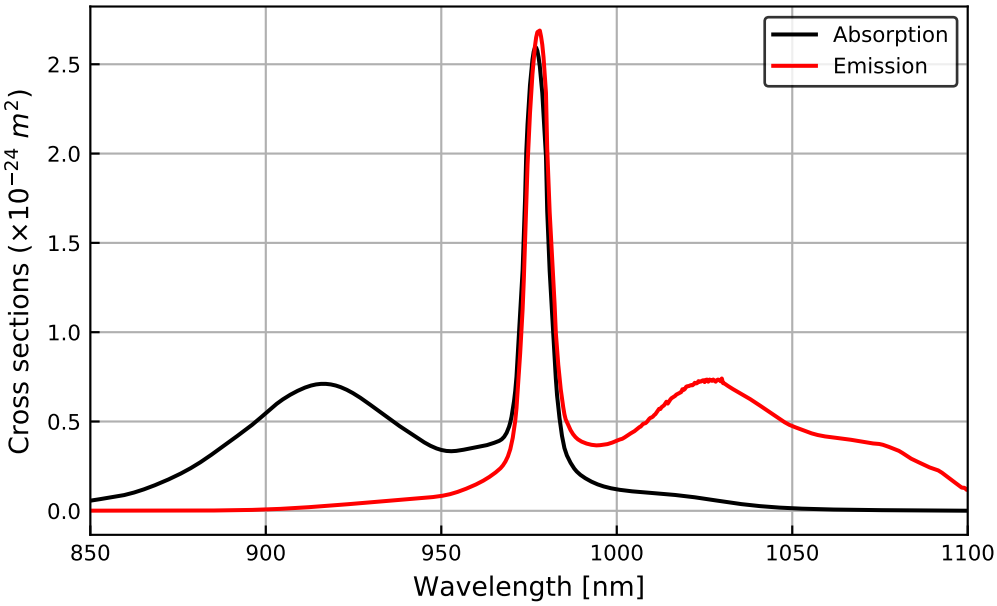

Figure 2.2. *Smoothed fit to Yb^{3+}:silica absorption and emission cross sections obtained from Nufern [28].*

50 % of the ions are pumped to the upper laser level. In a four-level system, in contrast, the thermal population in the lower laser level is practically zero, so even minimal pumping leads to population inversion. Yb:silica is classified as a quasi-three-level gain medium, showing characteristics of both three- and four-level systems depending on the absorption and emission wavelengths. For laser operation at 976 nm, the effective absorption and emission cross sections are equal and Yb:silica behaves essentially as a three-level system. For laser operation at $>$1060 nm, signal absorption is almost zero, making Yb:silica effectively a four-level system. At the intermediate wavelengths, there is some thermal population at the lower laser level, leading to weak absorption and operation in between three- and four-level systems.

Another essential concept for understanding the choice of pump and signal wavelengths is the quantum defect, which is the difference between the energies of the pump and signal photons. Quantum defect sets the theoretical limit for power conversion efficiency from pump to signal in the ideal case where each pump photon is transformed into a signal photon. In other words, quantum defect is a measure of how much waste heat is necessarily generated when using a specific pair of pump and signal wavelengths. Therefore, the minimization of the quantum defect should be one factor considered when choosing the operation wavelengths. Fortunately, Yb:silica is a highly efficient gain medium based on its low quantum defect. For example, when pumped at 980 nm with a signal wavelength of 1030 nm, the quantum defect is only about 5 % of the pump photon energy.

In addition to quantum defect, the inherent broadband noise in fiber amplifiers, caused by amplified spontaneous emission (ASE), also plays a role in how far apart the pump and signal wavelengths can realistically be. The origin of ASE is easy to grasp. Any ions excited to the upper Stark level manifold can undergo spontaneous emission by

emitting a photon with a random phase in a random direction. Some of the spontaneously emitted photons are captured by the fiber core and start to propagate towards either end of the fiber. These photons can then induce stimulated emission in other excited ions, depleting excitation in the fiber while the noise gets amplified, hence the name amplified spontaneous emission. ASE effectively limits the maximum gain of even well-designed fiber amplifiers to about 30-50 dB because, after a certain point, increasing the pump power will only increase the ASE output power without raising the inversion in the fiber. The ASE spectrum follows the emission spectrum of the fiber with the natural restriction that ASE is only generated at longer wavelengths than the pump beam. Therefore, to suppress excessive ASE, the pump wavelength should be chosen close to the signal wavelength.

Now armed with the useful concepts of three- and four-level systems, quantum defect and ASE, it is possible to discuss the choice of pump and signal wavelengths in Yb-doped fiber lasers and amplifiers while also taking into account the spectral shapes of absorption and emission in fig. 2.2. In terms of pumping, there are two absorption maxima to be considered: a weaker but broader peak at around 915 nm and a stronger, sharper peak at 976 nm. Both two pump wavelengths have their own advantages and disadvantages. A clear benefit of 915 nm pumping is the negligible emission cross section at 915 nm, which means that the pump beam can potentially excite all the ions into the upper energy level. Moreover, the broadness of the 915 nm absorption peak makes the absorption insensitive to slight changes in pump wavelength allowing the use of cheaper pump diodes without wavelength stabilization. If the wavelength of the signal to be amplified lies within the 976 nm peak, 915 nm pumping must obviously be used. However, if the signal has a longer wavelength, such as 1030 nm or more, pumping at 976 nm might be preferable. This decreases the quantum defect and avoids strong ASE at 976 nm caused by 915 nm pumping. Even more importantly, the effective absorption cross section at 976 nm is 2.5 to 3 times larger than at 915 nm, which allows all the pump to be absorbed in a much shorter length of fiber. Unfortunately, stable operation with 976 nm pumping typically requires wavelength-stabilized laser diodes since a drift in pump wavelength of only a few nanometers in either direction would cause a major drop in absorption. Enhanced pump absorption is particularly important in double-clad active fibers, whose absorption is lowered due to the multimode pump beam's reduced overlap with the core.

As for signal wavelength, ultrafast Yb-doped fiber lasers and amplifiers are typically operated at 1030-1040 nm because of the broad gain bandwidth in that region, which can support pulses as short as 100 fs and because the effective emission cross sections at those wavelengths are also quite high so the fiber length can be kept short to avoid dispersion and nonlinearity. Such lasers, like the one designed in this thesis, can be conveniently and efficiently pumped at 976 nm. The pumping must be strong enough to overcome the still sizable absorption at 1030-1040 nm.

2.4 Rate equation model of a fiber amplifier

The basic operation of a fiber amplifier or laser can be mathematically described using a system of differential equations for the optical power propagation and the excitation of the laser active ions [29]. The differential equations for an active fiber are mostly similar to those of a traditional solid-state laser but they must take into account the waveguide geometry of the fiber, which has two consequences. First, only the part of the mode that resides inside the core can interact with the laser active ions. Second, since the fiber can be rather long, the excitation and, consequently, gain and absorption vary strongly along its length. Exactly these reasons also make it difficult to predict accurately how a fiber amplifier will operate even in steady state without solving the system of differential equations, which must be done numerically in most cases. Therefore, when designing a fiber amplifier, simulations based on such a differential equation model can be invaluable as they allow optimizing the type and length of active fiber used, the required pump and signal input powers as well as the noise properties of the amplifier. Ideally all the spectroscopic and geometric parameters of the fiber(s) should be known beforehand, which can be difficult since fiber manufacturers do not always provide such data. This section aims to provide the basic background, including both physical and computational considerations, for understanding such simulations.

Before presenting the equations, a few words must be said on the assumptions built into the differential equation model and the applicability of the model for pulsed signals. A very important aspect is that the rate equation model is based on power propagation only and thus excludes the phase of the optical field. The lack of phase information is typically irrelevant for cases with continuous wave inputs. Long pulses from milliseconds down to nanoseconds can also be handled in the model by variation of power only since such relatively slow modulation does not affect the spectrum of the signal appreciably. However, at a first glance, this limitation appears to preclude the simulation of ultrafast fiber amplifiers because phase is absolutely required to describe ultrashort pulses. Fortunately, the phase-related effects, dispersion and nonlinear phenomena, are usually kept at a minimum in a well-designed ultrafast optical amplifier. If that is the case, the ultrafast pulse train can be approximated by a CW signal of an equal average power without a significant loss of accuracy. Another requirement is that the repetition rate is much higher than the inverse of the upper state lifetime of the laser active ions, in Yb-doped fibers >10 kHz. This condition is practically always true for ultrafast pulse trains in fiber amplifiers because otherwise either the average power would be negligible or the peak power enormous and cause strong nonlinearity.

Apart from the lack of phase information, there is substantial freedom in what physical phenomena to include in or exclude from the differential equations. For example, the model of the laser active ions can in principle be arbitrarily complex with a multitude of different ion species, energy levels and radiative and non-radiative transitions. The model of the interaction between the ions and the propagating optical power must necessarily include at least the three basic processes: absorption, stimulated emission and spon-

taneous emission. Other phenomena such as Rayleigh scattering or Raman scattering can be added in simple forms if deemed important. It is also possible to create a full multiphysics model of an active fiber by incorporating thermal and strain effects which are coupled to the optical properties. In the following, the ion population is modelled with a two-level system with effective transition cross sections because of the simple energy level structure of Yb^{3+} ions and the scattering and multiphysics effects are omitted for simplicity.

An essential part of the model is that all light propagating in the fiber is divided into so called *optical channels* characterized by their wavelength (or frequency), bandwidth, input power and propagation direction (forward or backward). Any broadband signals with bandwidths can be broken into several channels if necessary, depending on how sharply gain and absorption vary around the channel's center wavelength. The power propagation of a single channel is then described by the following partial differential equation (a one-way wave equation):

$$\frac{\partial P(z,t)}{\partial z} + \frac{1}{v}\frac{\partial P(z,t)}{\partial t} = \Gamma\sigma_e N_2(z,t)P(z,t) - \Gamma\sigma_a N_1(z,t)P(z,t) - lP(z,t) + 2\Gamma\sigma_e N_2(z,t)h\nu\Delta\nu \quad (2.8)$$

where N_2 and N_1 are the ion populations in the upper and lower energy levels and all the constants and the optical power $P(z,t)$ are properties of the specific channel. v is the speed of light in the fiber, Γ is the overlap integral from eq. 2.5, σ_e and σ_a are the effective emission and absorption cross sections, l is the background loss, $h\nu$ is the photon energy and Δv is the frequency bandwidth. The light propagates in the direction of the z-axis.

In a steady state, the time derivative on the left-hand side vanishes, and eq. (2.8) is reduced to an ordinary differential equation. The first term on the right-hand side refers to increase in power via stimulated emission by the laser active ions. The second term is similarly loss to absorption by the laser active ions. The third term contains all other sources of propagation loss in the fiber. The final term describes spontaneous emission due to the laser active ions that is not proportional to the existing power. The factor two in the spontaneous emission term is due to the two polarization modes that are supported by a single-mode fiber. Spontaneous emission can usually be neglected for narrowband signals but is otherwise essential as the source of wideband ASE.

Equation (2.8) can be simplified by using three other parameters: the total doping concentration $N_t = N_1 + N_2$ and the Giles parameters for gain g^* and absorption α [29].

$$\begin{aligned} g^* &= \Gamma\sigma_e N_t \\ \alpha &= \Gamma\sigma_a N_t \end{aligned} \quad (2.9)$$

g^* and α represent the maximum possible values for gain and absorption since they assume that all the ions are on the starting energy level of the optical transition, which is the upper energy level for gain and the lower energy level for absorption. The overlap integral Γ is used here as a geometric correction coefficient which gives the fraction of optical power propagating in the core. A major benefit of g^* and α is that they are easier to measure experimentally than the cross sections. With the three constants, it is possible to eliminate the lower level population N_1, the cross sections and the overlap integral Γ from eq. (2.8), resulting in the following equation

$$\frac{\partial P(z,t)}{\partial z} + \frac{1}{v}\frac{\partial P(z,t)}{\partial t} = [\alpha + g^*]\,\frac{N_2(z,t)}{N_t}P(z,t) - [\alpha + l]P(z,t) + 2g^*\frac{N_2(z,t)}{N_t}h\nu\Delta\nu \tag{2.10}$$

The second type of equation required for the description of a fiber amplifier is the rate equation for the laser active ions:

$$\frac{dN_2(z,t)}{dt} = \sum_k \frac{P_k(z,t)}{hv_kA}\left(\alpha_k - (\alpha_k + g_k^*)\,\frac{N_2(z,t)}{N_t}\right) - N_2(z,t)/\tau \tag{2.11}$$

where A is the cross-sectional area of the fiber core, τ is the lifetime of the excited state and k refers to summation over all the optical channels propagating in the fiber. The term $\frac{P_k(z,t)}{hv_kA}$ can be interpreted as the photon flux (unit $\frac{photons}{m^2s}$) often used in laser rate equation models. In a realistic case, the model can comprise hundreds of optical channels requiring an equal number of power propagation equations (eq. 2.10) while, in contrast, there is only one rate equation for each of the ions' excited energy levels. The ground state population can always be eliminated using the total doping concentration as was done above. In a steady state, the left-hand side of eq. (2.11) vanishes and the differential equation is reduced to an algebraic equation, from which the fractional excitation $\frac{N_2(z)}{N_t}$ can be solved as

$$\frac{N_2(z)}{N_t} = \frac{\sum_k \frac{P_k(z)\alpha_k}{hv_k\zeta}}{1 + \sum_k \frac{P_k(z)\,(\alpha_k + g_k^*)}{hv_k\zeta}} \tag{2.12}$$

where the saturation parameter $\zeta = AN_t/\tau$ [29]. All the parameters in eq. (2.12) are non-negative and the numerator is clearly smaller than the denominator on the right hand side. This means, logically, that the fractional excitation is always between 0 and 1. Propagating light with large α_k and small g_k^* get absorbed and builds up excitation while channels with large g_k^* and small α_k stimulate emission, thus depleting excitation.

Unfortunately, eq. (2.12) is still coupled to eq. (2.10) so that the excitation cannot be calculated before the optical power evolution along the fiber is known but, on the other hand, the power cannot be integrated from eq. (2.10) either without knowing the excitation first. Consequently, an iterative procedure is needed to find the solution to these equations, which mathematically constitute a one-dimensional boundary-value problem. The boundary values are the input powers of the channels, some of them known on the "left" and some on the "right" the end of the fiber depending on their propagation directions. When the boundary values and the constants are known, the system of differential equations can then be solved numerically using either a shooting method or a relaxation method. The mathematical details of these algorithms are beyond the scope of this thesis but both involve guessing the unknown values of the dependent variable (optical power) and somehow refining the guess until the calculated boundary values are within a required error tolerance from the known boundary values.

In the time-dynamic case, solving the differential equations is conceptually more straightforward than in the steady state because no initial guesses are needed. The excitation and optical powers simply start from a known state, which is typically zero, and are stepped forward in time using some finite-difference method. The difficulty lies in the vast difference in time scales between propagation of light through the fiber (nanoseconds) to the excited state lifetime of up to milliseconds. Thus, an enormous number of small time steps is required to build up ion excitation starting from zero, making time-dynamic algorithms orders of magnitude slower than steady-state ones. Therefore, a steady state algorithm is preferable whenever the amplifier's transient behavior is unimportant and the inputs can be approximated as continuous-wave signals.

To solve the system of differential equations numerically, space (and possibly time in case of time-dependent inputs) must be discretized. In practice, the fiber is divided into N slices of equal size along its length with each optical channel and the ion excitation having a constant value within each slice. The number of required slices depends mainly on two things: the maximum slopes $\left(\frac{dP}{dz}\right)$ of the optical powers and the order of the numerical integration scheme. Very strong gain or absorption in a short length of fiber generally requires closely spaced slices for the numerical solution to follow the exponential function accurately, while fewer points are enough to describe slower changes in optical power. Similarly, a high-order algorithm, which evaluates numerical derivatives with high precision, requires substantially fewer points than the simple Euler method.

2.5 Ultrashort pulses

At the center of this thesis is the generation, shaping and amplification of ultrashort optical pulses. This section aims to briefly review the relevant theory of ultrashort pulses, starting with their qualitative properties followed by a mathematical description.

2.5.1 Qualitative description

Ultrashort optical pulses are wave-packets of electromagnetic energy ranging from picoseconds down to hundreds or tens of attoseconds in duration. Even though the term "ultrashort" lacks an official definition, there are some characteristics that distinguish ultrashort pulses from merely short pulses or continuous-wave radiation. Consequently, different physical phenomena must be taken into account when describing ultrashort pulse propagation in solid state media or their interaction with optical components such as diffraction gratings.

First, ultrashort pulses have a broad spectral bandwidth compared to CW lasers or atomic line light sources, such as low-pressure sodium lamps. Furthermore, these spectral components must have a fixed phase relationship that is absent from broadband thermal light. In time-domain, the different wavelengths being in phase gives rise to constructive interference manifested as an optical pulse. The pulse duration is inversely proportional to the spectral width when the spectral components are fully in phase. For example, a pulse with a 1 nm wavelength bandwidth at 1 µm has a minimum duration of roughly 1/300 GHz = 3.3 ps because a 1 nm wavelength bandwidth corresponds to a 300 GHz frequency bandwidth. The broadband spectrum means that ultrashort pulses are subject to dispersive effects, when the optical path length (or phase retardation) in an optical system is frequency-dependent. The dispersive effects can alter the pulse duration and the pulse's temporal shape in general.

Because an ultrashort pulse's spectral energy is concentrated within a narrow time window, the peak power can become very high, which is equivalent to a strong electric field amplitude and high intensity if the light is spatially confined to a small cross-sectional area. At high enough intensities, the polarization induced by the pulse in the material through which it propagates no longer depends linearly on the polarizing field. The resulting nonlinear optical effects generate new frequencies and in so doing can broaden and distort the spectrum of the pulse. At even higher intensity levels, normally transparent materials such as glass start to absorb the laser radiation via multiphoton absorption which can lead to the destruction of the material. Therefore, nonlinear effects usually limit the peak power of ultrashort pulses in some way.

2.5.2 Mathematical description

In the general case, ultrashort pulses can be described by their magnetic and electric field components ($H(\mathbf{r},t)$, $E(\mathbf{r},t)$) whose evolution is governed by Maxwell's equations. However, this description is mathematically cumbersome, obstructs physical insights from view and is not conducive to use in efficient numerical simulations. For these reasons, several standard approximations are normally made to simplify the mathematics of ultrashort laser pulses in optical fibers.

This thesis adopts the conventional description of ultrashort pulses as the product of a

sinusoidal carrier wave and an envelope function. This description requires the slowly varying envelope approximation, which states that the envelope must vary only a little over one cycle of the carrier wave. The approximation is valid when the pulse duration is much longer than a single optical cycle; a condition well satisfied by all but the shortest pulses because the cycle duration is only a few femtoseconds. As the starting point, this thesis takes the expression for the real electric field $\mathscr{E}(\mathbf{r}, t)$ by Agrawal [23], which already includes terms arising from the waveguiding properties of optical fibers:

$$\mathscr{E}(\mathbf{r}, t) = \frac{1}{2}\hat{x}\left\{F(x, y)A(z, t)\exp\left[i\left(\beta_0 z - \omega_0 t\right)\right] + \text{c.c.}\right\} \tag{2.13}$$

This expression describes a pulse propagating to positive z-direction. The pulse is linearly polarized with the polarization unit vector $\hat{x}$ pointing to x-direction. After this point, the polarization vector will be dropped, and a scalar form of the equation is used. The scalar approximation is usually made to simplify the mathematics even when there are two orthogonal polarization components. In this thesis, the whole laser system design is made of polarization-maintaining fibers, so the scalar equation is totally valid if we ignore the small amount of power (typically around 1 %) that leaks into the orthogonal polarization mode.

The second term $F(x, y)$ is the transverse spatial distribution of the pulse. For a pulse propagating in a single-mode optical fiber, this distribution is the fundamental fiber mode whose shape only depends on the fiber geometry, core radius and numerical aperture and not on z or t. For pulses in free space on the other hand, the transverse distribution would evolve during propagation due to diffraction. Because $F(x, y)$ is assumed constant, it is also omitted from now on. However, it will become relevant when discussing fiber nonlinearities, because the transverse size of the mode affects the pulse's peak intensity and thus the accumulated nonlinear phase shift.

The third term $A(z, t)$ is the slowly varying complex pulse envelope which determines the temporal shape and duration of the pulse. The evolution of $A(z, t)$ during propagation in an optical fiber is governed by the generalized nonlinear Schrödinger equation that will be introduced in section 2.6.4.

The remaining terms in equation eq. (2.13) have the following meanings. The exponential term is the sinusoidal carrier wave, where β_0 is the propagation constant of the fiber mode and ω_0 is the carrier angular frequency. They both affect the absolute phase of the pulse, which is physically uninteresting in most situations. The notation c.c. denotes complex conjugate, which is required to make the electric field a real quantity. Because the complex conjugate is used, the factor $1/2$ in the beginning is required to get the correct amplitude.

2.5.3 Complex amplitude

This section mostly follows the concisely presented material and notation in [30]. To further simplify the mathematics related to the complex envelope, the complex conjugate term is usually dropped along with the rapidly varying exponential term. The z-dependence of the envelope $A(z,t)$ can also be ignored (for now), which is only meaningful in the context of propagation in optical fibers or other solid-state media. The final, solely time-dependent formulation is called the complex amplitude of the pulse:

$$A(t) = \sqrt{I(t)}e^{-i\phi(t)} \tag{2.14}$$

where $\sqrt{I(t)}$ is the amplitude and $\phi(t)$ is the temporal phase of the pulse. Both of them are slowly varying compared to the carrier frequency. This definition also implies that the electric field is normalized according to the following equation for intensity:

$$I(t) = |A(t)|^2 \tag{2.15}$$

which excludes the constants permittivity and speed of light. Like the intensity, also the temporal phase can be solved from eq. (2.14) as

$$\phi(t) = -\arctan\left\{\frac{\mathrm{Im}[A(t)]}{\mathrm{Re}[A(t)]}\right\} \tag{2.16}$$

The pulse is completely defined by the three parameters: $I(t)$, $\phi(t)$ and ω_0 that was omitted but is still implicitly included. An important parameter related to the temporal phase is the instantaneous frequency $\omega_i(t)$:

$$\omega_i(t) = \omega_0 - \phi'(t) \tag{2.17}$$

The instantaneous frequency is a measure of how the carrier frequency changes with respect to time. However, it is not directly related to the Fourier frequencies, i.e. the spectrum of the pulse. For pulse with a flat or linearly varying temporal phase, the instantaneous frequency is constant. Second or higher order temporal phase variations lead to changing instantaneous frequency. Such a pulse is called to have chirp, which is a relevant concept for discussing dispersion.

When considering dispersive, frequency-dependent effects on the pulse, it is beneficial to describe the pulse in the frequency domain. This is achieved by taking the Fourier

transform of the time domain complex amplitude:

$$\widetilde{A}(\omega - \omega_0) = \int_{-\infty}^{\infty} A(t) e^{-i\omega t} dt \tag{2.18}$$

The inverse Fourier transform can be used to get back to the time domain.

$$A(t) = \frac{1}{2\pi} \int_{-\infty}^{\infty} \widetilde{A}(\omega - \omega_0) e^{i\omega t} d\omega \tag{2.19}$$

The frequency domain field can be separated into spectral intensity or spectrum S and spectral phase φ.

$$\widetilde{A}(\omega - \omega_0) = \sqrt{S(\omega - \omega_0)} e^{-i\varphi(\omega - \omega_0)} \tag{2.20}$$

Defined this way, the spectrum is centered at zero frequency (hence the subtraction of ω_0) because the carrier frequency was omitted from the temporal complex amplitude. However, it is more convenient to have the spectrum centered at ω_0, so it is typically shifted there with a minor violation of mathematical rigor. Therefore, the frequency domain envelope function is written simply as

$$\widetilde{A}(\omega) = \sqrt{S(\omega)} e^{-i\varphi(\omega)} \tag{2.21}$$

In complete analogy to the time-domain intensity and temporal phase, the spectral intensity and spectral phase can be solved from 2.21 to give

$$S(\omega) = \left| \widetilde{A}(\omega) \right|^2 \tag{2.22}$$

$$\varphi(\omega) = -\arctan \left\{ \frac{\mathrm{Im}[\widetilde{A}(\omega)]}{\mathrm{Re}[\widetilde{A}(\omega)]} \right\} \tag{2.23}$$

The phase of a real pulse can be arbitrary. In theoretical considerations however, it is typically expanded as a Taylor series whose components have different physical meanings like below

$$\begin{aligned}\varphi(\omega) =& \varphi(\omega_0) + \varphi'(\omega_0)(\omega-\omega_0) + \frac{1}{2}\varphi''(\omega_0)(\omega-\omega_0)^2 \\ &+ \frac{1}{6}\varphi'''(\omega_0)(\omega-\omega_0)^3 + \ldots\ldots\end{aligned} \tag{2.24}$$

To summarize, we have now two equivalent ways to describe an ultrashort pulse. It can either be defined in time domain by specifying $I(t)$ and $\phi(t)$ or in frequency domain with $S(\omega)$ and $\varphi(\omega)$. Additionally, the carrier angular frequency ω_0 is required to tell how fast the time domain field oscillates under the envelope or equivalently where the spectrum is centered. Both methods completely define the pulse and knowing either the time domain or frequency domain intensity and phase, we can obtain the other description by taking the (inverse) Fourier transform. Having two complementary forms is useful because some physical effects are more easily described in time domain and some in frequency domain.

2.6 Ultrashort pulses in optical fibers

When designing ultrafast lasers and amplifiers, the target is to obtain as short and intense pulses as possible. This requires mitigating and compensating for dispersion and nonlinearity, which mostly impair the system's performance, though sometimes these phenomena can be used for a positive effect. Especially in fiber-based ultrafast laser systems, dispersion and nonlinearity play a substantial role because the propagation distance in the solid-state medium is much longer than in free space bulk optic laser systems.

2.6.1 Gain, absorption and loss

Ultrashort pulses can lose energy to scattering and absorption and gain energy by stimulated emission in a laser active medium. These effects are primarily frequency-dependent and therefore, best handled in the Fourier domain where they act on the spectral amplitudes but not on spectral phases (ignoring the weak effect of gain and absorption on the complex refractive index). In optical fibers, background loss including Rayleigh scattering and absorption in fused silica varies slowly with wavelength. Though it plays a major role in long-range fiber optical telecommunications, fiber laser setups are typically short enough that the background loss can be neglected. In active fibers, the absorption and stimulated emission by the dopant ions is both strong and has a clear wavelength-dependence even over a few nanometers as covered in section 2.3. At each wavelength, an active fiber exhibits certain net gain or absorption depending on the excitation of the ion population. The main difficulty in modelling gain and absorption effects in the context of ultrashort pulses is that the excitation evolves over much longer time scales (ms) than the pulse (ps-fs). Therefore, it is cumbersome to fit all relevant physical effects in the same mathematical model. If an individual pulse is too weak to deplete the excitation considerably, the excitation can be estimated beforehand with a rate equation simulation whose result is then used to calculate net gain as a function of wavelength for the ultrafast

pulse modelling. Based on eq. (2.10), the net gain g_{net} at a certain frequency ω is

$$g_{net}(z,\omega) = [\alpha(\omega) + g^*(\omega)] \frac{N_2(z)}{N_t} - \alpha(\omega) - l \tag{2.25}$$

A steady state case is assumed so that the excitation depends solely on position in the fiber. The net gain can be both positive (gain) and negative (absorption). Its effect on the optical pulse is described mathematically in eq. (2.26).

$$\frac{\partial \widetilde{A}(z,\omega)}{\partial z} = \frac{g_{net}(z,\omega)}{2} \widetilde{A}(z,\omega) \tag{2.26}$$

The factor two in the denominator is required to account for the fact that the gain is applied to the spectral amplitude, not spectral power. The wavelength-dependence of net gain can modify the spectral shape (and through that the temporal shape) of a pulse propagating in an active fiber in addition to changing its total energy.

2.6.2 Dispersion

Dispersion refers to the frequency-dependence of refractive index or, in optical fibers, propagation constant, which causes different spectral components to travel at different velocities relative to one another. In other words, dispersion acts on the spectral phase of the pulse either by broadening the pulse width if the phase variation becomes larger or in some cases by compressing the pulse if the added dispersion negates pre-existing phase variation. Dispersion can hence be positive or negative and dispersive pulse stretching followed by compression is at the core of the CPA technique.

Most optical materials exhibit positive or normal dispersion, which means that longer wavelengths travel faster than shorter ones. The opposite is negative or anomalous dispersion, which means that shorter wavelengths travel faster. A pulse that has propagated in such medium and accumulated dispersion is called a chirped pulse. The sign of the accumulated dispersion can additionally be specified as either positive (or down) chirp or negative (or up) chirp.

When discussing dispersion in an optical fiber in the context of ultrashort pulses, the frequency-dependent propagation constant is normally expanded as a Fourier series at a relevant center frequency ω_0 as in eq. (2.27):

$$\beta(\omega) = \beta_0(\omega_0) + \beta_1(\omega_0)\Delta\omega + \frac{1}{2}\beta_2(\omega_0)\Delta\omega^2 + \frac{1}{6}\beta_3(\omega_0)\Delta\omega^3 + \ldots\ldots \tag{2.27}$$

where $\Delta\omega = \omega - \omega_0$ and the Taylor coefficients β_n describe the dispersive effects. β_0 is the

absolute propagation constant at the center frequency. The constant phase shift caused by β_0 does not affect the pulse shape and is therefore neglected. The first order term β_1 describes a linear phase shift along the pulse's spectrum. Based on the properties of the Fourier transform, such a linear spectral phase shift results in a constant time shift, i.e. the pulse propagates at a different velocity than the phase velocity, but its shape remains unaffected. The group velocity of the pulse, which is the inverse of β_1, determines the transit time through a certain material such as a section of optical fiber but is relatively unimportant and therefore normally disregarded in ultrafast pulse simulations.

The second order Taylor coefficient β_2, in contrast, has a strong impact on the pulse shape. This term causes a quadratic contribution to the spectral phase and describes the variation of the group velocity with frequency. In other words, different parts of the pulse travel at slightly different velocities, which causes the pulse to broaden if the frequency components were originally in phase but then move increasingly out of phase with each other. The pulse becomes linearly chirped, which means that its instantaneous frequency changes linearly with time. Since the phase is a simple function, this kind of pulse can be relatively easily compressed to back to its shortest possible transform-limited duration, in which all the frequency components are in phase.

The third and higher order dispersion components β_3, β_4, ... describe the dependence of β_2 on frequency. The number of terms required to correctly model pulse propagation depends on the pulse's spectral bandwidth, with more terms needed for broadband pulses. The result of β_2 not being constant is that the pulse's chirp is no longer linear but becomes more complex function, making it more difficult to compensate with normal optical elements.

Formally, the dispersive effects on the complex amplitude of a pulse are represented mathematically by eq. (2.28) with the summation stopped at the highest order dispersion component included.

$$\frac{\partial A}{\partial z} = -\left(\sum_{n\geq 2} \beta_n \frac{i^{n-1}}{n!} \frac{\partial^n}{\partial T^n}\right) A \tag{2.28}$$

Though this equation is written for time domain A, dispersion is typically handled in the Fourier domain where the time derivatives can be replaced with multiplication by $i\omega$.

2.6.3 Fiber nonlinearities

The rest of the physical processes affecting ultrashort pulses are nonlinear, i.e. somehow proportional to local irradiance and therefore best understood in time domain. Nonlinear effects are the main limiting factor of ultrafast fiber lasers because the optical field is transversely confined within a small core at most a few tens of wavelengths in diameter resulting in high peak irradiance and because the propagation distance in the fiber is

rather long.

Nonlinear effects generate new frequencies. If these frequencies lie within the gain bandwidth of the laser active ions in a fiber amplifier, the new frequencies can be amplified by stimulated emission in addition to the nonlinear process itself and seeded by ASE generated in the amplifier [31]. For this reason, nonlinearities can be stronger in fiber lasers and amplifiers than in passive fibers. The effectiveness of energy transfer to the new frequencies depends on polarization and therefore nonlinear effects are typically strongest for linearly polarized light [32, 33].

In this high-level discussion of nonlinear effects in optical fibers, we can thus write a rule of thumb for the strength of nonlinearity NL as follows:

$$\mathrm{NL} \propto K \int_0^L \frac{P_{\mathrm{peak}(z)}}{A_{\mathrm{eff}}(z)} dz \tag{2.29}$$

The nonlinearity is roughly proportional to propagation distance L and peak power P_{peak} divided by nonlinear effective area A_{eff} (which equals to peak irradiance in the fiber) while K is a constant of the order of unity representing the effect of polarization. Peak irradiance must be integrated over the propagation distance since the input power is either attenuated (in passive fibers) or amplified (in pumped active fibers).

To reduce nonlinearity in a fiber laser system, one can try to affect the different parameters in eq. (2.29). Typically, linear output polarization is desired, which requires the fiber-based power amplifier to operate at linear polarization as well. In some cases, circular polarization can be used in the amplifier and then converted to linear polarization at the output, thus decreasing nonlinearity through K [19]. The amplifier length L should also be minimized, especially in high-peak-power parts. This requires strong pump absorption in the active fiber (through high doping concentration) and proper cooling to handle the increased thermal load per meter of fiber. For pulsed operation, the peak power depends on average power and pulse duration. At a certain average power, peak power can then be kept modest by using long pulses, which is the idea behind chirped pulse amplification. Nonlinearity can also be mitigated by maximizing the effective area A_{eff}, which is the target of various specialty fiber designs.

For a more detailed understanding of nonlinear effects in optical fibers, the first point to note is that fused silica is an isotropic material so second-order nonlinear effects are very weak and third order effects dominate [23]. Thus, the main nonlinear effects in optical fibers are four-wave mixing (FWM), stimulated Raman scattering (SRS), stimulated Brillouin scattering (SBS) and optical Kerr effect giving rise to self-phase modulation (SPM) and cross-phase modulation (XPM). FWM requires the fulfillment of a phase-matching condition, which generally does not happen accidentally, so FWM can be neglected in ultrafast fiber amplifiers operating far from the zero-dispersion wavelength. XPM describes the interaction of multiple waves in the fiber via Kerr nonlinearity and does not play a role

in a linearly polarized fiber amplifier with only one propagating signal. SBS is automatically phase-matched and, in principle, has the lowest threshold of the fiber nonlinearities. However, its gain bandwidth is only $\approx$ 50 MHz meaning that, for two frequencies ν_1 and ν_2 at least 50 MHz apart, signal at ν_2 does not contribute to SBS generated by signal at ν_1. For this reason, SBS typically does not play a role with broadband ultrashort pulses even though it can severely limit the propagation of narrowband signals. Consequently, only the Kerr effect (SPM) and SRS are relevant for the laser system in this thesis and will be described in more detail below.

The optical Kerr effect is an automatically phase-matched third order nonlinear effect. It causes an intensity-dependent phase shift often described via the nonlinear refractive index

$$n = n_0 + n_2 I \tag{2.30}$$

where n is the total refractive index, n_0 is the normal "linear" refractive index, n_2 is the nonlinear refractive index and I is the optical intensity. Since $n_0 \approx 1.45$ and $n_2 \approx 2\text{-}3 \cdot 10^{-20}\,\mathrm{m^2\,W^{-1}}$ for fused silica at 1 µm, the nonlinear refractive index only plays a role at high intensities. The nonlinear refractive index manifests itself both in spatial and time domains. In the spatial domain, the transversely varying intensity profile of a high-power beam generates a refractive index distribution resembling a positive lens. This effect, known as self-focusing, is used to provide saturable absorption in Kerr-lens mode-locked bulk solid-state lasers. In ultrafast fiber lasers, self-focusing sets the ultimate peak power limit inside the fiber (about 4 MW at 1 µm) [34], though in practice, other effects such as SRS usually constrain the peak power to a lower value.

Unlike the spatial Kerr effect, the temporal Kerr effect cannot be neglected in ultrafast fiber lasers. In this context, the Kerr effect is called self-phase modulation to emphasize the fact the irradiance of the pulse modulates the pulse's own temporal phase. Mathematically, SPM operates on the complex amplitude of the ultrashort pulse according to eq. (2.31):

$$\frac{\partial A(z,t)}{\partial z} = -i\gamma |A(z,t)|^2 A(z,t) \tag{2.31}$$

where $|A(z,t)|^2$ is the optical power and γ is the nonlinear parameter, essentially a scaled version of the nonlinear refractive index n_2 that includes the effective area:

$$\gamma\left(\omega_0\right) = \frac{n_2\left(\omega_0\right)\omega_0}{cA_{\mathrm{eff}}} \tag{2.32}$$

where ω_0 is the (carrier) angular frequency and c is the speed of light in vacuum. Equation (2.31) tells us that SPM imposes a phase shift matching the irradiance of the pulse in time domain. In other words, the phase shift depends on the pulse shape. By itself, SPM does not affect the temporal amplitude of the pulse but changes the spectrum by both generating new frequencies and altering the phase of the existing frequencies.

The accumulated SPM nonlinearity in an amplifier system is often expressed using a single parameter, the B-integral:

$$B = \frac{2\pi}{\lambda} \int n_2 I_{peak}(z) dz \tag{2.33}$$

where n_2 is the nonlinear refractive index and $I_{peak}(z)$ is the peak intensity of the pulse at position z. The B-integral gives the nonlinear phase shift due to self-phase modulation experienced by the peak of the pulse. The leading and trailing edges of the pulse undergo smaller phase shifts, which approach zero where the irradiance goes to zero so the B-integral is a measure of the maximum nonlinear phase variation in the pulse.

In the frequency domain, SPM manifests as nonlinear group delay, which can be approximated as

$$d\phi/d\omega = B/\Delta\omega_{hw} \tag{2.34}$$

where $\Delta\omega_{hw}$ is the half width at half maximum of the spectrum [35]. At 1 µm wavelength and 5 nm spectral half width, a B-integral of 1 rad corresponds to a group delay variation of 106 fs. For this reason, the nonlinear phase shift should be kept as low as possible if the target is to obtain femtosecond pulses. Fortunately, some of the nonlinear phase shift can be compensated via second- and third order dispersion in the amplifiers and the compressor if CPA is used [36]. The remaining uncompensated part can distort the compressed pulse, for example generating side lobes which effectively decrease the maximum peak power of the main pulse.

Because the nonlinear phase shift follows the temporal pulse shape, some pulse shapes are less susceptible to nonlinear phase distortions than others. Notable examples are solitons in negative-dispersion media and parabolic pulses in active fibers with positive dispersion. Solitons are sech^2-shaped stable solutions of the nonlinear Schrödinger equation (NLSE) which can propagate long distances unchanged because the negative dispersion and nonlinearity completely cancel out each other [23]. Unfortunately, solitons are not readily usable in high-power fiber lasers because they are stable only at low energies and silica fibers at 1 µm do not exhibit negative dispersion. Parabolic pulses are asymptotic solutions to the NLSE in the presence of positive dispersion, self-phase modulation and gain [37]. For CPA, they could possibly be generated by a parabolic spectral

filter followed by a stretcher. As their name implies, these pulses have parabolic intensity profiles with quickly decreasing tails unlike Gaussian or sech^2 pulses. This pulse shape is beneficial since the nonlinear phase it accumulates has a parabolic shape, which equals to a linear chirp that is easily compensated with negative second order dispersion.

The second major nonlinear effect in ultrafast fiber lasers and amplifiers is stimulated Raman scattering. Raman scattering in general arises from the interaction of the propagating light with the vibrational energy states in a transparent material so that the scattered photons are frequency downshifted by the difference of the material's vibrational energy levels. A frequency up-shift is also possible, but its probability is much lower because the minimal occupation of higher vibrational energy states at room temperature. In fused silica, the Raman shift is approximately 13.2 THz [23], corresponding to 48 nm at 1040 nm. Under normal circumstances, the Raman effect is weak but existing photons at the Raman-shifted wavelength can stimulate further Raman scattering leading to a rapid transfer of power from the original signal to the Raman-shifted signal. Therefore, SRS sets a limit for peak power in a fiber laser system after which all additional amplification will only amplify the Raman signal. The presence of seed light at the Raman wavelength influences how quickly SRS becomes a problem. Therefore, it is beneficial to avoid ASE light at the Raman wavelength, perhaps even by spectral filtering, so that the Raman signal must grow starting from weak spontaneous Raman scattering only. Even though the Raman process is automatically phase-matched, dispersion plays a role at ultrashort pulse durations because the generated Raman pulse travels faster (in positively dispersive medium) than the original pulse and cannot be amplified further via SRS when the pulses no longer overlap temporally. In ultrashort pulse modelling, SRS is taken into account by using a Raman response function, which is based on experimental data for the material in question.

2.6.4 Generalized nonlinear Schrödinger equation

All the effects introduced in the previous sections can be combined into a single partial differential equation describing ultrashort pulse propagation in optical fibers, the generalized nonlinear Schrödinger equation (GNLSE) that is presented in eq. (2.35) [38]. There is no analytic solution to the complete GNLSE so numerical methods are required to solve it in specific cases. Using this equation, it is possible to propagate a pulse, represented by its complex amplitude $A(z,t)$, numerically through a fiber whose parameters are known. The GNLSE is presented here in time domain but, in practice, solving it requires Fourier-transforming between the time and frequency domain because some effects are more conveniently handled in one or the other.

$$\frac{\partial A}{\partial z} = \frac{g_{net}}{2}A - \left(\sum_{n\geq 2}\beta_n \frac{i^{n-1}}{n!}\frac{\partial^n}{\partial T^n}\right)A + i\gamma\left(1+\frac{1}{\omega_0}\frac{\partial}{\partial T}\right)\left((1-f_R)A|A|^2 + f_R A\int_0^\infty h_R(\tau)|A(z,T-\tau)|^2 d\tau\right) \quad (2.35)$$

The first term on the right-hand side describes the effect of net gain, written here for simplicity without its wavelength dependence, which is best applied in the spectral domain. The second term describes second and higher order dispersion, which is also best modelled in the spectral domain because calculating the time derivatives numerically is inaccurate [23]. The final terms correspond to the nonlinear effects. The time-derivative accounts for the self-steepening effect, which is only relevant for sub-picosecond pulses but included here for the sake of completeness. f_R is an experimental constant factor between 0-1 that describes the proportion of the Raman response of the total nonlinear response. Therefore, the term with $(1-f_R)$ corresponds to the optical Kerr effect and the term with f_R to SRS.

Simulating ultrashort pulse propagation in a CPA system using the GNLSE is a computationally intensive task since the simulation time grid must be be both broad to describe the long stretched pulse and dense to handle the very short compressed pulse at the same time. Fourier transforming that time grid is slow so the number of required transforms should be minimized by using an efficient algorithm. Traditionally, the split-step Fourier transform method has been used for solving the GNLSE [23]. The algorithm alternates between the frequency domain where it integrates the gain and dispersive effects and the time domain where it integrates the nonlinear effects. A more efficient fourth order Runge-Kutta in the interaction picture (RK4IP) method was described by Hult in 2007 [38]. This method allows integrating the nonlinear terms more accurately than the split-step method, thus obtaining the same accuracy with fewer computational steps. The number of steps can be further optimized by using an adaptive stepping algorithm, which estimates the local error after each step and adjusts the step size accordingly to stay within a predefined tolerance. This thesis uses the Conservation Quantity Error stepping method described in [39], which the author of that paper found to be more efficient than the earlier developed Local Error method [40]. The simulation algorithm was adapted to Python programming language from the Matlab code provided by the authors of [41] online [42]. The adaptation included adding support to frequency-dependent gain and dense output for B-integral computation. The code used to solve the GNLSE is included as Appendix A.

2.7 The principle of chirped-pulse amplification

Chirped pulse amplification is the most widely used method for generating high-energy, high-peak-power ultrashort pulses. The principle is simple [35]. The starting point is

a seed laser that emits low-energy pulses typically hundreds of femtoseconds or a few picoseconds in duration. These pulses cannot be directly amplified to high energy in any solid-state optical amplifier because the resulting very high peak power causes excessive nonlinearity, which can either distort the pulse or even destroy the amplifier medium. The solution to this problem is to apply a large amount of dispersion to the pulse before amplification to stretch the pulse in time-domain. This reduces the peak power and allows reaching a higher pulse energy. After amplification when the pulse is propagating in free space and no longer subject to strict peak power limitations, an equal amount of dispersion of opposite sign is used to compress the pulse down to its original duration and reach a high peak power useful in many applications. This works because amplification by stimulated emission generates copies of the original photons and thus preserves the spectral phase of the original pulse.

The above view of CPA is somewhat simplified because it does not take into account the fact that original pulse might already be chirped and that the amplifier medium causes additional dispersion, both of which must be compensated for by the stretcher and/or the compressor to reach transform-limited pulses. Assuming that nonlinearity plays a negligible role, the operation of a CPA system can be conveniently described in the frequency domain [35]. If the time domain complex amplitude of the input pulse is $A(t)$, then the spectral domain complex amplitude is

$$\widetilde{A}(\omega) = \int_{-\infty}^{\infty} A(t) e^{-i\omega t} dt = \sqrt{S(\omega)} e^{-i\varphi(\omega)} \tag{2.36}$$

The whole CPA system comprising a stretcher, amplifier(s) and a compressor has a transfer function

$$T(\omega) = G(\omega) e^{-i\sigma(\omega)} \tag{2.37}$$

where $G(\omega)$ includes the frequency-dependent gain in the laser active medium and the attenuation in the other components and $\sigma(\omega)$ includes the dispersion of the stretcher, compressor and the amplifier. The output pulse in the spectral domain is then simply

$$\widetilde{A}'(\omega) = T(\omega)\tilde{A}(\omega) = G(\omega)\sqrt{S(\omega)} e^{-i[\sigma(\omega)+\varphi(\omega)]} \tag{2.38}$$

and in time domain

$$E'(t) = \frac{1}{2\pi} \int_{-\infty}^{\infty} \tilde{E}'(\omega) e^{i\omega t} d\omega \tag{2.39}$$

The target in designing a CPA system is to make the gain $G(\omega)$ high enough to reach the desired pulse energy and flat enough that the spectrum does not narrow during amplification, because the spectral width determines the minimum attainable pulse duration. The spectral phase $\sigma(\omega) + \varphi(\omega)$ by contrast should be made as close to zero as possible to actually compress the output pulse to its transform-limited duration. In other words, the spectral phase delays of the input pulse, the stretcher, the amplifier and the compressor should cancel each other out completely. The challenge lies in the fact that the stretcher and the compressor should provide massive amounts of dispersion to reach stretching ratios of up to >1000:1 while still making the fine-tuning possible to reach zero phase variation after the compressor. The problem is complicated further by the nonlinear phase contributions that were neglected in this simplified description of CPA, and managing nonlinearity is especially important in fiber-based CPA systems. In some cases, it can also be possible to benefit from self-phase modulation to compensate for gain narrowing in the amplifiers [43].

2.8 Dispersive elements for pulse stretching and compression

This section covers several different pulse shaping elements that have been used in the scientific literature to stretch or compress ultrashort laser pulses. Special emphasis will be placed on the elements finally chosen for the chirped pulse amplification design in this thesis: a chirped fiber Bragg grating (CFBG) for stretching and a bulk transmission grating pair for compressing the pulses. The discussion will be from the point of view of working with pulses at 1 µm wavelength.

2.8.1 Fiber spool stretcher

The simplest possible dispersive element in a fiber laser system is a long spool of passive optical fiber. This kind of stretcher was used in the initial demonstration of the chirped pulse amplification technique [4]. At 1 µm, single-mode optical fiber has positive second order and third order dispersion. Their proportion is naturally fixed by the specific fiber's parameters, but the total dispersion can otherwise be relatively easily tuned by changing the fiber length. A fiber stretcher can operate over an extremely broad bandwidth without clipping the pulse's spectrum, though higher order dispersion can become problematic with broad-band pulses. Furthermore, a fiber spool stretcher is straightforward to integrate into an all-fiber laser system without free-space alignment issues. Therefore, a fiber spool can also be used in combination with some other stretcher type. The input pulse energy to a fiber stretcher must be low enough to prevent the accumulation of nonlinear phase and, in the worst case, stimulated Raman scattering during the long propagation distance in the fiber. Using weak pulses in combination with the propagation loss in the fiber might necessitate additional amplification after the pulse has been stretched.

2.8.2 Chirped fiber Bragg gratings

A fiber Bragg grating (FBG) is a phase grating formed by a weak periodic refractive index modulation in the core of an optical fiber [44]. It can be fabricated by exposing a photosensitized fiber to UV radiation whose intensity pattern matches the desired refractive index modulation [45]. The absorption of UV light in the glass locally modifies the chemical bonds and, consequently, the refractive index. For some FBG designs, femtosecond infrared pulses can be used, which interact with the glass via multiple-photon absorption [46].

The simplest type of FBG is a uniform FBG with a constant modulation period and amplitude. Given strong enough index modulation and sufficient length, a uniform FBG acts as a high-efficiency narrow-band distributed reflector at the Bragg wavelength [44]:

$$\lambda_B = 2n_{\text{eff}}\Lambda \tag{2.40}$$

where n_{eff} is the effective group index of the fiber mode and Λ is the grating period, which together determine the reflection wavelength. Uniform fiber Bragg gratings are useful as fiber optic sensors, filters in optical communications, or cavity end mirrors in fiber lasers but do not provide dispersion.

However, if the period of modulation changes along the length of the FBG, different wavelengths are back reflected at different positions and those reflected farther along the grating are delayed with respect to the wavelengths reflected at the start of the FBG. Consequently, this kind of chirped fiber Bragg grating (CFBG) has a broader reflection band and acts as a dispersive element. This is demonstrated in fig. 2.3.

The reflection bandwidth of a CFBG depends on the grating periods at the start and at the end of the grating and can be estimated from eq. (2.41).

$$\Delta\lambda_B = 2n_{\text{eff}}\Delta\Lambda \tag{2.41}$$

where $\Delta\lambda_B$ is the variation of the Bragg wavelength (the grating chirp) and $\Delta\Lambda$ is the variation of the grating period. The maximum time delay generated by an CFBG between the spectral components reflected at the opposite ends of the grating is simply the round-trip time of the light reflected at the back end given by [47]:

$$\Delta t = \frac{2L}{v_g} \tag{2.42}$$

where L is the physical length of the grating and $v_g = c/n_{\text{eff}}$ is the group velocity of the

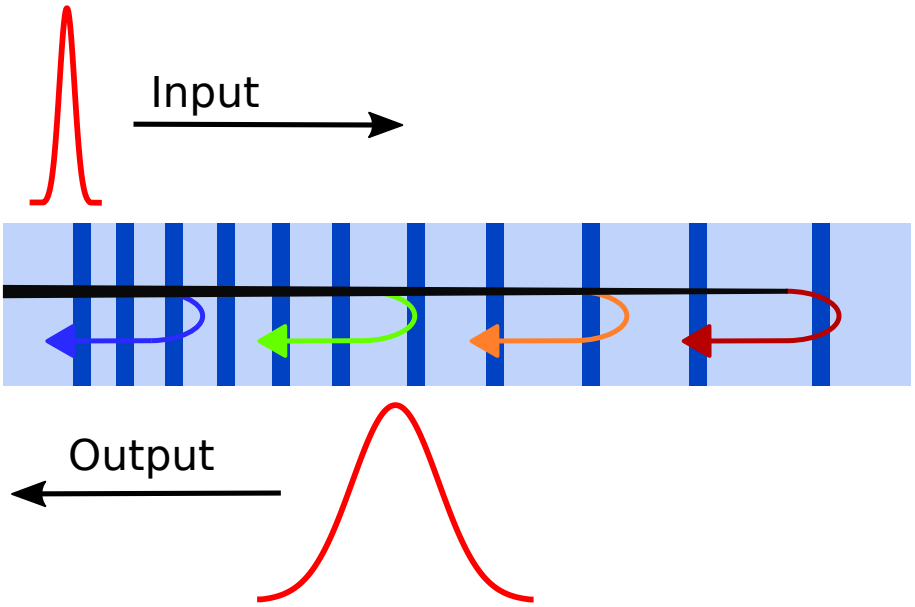

Figure 2.3. *Schematic of a chirped fiber Bragg grating. The group delay of a CFBG varies strongly between wavelengths reflected at different ends of the grating.*

pulse in the grating. Therefore, the second order dispersion of a CFBG is approximately

$$D = \frac{\Delta t}{\Delta \lambda_B} \tag{2.43}$$

in units of ps/nm [47]. Equations (2.41)–(2.43) represent only rough limits of a chirped FBG's operation. A more accurate understanding would require solving the coupled mode equations for the forward and backward propagating waves in the grating using the real refractive index modulation [44], which is outside the focus of this thesis.

When fabricating a CFBG, there is great flexibility in choosing its reflection bandwidth and dispersion, though a compromise must be made between the two since the grating cannot be made arbitrarily long. For a fixed grating length, increasing the reflection bandwidth reduces dispersion since the Bragg wavelength varies more rapidly. Within the maximum group delay limit imposed by the length of the CFBG, it is also possible to design a specific dispersion profile. In the simplest case, the grating period changes linearly, resulting in purely second order dispersion. However, the grating period can also change nonlinearly, giving rise to third and higher order dispersion of preferred sign and magnitude [48]. In essence, a CFBG can be fabricated to match the desired specifications with considerable freedom.

Afterwards, the dispersion of a CFBG is still tunable to an extent by stretching or heating, which slightly changes the grating period [47]. It can also be flipped around to reverse the sign of dispersion. However, the absence of stronger dispersion tuning and the inability to change the reflection bandwidth mean that a CFBG is less flexible than a fiber spool and must be carefully designed beforehand for the intended application. Another

disadvantage is that a CFBG, which operates only in reflection, requires a lossy optical circulator to be incorporated in a feed-forward fiber amplifier system.

2.8.3 Chirped volume Bragg gratings

Volume Bragg gratings are the bulk component equivalents of fiber Bragg gratings. Their fabrication is also similar, involving either UV or femtosecond IR laser writing of a periodic refractive index pattern in photosensitive glass material [49]. As in a chirped FBG, the period of a chirped volume Bragg grating (CVBG) changes along its length, imposing a strong dispersive phase shift to the reflected beam, which means that using a CVBG is a highly compact way to provide dispersion.

As a bulk component, a volume Bragg grating can accommodate beam diameters up three orders of magnitude larger than an FBG (millimeters instead of micrometers) [49]. This makes volume Bragg gratings usable for high-power operation. In bulk CPA systems, a single chirped volume Bragg grating can be used as a perfectly matched stretcher and compressor simultaneously by launching the beam into the grating from opposite ends because the two reflected beams acquire phase shifts of equal magnitude but opposite sign. In fiber laser systems, using a VBG this way is less attractive since an equivalent FBG stretcher is far preferable to a free-space VBG one. However, it is possible to use a matched pair comprising a CFBG and a CVBG for similar effect [50].

High-power volume Bragg gratings represent emerging technology compared to bulk diffraction gratings [51] and cost considerably more. The tunability of volume Bragg gratings is practically non-existent since they cannot be stretched like their fiber-based counterparts. Therefore, a CVBG must be optimized strictly for a specific input pulse during manufacturing and cannot be used for other wavelengths or differently chirped pulses. On the negative side, this makes a CVBG a poor choice for prototyping a laser system when the required pulse parameters are partly unknown. On the other hand, the fact the a VBG can be made to match a desired dispersion specification makes it an attractive option for mature laser system designs.

2.8.4 Bulk diffraction gratings

An optical diffraction grating is a periodic groove structure scratched or etched on a reflective or transmissive substrate. The distance between the grooves is comparable to the wavelength of light, whose interaction with the grating is therefore heavily wavelength-dependent. A diffraction grating works by bending an incident beam of light into several diffraction orders, i.e. directions, and within each diffraction order into its spectral components. This translates to optical path length differences between wavelengths, giving rise to group delay dispersion. This section covers the use of bulk gratings for pulse stretching and compression starting with methods to maximize the diffraction efficiency (power going to a single diffraction order) and then handling the dispersive properties of gratings.

The operation of a bulk diffraction grating is governed by the grating equation, which is

$$\Lambda \cdot (\sin\theta_I + \sin\theta_D) = m\lambda \tag{2.44}$$

for a reflection grating and

$$\Lambda \cdot (-\sin\theta_I + \sin\theta_D) = m\lambda \tag{2.45}$$

for a transmission grating where Λ is the grating period, θ_I is the incidence angle, θ_D is the diffraction angle, the integer $m = 0, \pm1, \pm2, ...$ is the diffraction order and λ is the wavelength [52]. The following sign convention is used for the angles: all angles opening counter-clockwise from the surface normal are positive, and angles opening clockwise from the surface normal are negative. The rest of this section uses the transmission grating equation eq. (2.45) as the starting point but applies equally well to reflection gratings with the relevant sign changes.

The separation of the diffracted wavelengths from each other is called angular dispersion and can be calculated from eq. (2.45) by solving for θ_D and then differentiating with respect to λ [53]. The result is

$$\frac{d\theta_D}{d\lambda} = \frac{m}{\Lambda \cos\theta_D} \tag{2.46}$$

Several important conclusions can be drawn from this equation. First, the magnitude of the diffraction angle grows with wavelength, i.e. longer wavelengths are diffracted more strongly. This is intuitively understandable since diffraction as a phenomenon becomes important only when light interacts with wavelength-scale structures. If the wavelength were much shorter than the grating period one would not expect noticeable diffraction to happen. Second, high diffraction orders m result in stronger angular dispersion. While higher diffraction orders of up to $m > 100$ are indeed used in some high-resolution spectrometers based on specialized Echelle gratings [53], only the first order is usable in high-power pulse compression because the diffraction efficiency of higher orders is too weak [54]. Another way to increase angular dispersion is to decrease the grating constant Λ, again since diffraction is stronger when the wavelength and the diffracting structure are about the same size. However, a too small grating constant results in no valid diffracted solutions to the grating equation.

The absolute lower limit for the grating period is

$$\Lambda \geq \lambda/2 \tag{2.47}$$

as set by the grating equation:

$$|m| \frac{\lambda}{\Lambda} = |\sin\theta_I + \sin\theta_D| \leq 2 \tag{2.48}$$

because the sum of the sines must be always less than or equal to 2 and $|m|$ is 1 for the lowest diffraction orders. Therefore, if the grating constant were smaller than $\lambda/2$, the only solution to the grating equation would be the non-diffracted zeroth order $m = 0$. In other words, eq. (2.47) also gives the longest wavelength, at which a certain grating still works. At the limit, the grating is operated at grazing incidence $\theta_I = 90°$, which is not practical so the grating period should be slightly above the limit if maximum dispersion is desired in a real optical system.

There is also a further limitation to the incidence and diffraction angles related to diffraction efficiency. To maximize diffraction efficiency, gratings are typically used in the Littrow configuration where the incidence angle is equal to the first order diffraction angle. For transmission gratings, this means that $m = -1$ and $\theta_D = -\theta_I$ in the adopted sign convention, which leads to the following equation for the Littrow angle of incidence:

$$\sin\theta_L = \frac{\lambda}{2\Lambda} \tag{2.49}$$

Inserting this into the grating equation gives

$$\sin\theta_D = \frac{\lambda}{2\Lambda} = \left(m + \frac{1}{2}\right)\frac{\lambda}{\Lambda} \tag{2.50}$$

which has solutions only for $m = 0$ and $m = -1$ if $\frac{\lambda}{\Lambda} > \frac{2}{3}$, in which case all the other diffraction orders are suppressed. Still, most of the incident power could go to the zeroth instead of the first order. The first order diffraction efficiency can be maximized by shaping the grating grooves in a specific way. While the groove shape is not present in the grating equation and does not affect a grating's dispersion properties, it has a major impact on the diffraction efficiency. Pulse stretching and compression typically make use of blazed gratings (see fig. 2.4), whose grooves are triangular with facets angled to the grating surface. Blazed gratings are specifically designed to be used at the wavelength, at which the Littrow angle matches the blaze angle, and their diffraction efficiency decreases at wavelengths further away from that design wavelength. Gratings are also typically

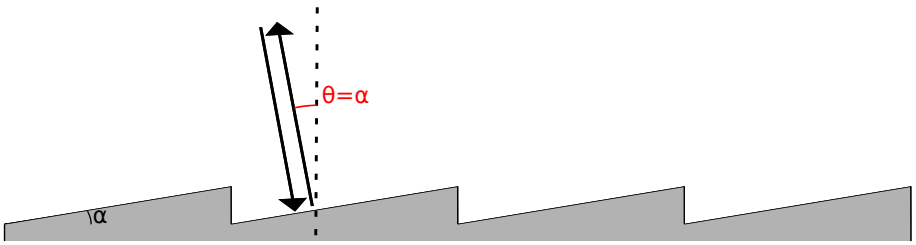

Figure 2.4. *Schematic of a blazed reflection grating with blaze angle α. The incidence and diffraction angles are equal to each other (θ) and to the blaze angle in Littrow configuration.*

polarization dependent, and the diffraction efficiency is higher for s-polarization, in which the electric field of the incident light is parallel to the grating lines.

In 1969, Treacy [55] demonstrated that a pair of identical gratings can be used to generate negative second order dispersion for pulse compression. His original design comprised only two reflection gratings, but the configuration was later refined to include a back reflecting mirror for a double pass in the system [56]. A practical version for high-power pulse compression in shown in fig. 2.5.

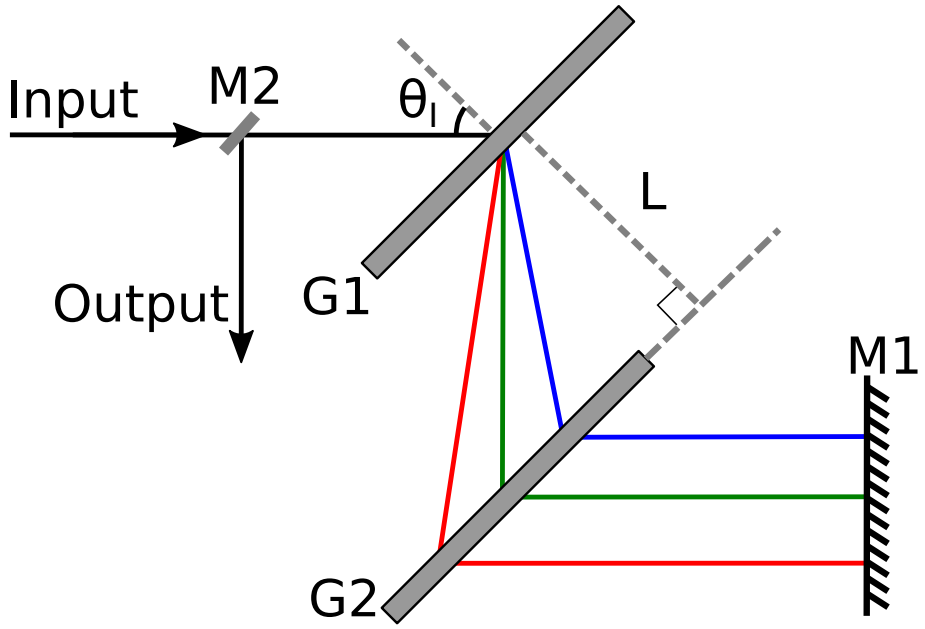

Figure 2.5. *Schematic of a transmission grating compressor operated at Littrow configuration. G1, G2 = transmission gratings, M1, M2 = mirrors, L = grating separation, θ_I = incidence angle*

In the grating compressor, the incident beam first encounters the grating G1, which separates the beam to its spectral components. A second identical grating G2 placed parallel to G1 is then used to parallelize the wavelength components. At this point, the beam has experienced negative group delay dispersion since the longer wavelengths have propagated a longer optical path than the shorter wavelengths. However, the beam is also spatially chirped since the wavelength components no longer perfectly overlap in space. In practice, a real finite-sized beam (unlike the rays in fig. 2.5) would become elliptical.

This can be avoided by including a mirror M1 (or two additional gratings) so that the beam propagates back the way it came due to reciprocity of diffraction. As a result, the spatial chirp is eliminated and the beam experiences twice the amount of dispersion but at the cost of higher diffraction losses [56]. To separate the output beam from the incident beam, the mirror M1 can be slightly tilted upwards or downwards and the exiting beam can then be captured with the small mirror M2.

The dispersion generated by the grating compressor depends on wavelength, incidence angle θ_i, grating separation L and the grating period. The second and third order dispersion terms are shown in eqs. (2.51) and (2.52) [35].

$$\frac{d^2\varphi}{d\omega^2} = -\frac{Nm^2\lambda^3 L}{2\pi c^2 \Lambda^2}\left[1-\left(-m\frac{\lambda}{\Lambda}-\sin\theta_i\right)^2\right]^{-3/2} \tag{2.51}$$

$$\frac{d^3\varphi}{d\omega^3} = -\frac{3\lambda}{2\pi c}\frac{1+\frac{\lambda}{\Lambda}\sin\theta_i-\sin^2\theta_i}{1-\left(\frac{\lambda}{\Lambda}-\sin\theta_i\right)^2}\frac{d^2\varphi}{d\omega^2} \tag{2.52}$$

where $N = 2$ is the number of passes when using the back-reflecting mirror and $m = -1$ is the diffraction order. The second order dispersion is always negative and the third order dispersion always positive. For a given pair of gratings, the distance between them and the incidence angle are freely tunable parameters, though θ_i should be kept close to the Littrow angle for high diffraction efficiency. Transmission gratings have an advantage over reflection gratings in that they can be operated at exactly the Littrow angle since the incident and diffracted beams are on different sides of the grating and therefore angularly separated. On the negative side, the material in transmission gratings contributes a small amount of positive dispersion, which might be problematic for the shortest pulses.

Analogous to FBGs and VBGs, the transverse size of a bulk grating limits the maximum optical path difference between the spectral components of a pulse and therefore the dispersion obtainable from a grating stretcher or compressor. The pulse's spectral bandwidth only affects the angular dispersion, i.e. how far from each other the gratings should be placed so that the beam completely fills the second grating's aperture in one direction. The required grating size can be approximated from angular dispersion from eq. (2.46), the diffraction angle and the grating separation.

A grating pair can also be modified to generate positive second order dispersion by adding two lenses, which was first proposed by Martinez [57]. The design is shown in fig. 2.6. In this configuration, the same equations for dispersion eqs. (2.51) and (2.52) still hold but the grating separation L can be effectively made negative by placing the gratings closer to the lenses than the focal length f. In principle, this allows designing matched gratings stretchers and compressors, whose dispersion components balance each other out perfectly. In practice, however, the lens telescope's chromatic aberration can cause

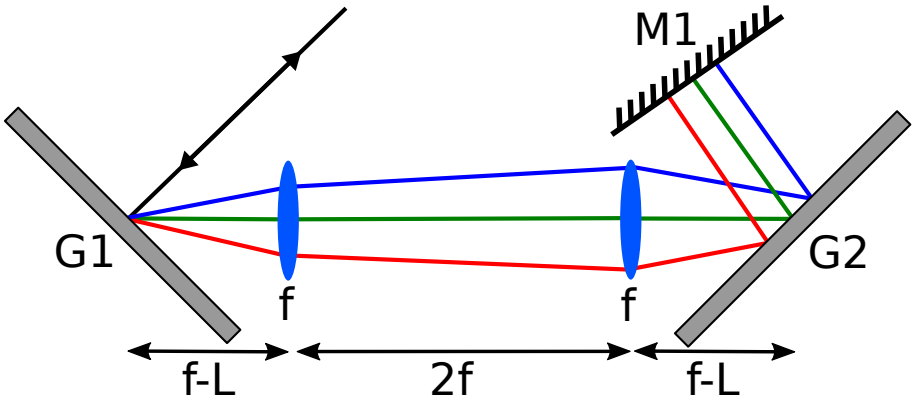

Figure 2.6. *Schematic of a grating stretcher with two identical reflection gratings and lenses with focal length f.*

phase distortions, and for this reason all-reflective stretcher designs such as the Öffner stretcher have later been developed [58].

Using the Martinez grating pair, it also possible to access the Fourier plane of the pulse by placing the gratings and lenses in a 4f-configuration. Then, a phase plate or a spatial light modulator can be placed at the Fourier plane to shape the spectral phase with an arbitrary function. Some high-end CPA systems use this kind of setup for more complex phase compensation [5, 19].

2.8.5 Bulk prisms

In addition to gratings, the wavelength-dependent refraction in prisms is also a source of angular dispersion [59] and a prism pair can be used to build a compressor or stretcher similarly to a grating pair. The scheme of a prism compressor is shown in fig. 2.7.

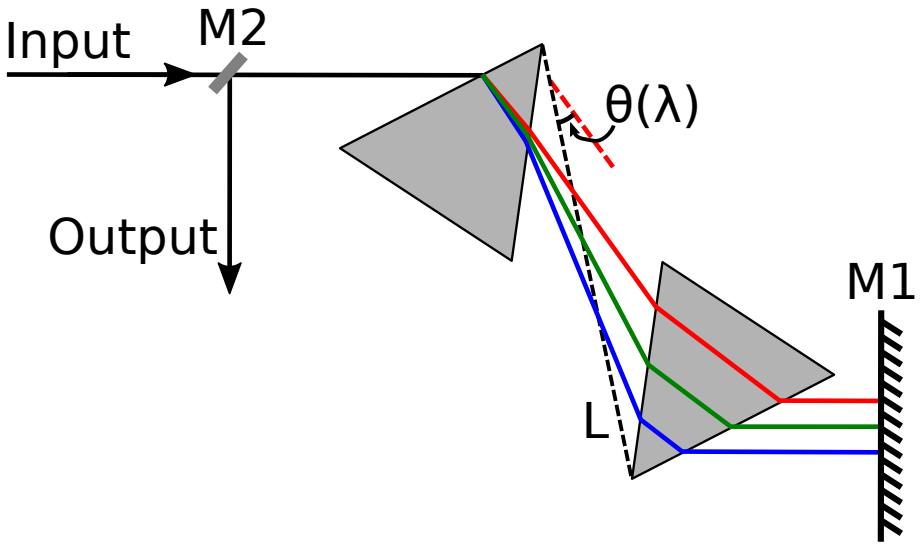

Figure 2.7. *Schematic of a prism pair compressor, which works on the same principle of angular dispersion as the grating pair compressor in fig. 2.5. The dispersion is defined in terms of the angle θ and path length L of a reference ray going through the apices of the prisms.*

However, it is difficult to obtain large negative dispersion because the angular dispersion is typically weak even in high-index glass and partially offset by the positive dispersion of the bulk glass material. In the example calculated in [35], a grating pair generates roughly two orders of magnitude higher dispersion than a comparable prism pair. For this reason, a prism pair is more suitable for fine-tuning than generating massive amounts of dispersion. On the positive side, a prism pair operated at Brewster's angle or with proper anti-reflection coating has higher transmission than a grating pair. By inscribing gratings onto the prisms to create so called "grisms" it is also possible to create a compressor, in which both second and third order dispersion are negative [60].

3 HIGH-LEVEL LASER SYSTEM DESIGN

The purpose of this chapter is to describe the structure of the CPA system qualitatively and explain and justify the choices made when designing it, including comparisons to alternative solutions. The main novelty of this system is the use of a tapered fiber amplifier together with the CPA technique. The laser system is designed for 1040 nm central wavelength, which more optimal for amplification in the Yb^{3+}-doped tapered fiber than the typical low-power seed laser wavelength of 1030 nm.

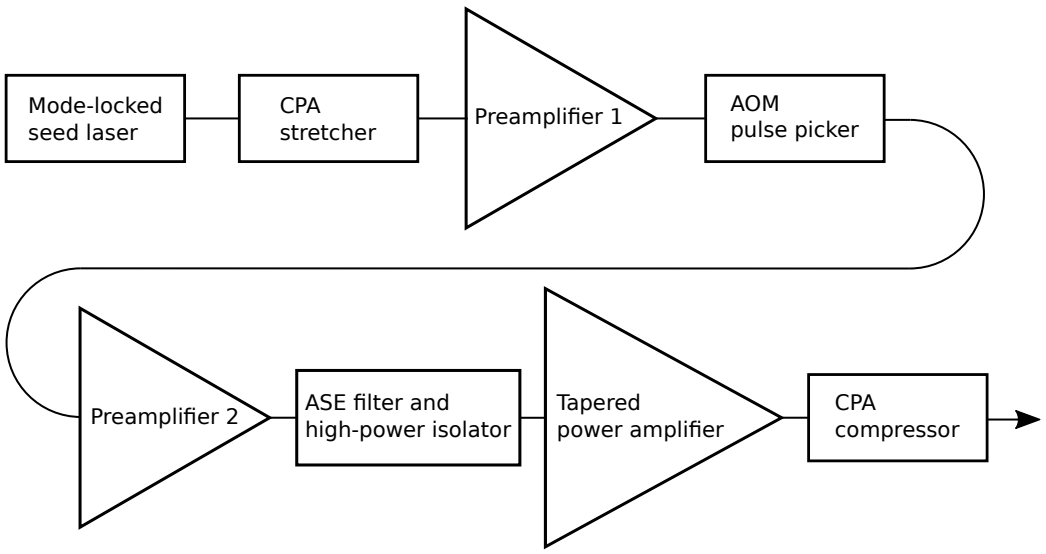

Figure 3.1. *High level scheme of the CPA laser system.*

A high-level schematic of the laser system is shown in fig. 3.1. The design is based on the master-oscillator-power-amplifier principle, in which the output of a weak seed laser is modified and amplified by a number of successive elements. The first element is the seed laser, which is a mode-locked fiber laser generating low-energy ultrashort pulses at a relatively high repetition rate. The seed pulses are slightly positively chirped but still much too short to be amplified to high pulse energy. This is where the CPA technique comes into the picture. The seed pulses are first stretched in a strongly dispersive component, whose function is to increase the pulse duration by more than an order of magnitude compared to the original pulses. At the same time, the stretcher is also lossy so that the pulse train then requires amplification in the following core-pumped preamplifier 1. After that, the pulses propagate through another lossy component, the pulse picker, which is essentially a fast optical switch that can block some pulses and transmit others. The pulse picker reduces the pulse train's repetition rate so that the energy gained in the further

amplifiers is shared between fewer pulses to enable higher energy per pulse later at the output. Besides having non-negligible excess loss, the pulse picker causes more than an order of magnitude drop in signal power by rejecting most of the pulses. Consequently, the pulse train must be amplified in another core-pumped preamplifier before it can be coupled into the tapered power amplifier through a high-power isolator. The final element after the amplification stages is the compressor, a strongly dispersive element, which compensates for the stretcher's dispersion, the pulse's initial chirp and the dispersion accumulated in the amplifier chain. The desired end result is a high-peak-power ultrashort pulse that is as close to the transform limit as possible and does not show significant side pulses.

The following sections will provide a detailed view into each sub-assembly in the CPA system and discuss the design choices and trade-offs associated with it. The trade-offs are mostly related to performance, i.e. the optical parameters of the output pulse train, and the ways to maximize it, but the commercial motivation of the project puts additional emphasis on cost, simplicity and robustness of the laser design. Actual results, experimental in the case of the seed laser and simulated for the rest of the system are presented in chapter 4.

3.1 Seed laser

Choosing or building a suitable seed laser is essential for realizing a performant CPA system. The seed laser generates the initial pulse train that is then sculpted and amplified by the subsequent elements. In some limited respect, the amplifier stages can compensate for less than ideal seed operation, but a suboptimal seed would drive up the complexity and cost of the laser system even in the best case. The seed does also place a few hard limits on the system's performance that cannot be circumvented by changes in the amplifiers.

The most important parameter of an ultrafast seed laser is arguably the quality of its pulses, which in this context should be understood as the focusability of the pulsed energy in time domain. A short pulse duration necessarily requires a broad spectrum based on the Fourier relation between the time and frequency domains. However, a broad spectrum alone is not a sufficient condition for obtaining clean ultrashort pulses. Especially fiber-based seed lasers generate initially chirped pulses that, in principle, could have such a complex spectral phase that they cannot be properly compressed with normal optical elements. For use in a practical system, the seed pulses must therefore also have a well-behaved spectral phase in addition to a broad spectrum. A small exception to the previous requirements is that an originally narrow spectrum can be broadened by self-phase modulation during propagation in an optical fiber, but the resulting nonlinear phase can then hinder perfect pulse compression unless the pulse shape is carefully chosen. A broad seed spectrum is also beneficial in a CPA system for practical reasons since the dispersion required to stretch or compress a pulse to a certain duration is directly

proportional to its spectral width. Therefore, a broad seed spectrum leads to a more compact laser setup if, for example, a fiber spool stretcher can be shorter or the gratings in a compressor can be closer to each other. Finally, the seed spectrum should lie within the optimal gain bandwidth of the power amplifier and preferably at a wavelength where wavelength-selective components such as filters, wavelength-division multiplexers and gratings are available commercially.

Besides the capability of generating short pulses, the seed laser's repetition rate is also an influential parameter. The majority of ultrafast seed lasers (except gain-switched diodes) are mode-locked so their fundamental repetition rate has a fixed value based on the cavity length. The seed's repetition rate then represents the maximum repetition rate of the laser system but lower rates can be obtained by using an external pulse picker to block every nth pulse. A pulse picker only enables repetition frequencies that are fractions of the original one and also causes a loss proportional to the number of pulses blocked out. Therefore, having seed repetition rate close to the final repetition rate is beneficial to avoid excessive losses. In the best case, the seed would generate at the correct repetition rate without need for a pulse picker, reducing both cost and complexity of the laser system. In practice, the cavity of a low-repetition-rate mode-locked laser would have to be unpractically long. For example, a 1 MHz fiber ring laser would require 200 m of fiber in the cavity, which would lead to problems with very high cavity dispersion. For this reason, mode-locked seed lasers typically have high repetition rates and must be pulse-picked. Tunability of the seed repetition rate would also be a beneficial quality but that would require cavity length tuning with a free space optical delay line, a complexity that is in most cases best avoided.

Apart from the pulse quality and the repetition rate, a seed laser's average power also plays a role in its suitability for a CPA system. Since a mode-locked laser typically generates very little ASE, the average power and pulse energy are directly related by the repetition rate, but average power is the more relevant parameter when considering amplification. The seed power should be at least enough to saturate the first preamplifier to avoid excessive ASE generation. For single-mode fiber amplifiers, the seed power would optimally be of the order of 1 mW, which is not a difficult requirement to satisfy. Still, a high seed power leaves more leeway in designing the preamplifiers as lossier components and less powerful pump diodes can be selected.

From the engineering point of view, a seed laser candidate's cost and compatibility with the amplifiers' fiber-based design must also be evaluated. In the scientific literature, many fiber-based CPA systems use bulk solid-state lasers as their seed sources [19, 43, 61]. The technology of bulk solid-state lasers is mature, and these lasers generally offer excellent performance, specifically in terms of a high pulse energy and a short pulse duration, which explains their popularity in academic work aiming to overtake earlier performance records. However, using a fiber-based seed laser offers some tangible benefits for a commercial CPA system not solely focused on performance. For example, using a bulk solid state laser as seed necessarily makes the laser system more susceptible to align-

ment issues since the free space seed beam must be coupled into the single-mode fiber amplifiers. Second, a fiber laser is relatively cheap, robust and quick to assemble from commercial components once the design has been fixed. A fiber laser fits into a small volume and does not require servicing due to optical misalignment. For these reasons, the laser system described in this thesis uses a fiber-based seed laser. A fiber-coupled gain-switched diode laser would have similar benefits but was rejected because of its poor pulse quality. In the future, a diode laser could possibly be used with extensive pulse shaping.

There are numerous possible designs for ultrafast fiber lasers at 1 µm. The most important differentiating factors among them are the polarization state and dispersion in the cavity as well as the mode-locking technique. For reliable long-term operation, the seed laser should be built with polarization maintaining fibers. Otherwise environmental changes such as temperature fluctuations would disturb the polarization state in the cavity, destabilizing the laser. For the sake of reliability, the laser should also minimize the use of free-space sections, preferring fiber-coupled micro-optical components instead.

Ultrafast fiber laser cavities are divided into different categories based on their cavity dispersion. Soliton fiber lasers have cavities with exclusively negative dispersion. Building a soliton fiber laser at 1 µm is not possible since optical fibers exhibit positive dispersion, which tends to broaden the propagating pulse together with SPM. However, the overall cavity dispersion can be made close to zero or negative by adding an element with strong negative dispersion, such as a chirped fiber Bragg grating, into the cavity. Such cavities are called stretched-pulse or dispersion-managed fiber lasers. Relatively recently in 2006, it was demonstrated that a dispersion compensating element is not required if the cavity contains a spectral filter instead [62]. The filter shortens the pulse by cutting the extreme wavelengths from its spectrum, which correspond to the pulse's edges in time domain. This kind of all-normal-dispersion (ANDi) fiber laser is appealing owing to its simplicity and cost-efficiency while also being able to generate high-energy pulses. Therefore, an ANDi design was selected for the seed laser in this thesis.

The actual mode-locking methods used in ANDi lasers include nonlinear polarization rotation (NPR) [62], nonlinear optical/amplifying loop mirror (NOLM/NALM) [63], Mamyshev oscillator [64] and semiconductor saturable absorber mirror (SESAM) [65] based designs. While the NPR technique can generate high quality pulses with broad spectra, it requires that the polarization state can evolve inside the cavity, and the best designs typically use a number of free space components for polarization adjustment. Therefore, NPR must be ruled out based on the earlier reliability requirements. Mamyshev oscillator and NALM designs would fulfill the general requirements, but we opted for a SESAM based design because of our extensive experience with SESAM mode-locked fiber lasers.

A schematic of the experimentally built laser cavity is shown in fig. 3.2. Arriving at this design was the result of testing numerous slightly different designs. Most of the details of that work are excluded from this thesis to keep the focus on the chirped pulse amplification. Instead, this section provides a short discussion on the design choices and the later

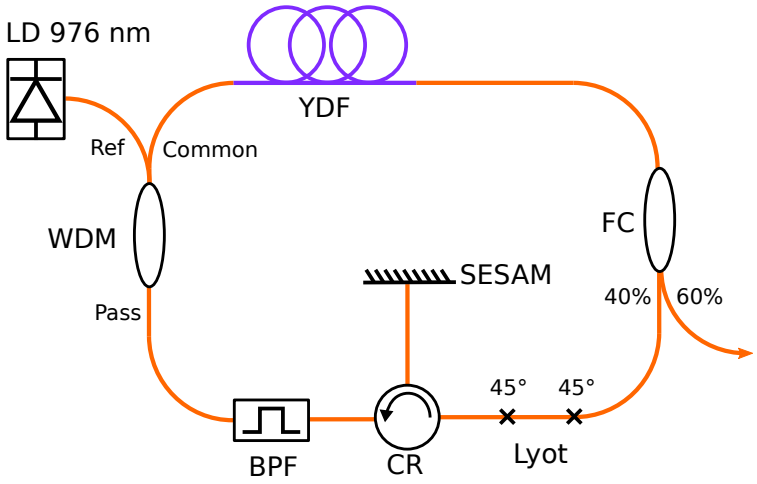

Figure 3.2. *The scheme of the experimentally realized mode-locked fiber seed laser. LD = pump laser diode, WDM = wavelength division multiplexer, YDF = ytterbium-doped fiber, FC = fused output coupler, Lyot = fiber based Lyot filter, BPF = micro-optical band pass filter, CR = optical circulator*

section 4.1.1 contains an overview of the output parameters of the seed pulses, which together should be sufficient to understand how the seed laser works and relates to the rest of the CPA system.

The demonstrated seed laser is a ring resonator made of mostly PM980 passive fiber with the SESAM incorporated by means of an optical circulator. The circulator also enforces a single propagation direction, which is clockwise in fig. 3.2. The laser is pumped by a 300 mW, 976 nm single-mode laser diode through a filter-based micro-optical wavelength division multiplexer (WDM). The gain medium consists of 60 cm of Nufern PM-YSF-HI-HP single-clad ytterbium-doped fiber. The laser's output is located immediately after the active fiber where the pulse energy is at its highest. The output coupling ratio is 60 %. The output coupler is followed by a fiber based Lyot filter, which consists of a 26.5 cm long section of PM980 spliced at 45° angles on both sides. The incoming linearly polarized light gets divided equally between the slow and fast axis polarization states that then accumulate a phase difference due to the fiber's birefringence. The wavelength-dependent phase difference determines whether a certain spectral component ends up in the slow or fast axis after the 26.5 cm fiber section. The following component, the circulator, rejects light in the fast axis, completing the Lyot filter, which has a periodic sinusoidal transmission spectrum. A number of different Lyot filters were fabricated on a trial and error basis until one with 1040-1041 nm central wavelength and approximately 10 nm peak-to-peak distance was realized. Since the Lyot filter has a transmission maximum also at 1030 nm, the laser originally tended to operate at both wavelengths simultaneously. To avoid this, a flat tunable band pass filter was inserted into the cavity after the circulator. The flat filter's pass band was tuned to be approximately 10 nm wide centered at 1040 nm to eliminate the 1030 nm operation. This cavity generated pulses with 5.4 nm spectral FWHM. More detailed experimental data measured for the seed laser is presented in chapter 4.

Originally, the laser was built with only a rectangular filter with 5 nm bandwidth. This, how-

ever, resulted in narrow spectra of roughly 1 nm full-width-at-half-maximum, insufficient to obtain sub picosecond pulses even with perfect compression. The Lyot filter's smoother spectral shape worked much better in this regard. Qualitatively, the difference between the filters is somehow understandable since the 5 nm filter would not clip the edges of the spectrum (and the time domain pulse) unless the input spectrum were broader than the bandwidth, while the smooth Lyot filter always attenuates the edges more than the center of the pulse. However, no numerical modelling was conducted on the seed laser to confirm this effect.

The designed seed laser has two disadvantages concerning its stability. The first is the Lyot filter section, in which light is not linearly polarized and environmental disturbances can affect its polarization state. Therefore, the Lyot filter should be carefully packaged to ensure reliable operation. The second issue is the butt coupled SESAM, which has two distinct problems. For packaging the seed laser, the SESAM has to be fixed so that its fiber coupling does not deteriorate. Additionally, the SESAM its might degrade over time due to interacting with high-energy pulses. These issues were not considered more deeply in the context of this thesis, but they would require further engineering to make the laser viable outside of a lab environment.

3.2 Pulse stretcher and compressor

Selecting the stretcher and the compressor is a major decision in building a CPA system, and these two elements must necessarily be discussed together. In principle, the maximum peak power obtainable from a nonlinearity-limited CPA system is directly proportional to the stretched pulse duration so that a given power amplifier can be made to generate more energetic pulses simply by stretching the pulses more. In practice, physical limitations in the stretcher and compressor discourage extremely large stretching ratios, because the dispersion they can provide is proportional to their physical size and large gratings (whether bulk, FBG or VBG) are both difficult to handle and expensive to fabricate. Therefore, a compromise must be reached between the targeted output peak power, the stretching ratio, and the amplifier's capability to avoid nonlinear effects.

The first decision when selecting a stretcher and a compressor is which of them should have negative and which positive dispersion. Based on the physics of pulse propagation, it does not matter if the seed pulse is stretched with positive dispersion and compressed with negative dispersion or the other way around. In practice, the choice is easy and the stretcher almost always has positive dispersion and the compressor negative dispersion. This is dictated by the fact that the compressor, which interacts with the high-power output beam, should contain as few bulk optical elements as possible and, in typical cases, negative dispersion can be generated with a simpler configuration than positive dispersion. For example, the basic Treacy grating configuration or a prism pair provide negative second order dispersion, while positive dispersion would require a more complex system such as the Martinez grating pair, which would be susceptible to alignment errors and

optical damage when working with the high-power output beam. Furthermore, optical components specified for high-power operation are also more expensive than standard ones, which is another reason to minimize their number. In the designed laser system, the seed pulses are already positively chirped so stretching them with negative dispersion would effectively require a stronger stretcher to first remove the existing chirp and then add enough chirp of opposite sign. All these reasons make deciding the sign of dispersion simple in the end: the stretcher should have positive dispersion and the compressor negative dispersion.

The next and less obvious decision concerns selecting a stretcher and a compressor from the alternatives introduced in section 2.8. The requirement of high-power handling capability restricts the compressor choice significantly so it should be selected first. A fiber Bragg grating cannot survive a high peak power, which would exceed the catastrophic self-focusing limit in fibers. Therefore, a free-space optical solution must be found. A volume Bragg grating is the closest free-space equivalent to a fiber Bragg grating and the best option in terms of compactness and ease of alignment. Unfortunately, unlike FBGs which are tunable, a VBG has a fixed dispersion and center wavelength, which is a major drawback in prototype development when the required dispersion and the exact center wavelength are not exactly known beforehand. The remaining tunable free space compressor solutions include those based on prisms and bulk diffraction gratings. A prism pair would have minimal losses with proper anti-reflection coatings, but it cannot generate large enough dispersion to compress a pulse from hundreds of picoseconds to sub picosecond duration.

This leaves the grating pair in Treacy configuration as the only remaining option. Though gratings are designed for a certain central wavelength, they can typically operate over a relatively wide bandwidth of at least tens of nanometers. To minimize losses and the chance to damage the gratings, fused silica transmission gratings should be used. Fused silica has a high threshold for optical damage and the gratings can reach diffraction efficiencies well in excess of 90 %. The compressor's dispersion can be tuned by changing the distance between the gratings and, slightly, the incidence angle. The amount of angular dispersion a grating can produce depends on its grating period. The more closely spaced the grating grooves are, the more strongly it can disperse the incident light. This translates to a smaller grating separation and an overall more compact setup as long as the grating period is larger than half of the wavelength so that diffraction takes place. Aiming for a compact compressor, a pair of commercial gratings with 575 nm grating period was chosen for the work in this thesis. The small grating period has, however, a disadvantage in increasing the compressor's third order dispersion even more than second order dispersion according to eq. (2.52), and compensating for that additional TOD must take place earlier in the CPA system.

As for the stretcher, an in-fiber solution is highly preferable over free-space solutions to limit alignment issues in the otherwise fiber-based seed and amplifier chain. This leaves two options: a long spool of fiber and a fiber Bragg grating. Ordinary single-mode fiber,

such as PM980, has positive dispersion at 1 µm wavelength so a sufficient length of it can be used to stretch an optical pulse that can then be compressed with the grating pair's negative dispersion. Tuning the fiber stretcher's dispersion would be straightforward by increasing or decreasing the fiber length, but this tuning is only possible when developing the laser system, not while it is running. The fiber spool stretcher also has a severe disadvantage: both it and the grating compressor have positive third order dispersion, which when added together will limit the compression efficiency. There are specially designed fibers with negative third order dispersion [66] but they are expensive and not widespread and hence were dropped from consideration.

For this prototype system, a custom chirped fiber Bragg grating was chosen because of its compactness, tunability and ability to compensate for the compressor's third order dispersion. The CFBG has a second order dispersion of 67.1 ps. Reaching an equally high dispersion with PM980 fiber would require an unpractically long fiber spool (almost 3 km), which could have led to problems with SRS as well. Reaching an equivalent negative dispersion with the selected grating pair compressor requires a grating separation of 43 cm assuming Littrow incidence angle. The FBG stretcher also provides negative third order dispersion, which can negate pre-compensate for the positive third order dispersion in the compressor. Both dispersion components in the stretcher are also electronically tunable within a small range, which will greatly simplify optimizing the compression efficiency in the real-world setup.

While the compressor is self-evidently the final element of the CPA system, there is in principle some freedom in the placement of the stretcher. If the seed laser generated a very low pulse energy, it might make sense to amplify the pulses before the lossy stretcher. In this case, the designed ANDi seed laser generates energetic pulses, which would start accumulating nonlinear phase shift during a propagation in a long fiber so it makes sense to place the CFBG stretcher immediately after the seed and before the first preamplifier to avoid the nonlinearity.

3.3 Preamplifier 1

After the stretcher, the design includes a single-mode fiber amplifier to overcompensate for the stretcher's losses. The preamplifier is a simple one with a 976 nm pump diode, a wavelength division multiplexer, a piece of highly Yb-doped active fiber and an isolator, and as such does not warrant special discussion. The scheme is shown later together with the modelling parameters in fig. 4.7.

The fiber lengths in the first preamplifier are too short to provide significant dispersion, and the peak power is too low to cause any nonlinear effects. This preamplifier is actually the least meaningful element in the CPA system but was included to provide flexibility against unpredictable seed power and possibly lossy components. With limited seed power, the two-stage preamplification helps to limit ASE generation in the preamplifiers, which must be kept low because CW ASE light entering the final power amplifier would

rob gain from the pulsed signal. As long as ASE is not too strong, the CPA system could be simplified by using a single preamplifier, the second one.

3.4 Pulse picker

The next element in the CPA system is the pulse picker, which is a fast optical switch that can selectively block most pulses but transmit every nth pulse to reduce the repetition rate. The required switching speed depends on the pulse repetition rate at the input of the pulse picker, which must be able to switch within the time interval between two consecutive pulses. With mode-locked fiber lasers typically generating pulse trains at tens of MHz repetition frequencies, the pulse picker must be able to switch from off to on state roughly within 10 ns in continuous operation. The standard technology used in pulse pickers is the acousto-optic modulator (AOM), in which the presence of an RF acoustic wave in crystalline material in the on state is used deflect a propagating beam to the output while, in the off state, the undeflected beam is absorbed inside. This working principle is illustrated in fig. 3.3.

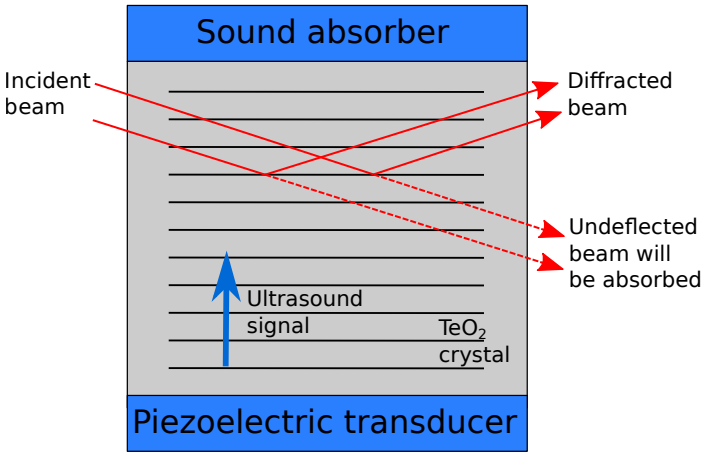

Figure 3.3. *The working principle of an acousto-optic modulator: An RF acoustic wave travelling in a crystal such as TeO_2 causes a slight index grating in the material, which then diffracts a propagating beam to a slightly different direction. The rise and fall time of the AOM depends on how tightly the beam is focused and on the speed of the acoustic waves in the crystal.*

Electro-optic amplitude modulators can reach similarly fast switching times, but the required kV-class voltages and lower duty cycles make them unappealing. Therefore, the choice to use an AOM is clear. A fiber-coupled AOM was selected for the CPA system to avoid free space alignment issues.

3.5 Preamplifier 2

After the lossy pulse picker, a second preamplifier is required to boost the pulse train's average power to the order of 10 mW for amplification in the tapered power amplifier. Because of the low power requirement, a relatively standard core-pumped single-mode fiber

amplifier can be used for the purpose instead of a double-clad fiber amplifier. As such, the preamplifier design is rather uninteresting and does not warrant a lengthy discussion. The scheme of the second preamplifier is shown in the next chapter in fig. 4.15 together with the numerical simulations.

At 1 MHz repetition rate, the targeted pulse energy of >10 nJ still becomes quite high for single-mode fiber so the preamplifier must be designed to avoid nonlinear phase shift. This is taken into account by using fibers that are still single-mode but have larger cores of roughly 10 µm in diameter and lower numerical apertures than in the first preamplifier. Additionally, backward pumping direction is chosen so that amplification mostly takes place near the output end of the active fiber.

The output of the second preamplifier contains a couple of components different from the first preamplifier. First, a band pass filter is added to block amplified spontaneous emission that might seed stimulated Raman scattering in the tapered amplifier and, second, a high-power version of the isolator is selected to protect the preamplifier from feedback from the taper.

3.6 Tapered fiber power amplifier

Tapered optical fibers occupy a small niche in the field of fiber optics, being specialized for high-peak power and narrow-linewidth applications where nonlinear effects are the limiting factor. Tapered fibers in general have a longitudinally varying diameter but there is an important distinction to be made between tapered fibers realized by heating and stretching an existing fiber and those fabricated by changing the drawing speed when the fiber is drawn from the preform. The fibers in the first category are thinner than the commercial uniform fibers from which they were made while the fibers in the second category are typically thicker than uniform fibers at one end. The tapered fiber in this thesis naturally belongs to the latter category. More specifically, the tapered fiber constitutes the laser active medium in the final power amplifier and, for this purpose, it is doped with ytterbium and contains a pump cladding as well as stress rods for PM operation.

Even though no alternative fiber types were considered for the CPA system, it is worth detailing the strengths and weaknesses of tapered double-clad fibers compared to competing solutions for this kind of application. Tapered fibers' most important advantage is simplicity. A tapered fiber has a narrow end designed to be compatible with standard single-mode fibers and can therefore be readily spliced to a signal input fiber. In contrast, a uniform LMA fiber amplifier requires a special mode-field adapter or free-space optics to efficiently couple single-mode light into the fiber core. In tapered fibers, only the output end has a large core size but that is exactly the part of the fiber where peak power is high so the fiber design can still efficiently reduce peak intensity and nonlinear effects. The gradual increase in the diameter of a tapered fiber can preserve the single-transverse-mode operation during propagation and allow near-diffraction-limited output beam from the effectively multi-mode core at the wide end of the taper. The thick output end of a

taper also allows powerful multi-mode pump radiation to be coupled in.

A more subtle benefit of the gradually increasing core size is that the saturation power, which determines the signal power required to effectively extract the stored energy via stimulated emission, also grows from the narrow end to the thick end. For this reason, the input power to a tapered amplifier can be of the order of 1-10 mW and the amplifier can still reach an output power of 10-100 W with a gain of 30-40 dB or higher. A comparable uniform fiber amplifier would require at least on order of magnitude higher input power to extract the same energy from the fiber. In a tapered fiber amplifier, the signal is amplified to this level internally in the narrow input end. In short, a tapered fiber amplifier can at best replace two traditional fiber amplifiers in a fiber laser system.

Where tapered double-clad fibers lag behind the competing technologies is in the fiber's absolute mode field area and consequently the maximum peak power handling capability. Especially photonic crystal fibers can provide very large mode field areas, for example 8600 μm^2 reported in [19], which is an order of magnitude higher than that of a typical tapered fiber. Obtaining world record peak powers is therefore unrealistic with tapered fiber amplifiers. However, the above-mentioned benefits in handling and system integration make them attractive options in many applications where their performance is adequate.

The most complex part of a practical tapered fiber amplifier is the pump coupling. Though the fiber could in principle be pumped from either end, only backward pumping makes sense since strong amplification in the narrow end would greatly enhance nonlinear effects. Therefore, pump light from a multi-mode laser diode's output fiber is coupled into the taper in free space as shown in fig. 3.4. Using free space pumping instead of a pump combiner means that the amplified pulses do not propagate and accumulate nonlinear phase in a passive output fiber. Realistically speaking, commercial combiners do not even exist for the 40-50 µm output core diameter.

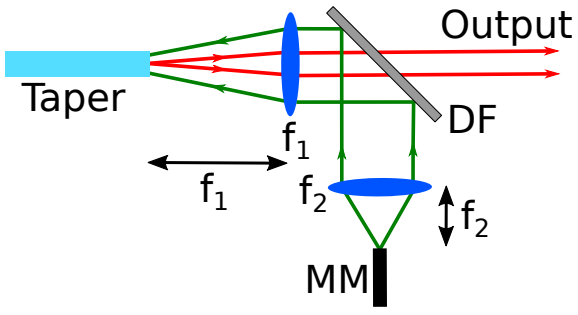

Figure 3.4. *The scheme of the free space optics for collimating the signal beam and coupling the multimode pump beam into the tapered fiber's cladding. DF = dichroic filter, MM = multimode pump fiber*

The pump coupling setup includes collimation lenses for both pump and signal light. A dichroic filter separates the output signal beam from the input pump beam, while the signal collimation lens also focuses the pump light onto the taper's end face. To avoid beam quality degradation, aspheric lenses must be used, and it is beneficial to choose a rather long focal length of $>$10 mm for the signal lens to make the generated beam larger

and less divergent.

Other design concerns include the tapered fiber's core-to-cladding ratio and longitudinal thickness profile, but in this regard tapered double-clad fibers do not differ greatly from normal LMA double-clad fibers, and the same principles hold for both. Using a smaller cladding restricts the amount of pump power that can be coupled into the fiber but at the same time improves pump absorption in the core, allowing for a shorter fiber length and lower nonlinearity. Strong pump absorption is especially important for short wavelength 1030 nm operation, which requires relatively high excitation to obtain positive gain. In contrast, long-wavelength operation might suffer from excessive 1030 nm ASE if excitation is too high. In terms of the longitudinal profile, a large core is always better in avoiding nonlinearity so the diameter of the taper should rise relatively rapidly from the input single-mode fiber thickness towards tens of nanometers. The rise must not be too fast, however, or the output beam quality will suffer from coupling to high-order modes within the transition region.

3.7 Electronics and mechanics

This thesis concentrates on the physics and fiber optics side of the CPA system, but it is worth noting that some additional mechanical and electrical engineering is necessary for realizing such a laser system in practice. All the laser diodes need drivers, which are optimally computer controllable. The AOM pulse picker requires additional electronics that use a monitor photodiode to synchronize with the incoming pulse train and generate the correct driving signal. Other monitor diodes and possibly thermocouples should act as failsafe to shut down the laser system in case of abnormal operation. The power amplifier, including the tapered fiber, the multimode pump diodes, and the pump coupling optics must be actively cooled to maintain constant temperature and output power and to avoid damage due to overheating. All these things require real engineering work that is not considered here in any detail.

4 EVALUATION OF THE DESIGN BY NUMERICAL SIMULATIONS

This chapter presents numerical simulations of the complete designed CPA laser system starting from the pulses generated by the seed laser and ending with the compressed pulses after the gratings. In effect, the seed pulse is propagated computationally through each piece of fiber and each component in the system. Gain in the active fibers is modelled using rate equation simulations while the actual ultrashort pulse propagation is calculated with the generalized nonlinear Schrödinger equation. Since the components for this laser system design actually exist, the simulations strive to use their realistic parameters from their datasheets where possible. Some starting parameters were unfortunately unavailable and have been substituted by educated guesses or estimates. The text states clearly the points where this has been necessary. Similarly, some physical effects or details are beyond the scope of this thesis either because of the difficulty in implementing them or, more commonly, because of their impact on the modelling results was considered very limited. The text also includes a mention wherever the physical model could be improved by considering those additional effects.

The first half of this chapter goes through the laser design piece by piece in sequential order to show how each part is modelled and how it affects the pulse propagating through it. For this purpose, the simulation uses the seed pulse from the experimentally build mode-locked fiber laser, which allows evaluating the seed laser's suitability for the CPA system at the same time. After the component-by-component analysis, the model for the complete system is used to study the effect of tuning the amplifiers' pump currents and the stretcher's dispersion as well as using a Gaussian seed pulse.

The ultrafast pulse is described numerically as an array of complex numbers corresponding to the discretized complex amplitude in either the spectral or time domain. As mentioned in section 2.5.3, the two descriptions are equivalent, and it is possible to switch between them by Fourier transforming. This also has a practical consequence as it means that the scales of the simulation arrays in time and spectral domain are similarly linked. The table below table 4.1 shows the parameters of the simulation arrays used in all the ultrafast simulations in this chapter. The spectral domain is presented as using wavelength units for convenience, though in reality the simulation array consists of equally spaced points in frequency and the wavelength resolution varies slightly from the low to high-frequency side of the array.

Table 4.1. *The time and wavelength ranges and resolutions used in the discretized GNLSE simulation arrays.*

Parameters of the pulse simulation array	
Time resolution	72 fs
Time range	1.2 ns
Wavelength resolution	3.1 pm
Wavelength range	50 nm
Center wavelength	1040 nm
Number of points	16384

The parameters are determined by the requirement to model both stretched and compressed pulses in the CPA system. First, the time window must be long enough to accommodate a pulse hundreds of picoseconds long so that no energy can escape from the window to the sides, whereupon it would appear on the other side, distorting the simulation results. At the same time, the time grid must be dense enough to describe a compressed sub-picosecond pulse. In this case, a $<$100 fs resolution is acceptable given that the seed's spectral width (see section 4.1.1) is too narrow to support $<$0.5 ps pulses. The number of data points is typically set as a power of two to leverage the most efficient fast Fourier transform (FFT) algorithms. Consequently, the best choice is 2^{14} points, which leads to a time resolution of 72 fs. The spectral range and resolution follow from the time domain parameters as expected with the Fourier transform. Notably, the spectral range excludes wavelengths around 1090 nm where stimulated Raman scattering would appear. This is a conscious decision to reduce the computational load and based on the following reasons. The simulations presented in this chapter suggest that poor pulse compression due to self-phase modulation becomes the limiting factor of the CPA system earlier than significant SRS is expected to be generated based on experiments. The second reason to exclude Raman wavelengths is that modelling SRS accurately in a fiber amplifier is simply difficult as it also requires accurate modelling of background noise caused by amplified spontaneous emission and spontaneous Raman scattering, because these provide the seed signal for SRS.

4.1 Pulse propagation through the CPA system

This section describes the CPA system is modelled numerically to propagate a seed pulse from the experimental laser through the system, and how each component modifies the pulse between its input and output.

4.1.1 Seed laser

The seed laser is an experimentally realized mode-locked PM all-normal-dispersion fiber laser generating an average output power of 30.6 mW at the repetition rate of 35.8 MHz. This translates to a pulse energy of 0.85 nJ. The measured spectrum of the seed pulse is shown on the right in fig. 4.1. There is a minor caveat: the spectrum has been shifted slightly from the original center wavelength of 1040.7 nm to be centered at exactly 1040 nm, which is the stretcher's wavelength and a nicer center wavelength for the figures. Since the seed laser's wavelength is determined by the tunable spectral filters in the cavity, it could even in reality be tuned to 1040 nm even though the measured spectrum happens to be for 1040.7 nm. The spectrum is 5.4 nm wide (FWHM) and has sharp edges typical for ANDi lasers. On the top, the spectral shape is irregular possibly because of some polarization filtering effect in the cavity. In addition to the spectrum and output power, the seed's autocorrelation was measured and is shown in fig. 4.2.

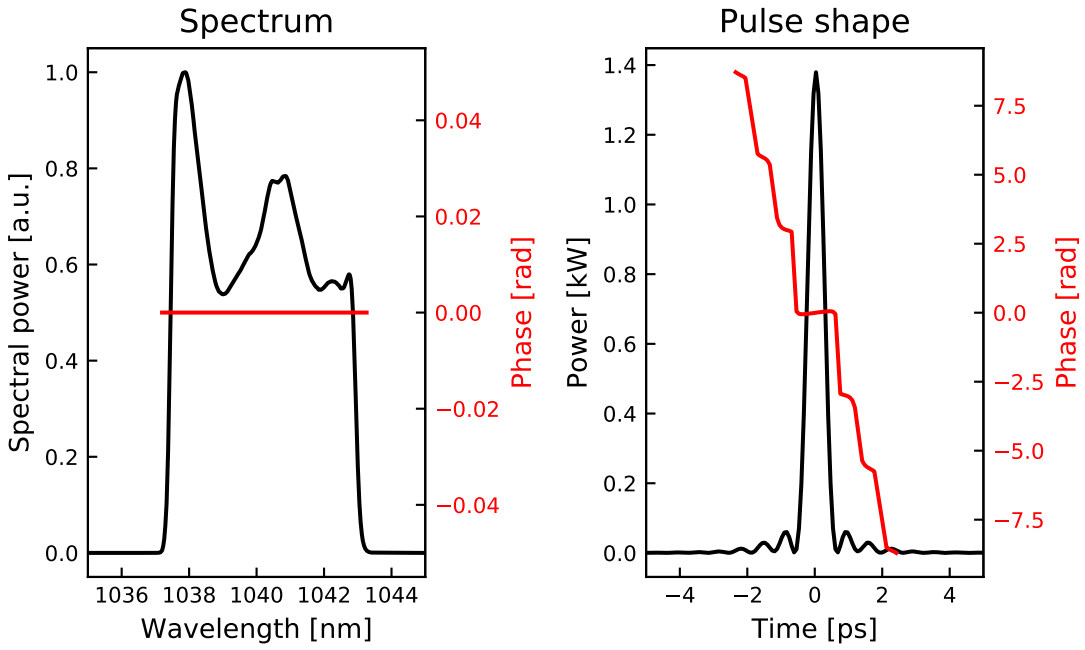

Figure 4.1. *The pulse used as a starting point of the numerical simulations. Left: The spectrum of the seed pulse. Right: The pulse shape calculated by Fourier transforming the spectrum assuming constant spectral phase. Starting dispersion has not yet been applied to the pulse. The phase has only been drawn where the power is greater than 0.5 % of the maximum since phase fluctuates greatly and has no meaning when the power is close to zero.*

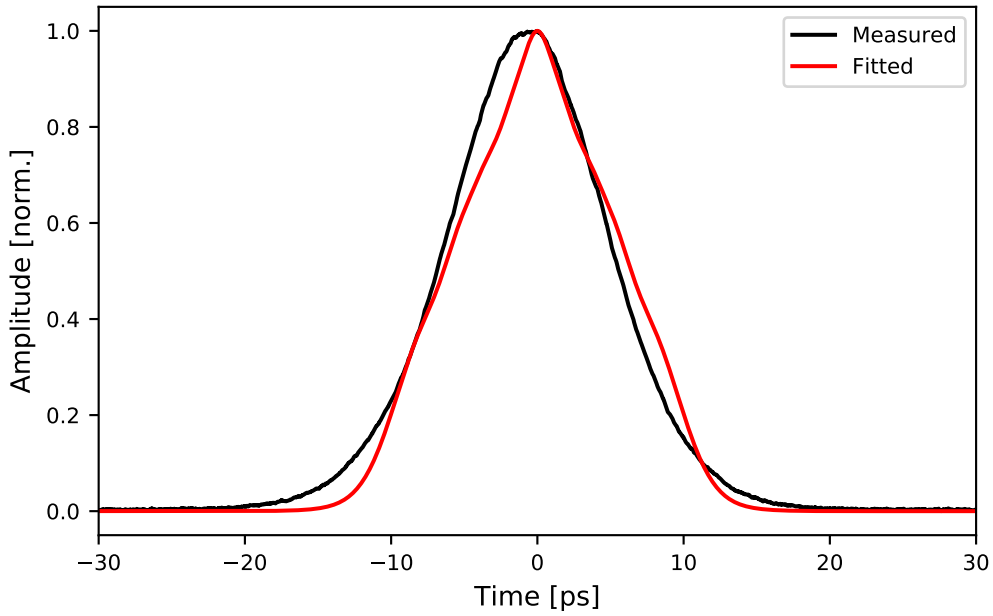

Figure 4.2. *The measured seed autocorrelation and the best simulated fit based on adding second and third order dispersion to the pulse shape in fig. 4.1. The optimal second and third order dispersion values are* $\varphi_2 = 1.31\,ps^2$ *and* $\varphi_3 = -0.0162\,ps^3$.

The complete numerical description of the pulse requires the knowledge of the pulse's complex electric field envelope. However, that information cannot be obtained solely from spectrum and autocorrelation measurements. In the absence of a possibility to completely characterize the seed pulse, for example with the frequency-resolved optical gating technique [67], this is the first point where estimation is required. The pulse is not transform-limited like the one shown on the right in fig. 4.1 since the experimentally measured autocorrelation width is 12.4 ps. Instead, the pulse is expected to be positively chirped coming from an all-normal-dispersion fiber laser.

A rough way to estimate the chirp of the seed pulse based on the inadequate experimental data is to take the spectrum as the starting point and apply dispersion until the autocorrelation calculated from the spectrum best matches the measured autocorrelation. To limit the complexity of this procedure, the simulation only adds second and third order dispersion to the pulse. Numerical optimization with this restriction leads to the autocorrelation shown in fig. 4.2 together with the original measured autocorrelation.

The two autocorrelations have similar widths but overall, the fit quality is not particularly good with the computed result being much more triangular than the measured one. We must conclude that the seed pulse must have a more complex spectral phase that is impossible to estimate accurately. This does not matter greatly since the pulse shape in the amplifiers will mostly be determined by the spectral shape and the stretcher's massive dispersion.

The actual pulse corresponding to the optimized autocorrelation is shown in fig. 4.3. Its temporal profile is irregular mirroring the uneven spectral shape. The negative effect

of the spectral shape will become evident later when assessing the performance of the complete CPA system.

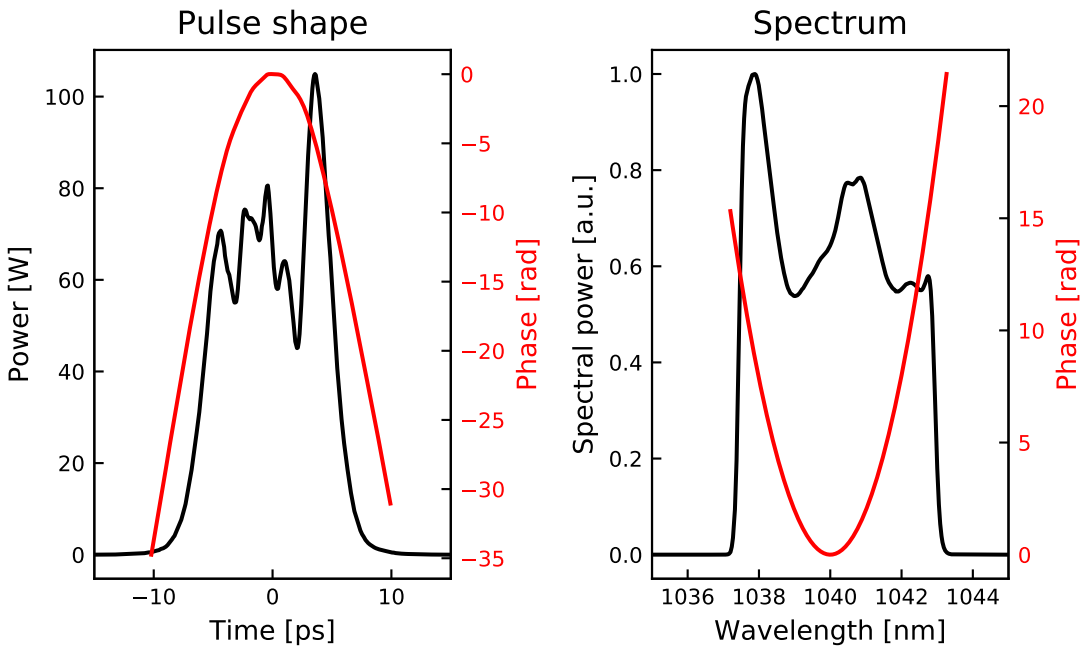

Figure 4.3. *The seed pulse from fig. 4.1 after applying the second and third order dispersion obtained from fitting the autocorrelation. The resulting pulse is modestly positively chirped.*

The energy of the pulse has been scaled to match the experimentally measured pulse energy, leading to a peak power of roughly 100 W. Other parameters of the chirped seed pulse are briefly summarized in table 4.2.

Table 4.2. *Parameters of the chirped seed pulse shown in fig. 4.3.*

Energy	0.85 nJ
Peak power	105 W
Time duration (FWHM)	10.6 ps
Spectral width (FWHM)	5.4 nm
Time-bandwidth product	15.8

This pulse is used to seed the following amplifier chain. All the components will transform the pulse somehow and the modified pulse shape and spectrum will be shown after each functional part of the laser system (i.e. after the stretcher, pulse picker, each amplifier and finally, after the compressor) but not after each piece of fiber or single component since most of them do not modify the pulse noticeably.

4.1.2 Stretcher

After the seed laser, the pulse is stretched in a tunable chirped FBG to reduce its peak power and to prevent it from accumulating nonlinear phase shift in the amplifier stages. The FBG has a nonlinear chirp to better compensate for the third order dispersion in the fibers and the final grating compressor. Since the FBG is a reflective component, a circulator is required to incorporate it in the laser system. The whole stretcher is shown schematically in fig. 4.4. Each port of the circulator as well as the FBG is assumed to have a 25 cm long passive PM980 fiber pigtail. Keeping the passive fibers as short as possible is beneficial in pulsed amplification to avoid nonlinearity and additional dispersion. At the same time, the fibers must be long enough for practical purposes to be spliced a couple of times if the first splices fail for some reason. The 25 cm pigtail length is a compromise reflecting this requirement and will be used for all other components in the system as well.

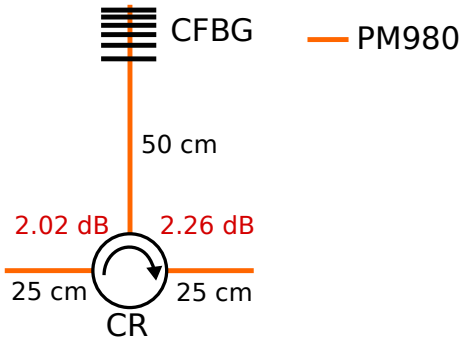

Figure 4.4. *A schematic of the stretcher assembly with the passive fiber lengths and the circulator's losses indicated. CR = optical circulator, CFBG = chirped fiber Bragg grating*

The stretcher starts therefore with pulse propagation through a 25 cm section of passive fiber, which is simulated using the GNLSE model. The parameters used for PM980 fiber in the stretcher and the subsequent parts of the CPA system are shown in table 4.3.

Table 4.3. *Parameters used to model PM980 passive fiber at 1040 nm*

Core diameter	6.0 µm
Core NA	0.12
Second order dispersion β_2	$2.3 \cdot 10^{-26}$ s^2
Third order dispersion β_3	$4.4 \cdot 10^{-44}$ s^3
Nonlinear effective area A_{eff}	38 µm^2
Nonlinear coefficient γ	$4.0 \cdot 10^{-3}$ W^{-1} m

The core diameter and NA are based on the fiber's specification [68], the second and third order dispersion values are taken from [69], the effective area is calculated from the fundamental Bessel mode shape assuming a step-index geometry with the listed core radius and NA, and finally the nonlinear coefficient γ is calculated based on the effective area and the nonlinear index, which is assumed to be $2.5 \cdot 10^{-20}$ m^2 W^{-1} based on the values

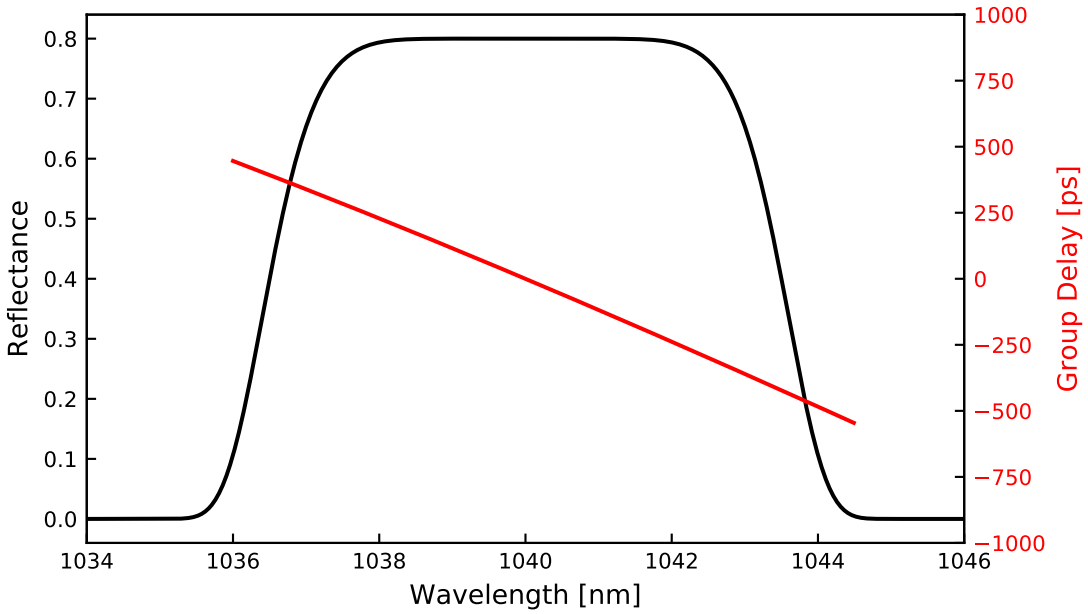

Figure 4.5. *The reflection spectrum and group delay of the tunable chirped fiber Bragg grating stretcher.*

given in [23]. All parameter values are for 1040 nm and assumed to be constant over the simulated wavelength range. This is a valid assumption since the pulse's spectrum is only roughly 5 nm wide. The fiber's background loss as well as splice losses between similar single-mode fibers are neglected as insignificant both here and in the rest of this chapter.

Next, the pulse enters the first port of the circulator, which is modelled as a lumped loss of 2.02 dB between ports 1 & 2 and 2.26 dB loss between ports 2 & 3. The loss values are based on the actual datasheet for the circulator. The circulator's non-reciprocity also isolates the seed laser from back reflections further down the fiber. The isolation is assumed to be adequate and any backward propagating signals are not considered in this model.

After the first pass through the circulator, the pulse propagates a further 50 cm in PM980 fiber (consisting of the both the circulator's and the chirped fiber Bragg grating's pigtails) until it reaches the CFBG, which is the component that performs the stretching. The CFBG is also considered as a lumped component with two functions, spectral filtering (including loss) and dispersion. Both of these can be applied as transfer functions in the spectral domain so their order of application does not matter. The filter shape is modelled after the datasheet as a super-Gaussian function with a peak reflectance of 0.8 and full-width-at-half-maximum of 7 nm. The fiber Bragg grating's dispersion consists of the following static components: $\beta_2 = 67.1\,\mathrm{ps}^2$, $\beta_3 = -0.856\,\mathrm{ps}^3$ and $\beta_4 = -0.039\,\mathrm{ps}^4$. Additionally, the second and third order dispersion can be tuned by $\Delta\beta_2 = \pm 3.51\,\mathrm{ps}^2$, and $\Delta\beta_3 = \pm 0.915\,\mathrm{ps}^3$. The stretcher's response, i.e. filter profile and group delay at zero tuning, is shown in fig. 4.5.

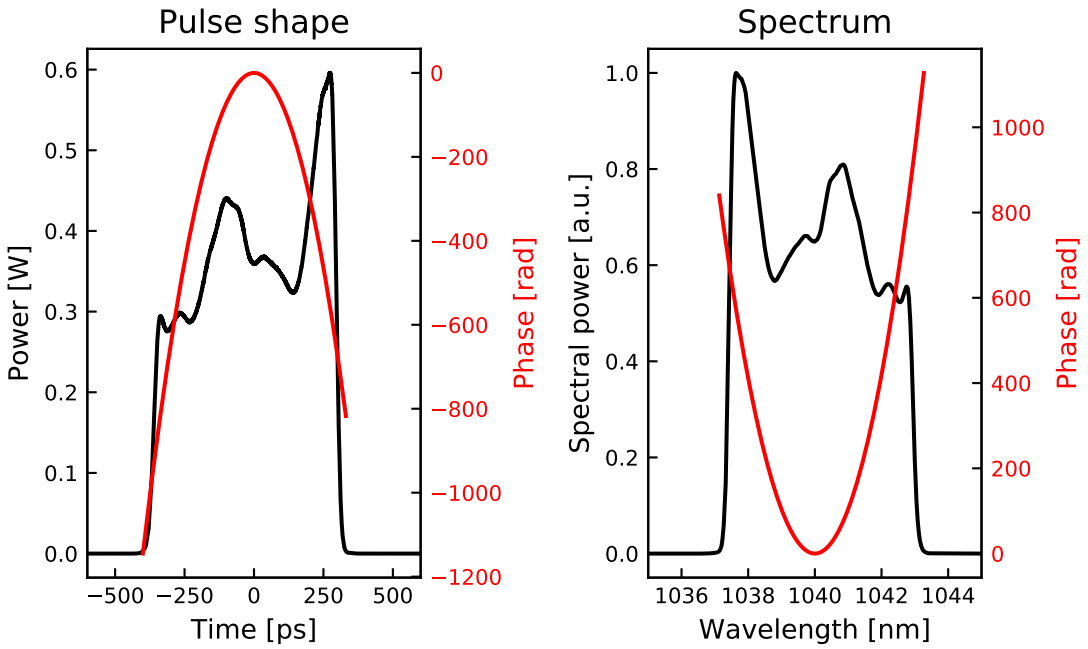

Figure 4.6. *Pulse shape and spectrum after propagating through the stretcher.*

Table 4.4. *Parameters of the pulse after the stretcher.*

Energy:	0.25 nJ
Peak power:	0.60 W
Time duration (FWHM):	568 ps
Spectral width (FWHM):	5.4 nm
Time-bandwidth product:	854

After the CFBG, the now stretched pulse propagates through the same 50 cm of PM980 back to the circulator's second port, through the circulator (incurring lumped loss) and the 25 cm of the third port's passive fiber. The pulse at this point is shown in fig. 4.6 and its main parameters are listed in table 4.4.

The pulse energy has dropped to 0.25 nJ due to losses in the circulator and the CFBG. The pulse is now also massively positively chirped with a duration of almost 600 ps, which has reduced its peak power to below 1 W. The strong positive dispersion has effectively mapped the pulse's spectral shape into time domain. For example, the narrow peak at roughly 1038 nm in the spectrum has resulted in a similarly sharp peak at the trailing edge of the pulse. If the stretcher had negative dispersion, this peak would naturally be located at the leading edge. The spectral shape has not been affected since the FBG's reflection band was broader than the spectral width. Had the pulse's spectrum been too broad for the CFBG, part of it would have been clipped out.

4.1.3 Preamplifier 1

The stretched pulse then enters the first preamplifier whose purpose is to boost the average power of the pulse train by an order of magnitude before the repetition rate is reduced in the pulse picker. The preamplifier's design is based on 6/125 µm Nufern PM-YSF-HI-HP active fiber forward-pumped with a single-mode 200 mW, 976 nm pump diode. The schematic with fiber lengths and component losses is shown in fig. 4.7.

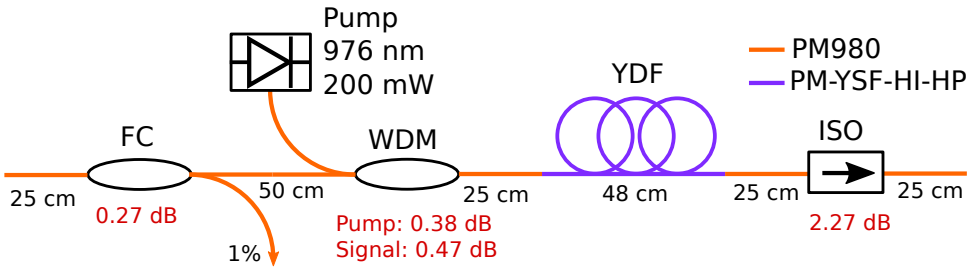

Figure 4.7. *The scheme of the first preamplifier using 6 µm core-pumped active fiber. The fiber lengths and losses are indicated in the figure. FC = fused coupler (1/99), WDM = wavelength division multiplexer, YDF = ytterbium-doped fiber, ISO = isolator*

The first component is a 1 % fused coupler used to monitor input power, i.e. that the seed and the stretcher are working properly. The second component is a filter-based micro-optical wavelength division multiplexer, which couples pump light into the signal fiber. The WDM is followed by a length of the Yb^{3+}-doped active fiber, and the final component in preamplifier 1 is an isolator, which protects the amplifier from backward propagating power.

The active fiber's parameters used in the modelling are shown in table 4.5

Table 4.5. *Parameters used to model PM-YSF-HI-HP active fiber at 1040 nm*

Core diameter	6.0 µm
Core NA	0.11
Yb^{3+} doping concentration	$3.72 \cdot 10^{25}$ 1/m^3
Cross sections	see fig. 2.2
Nonlinear effective area A_{eff}	42 µm^2
Nonlinear coefficient γ	$3.5 \cdot 10^{-3}$ W^{-1} m^{-1}

where the core radius and NA are from the manufacturer's website [28] who also kindly provided the doping concentration by email. The core material's absorption and emission cross sections were also available online and a spline interpolation fit to them was shown in fig. 2.2. The dispersion values of the PM-YSF-HI-HP are assumed to be the same as for PM980 in the absence of data. The nonlinear coefficient computed at 1040 nm is slightly lower due to the lower NA and expanded mode area compared to PM980.

Before the ultrafast pulse can be numerically propagated through the amplifier, the active fiber's optimal length and excitation must be solved using rate equation simulations. Since

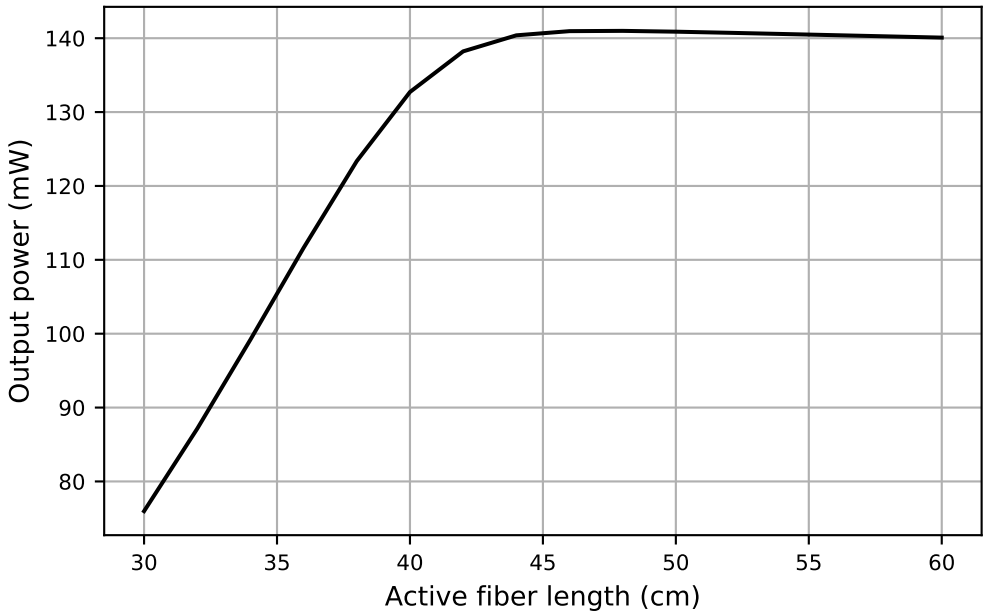

Figure 4.8. *Output power of the first preamplifier as a function of active fiber length obtained from the rate equation simulations while keeping the signal and pump powers constant. The optimum fiber length is 48 cm.*

the signal's repetition rate at 35.8 MHz is much higher than the inverse of the excited state lifetime in Yb^{3+}:silica (about 1 ms), the pulse train can be approximated as a CW signal and simulated with the steady state rate equation model, which simplifies matters.

In this case, the steady state model comprised a total of 162 optical channels, including one channel for the 1040 nm signal, one channel for the 976 nm forward pump beam and 80 channels for both forward and backward propagating ASE light between 1000-1080 nm. For improved accuracy, the pulse's spectrum could be divided into multiple channels at slightly different wavelengths instead of using only a single channel but the potential benefit was judged to be minor because gain does not vary that much within 5 nm that this was not implemented. The rate equation approach also requires that the spectral shape does not noticeably change during amplification due to nonlinear effects, which is valid for the stretched pulse but pulses with higher peak power would require a more complex approach. The steady state rate equation model first calculated the Bessel mode shape of each channel (i.e. at each wavelength) and then based on that computed the overlap integral and the gain and absorption coefficients in eq. (2.9). These were then used to solve eq. (2.10) and eq. (2.12) to give the optical powers and ion excitation at each point in the fiber. The input average power going into the active fiber was 7.6 mW after the minor losses in the coupler and the WDM. Similarly, the WDM's loss caused the pump power going to the active fiber to be 183 mW instead of 200 mW. Multiple simulations were run at different fiber lengths while keeping the signal and pump powers constant to find the optimum active fiber length. The result is plotted in fig. 4.8.

The optimal fiber length giving the highest output power is 48 cm. At lengths shorter

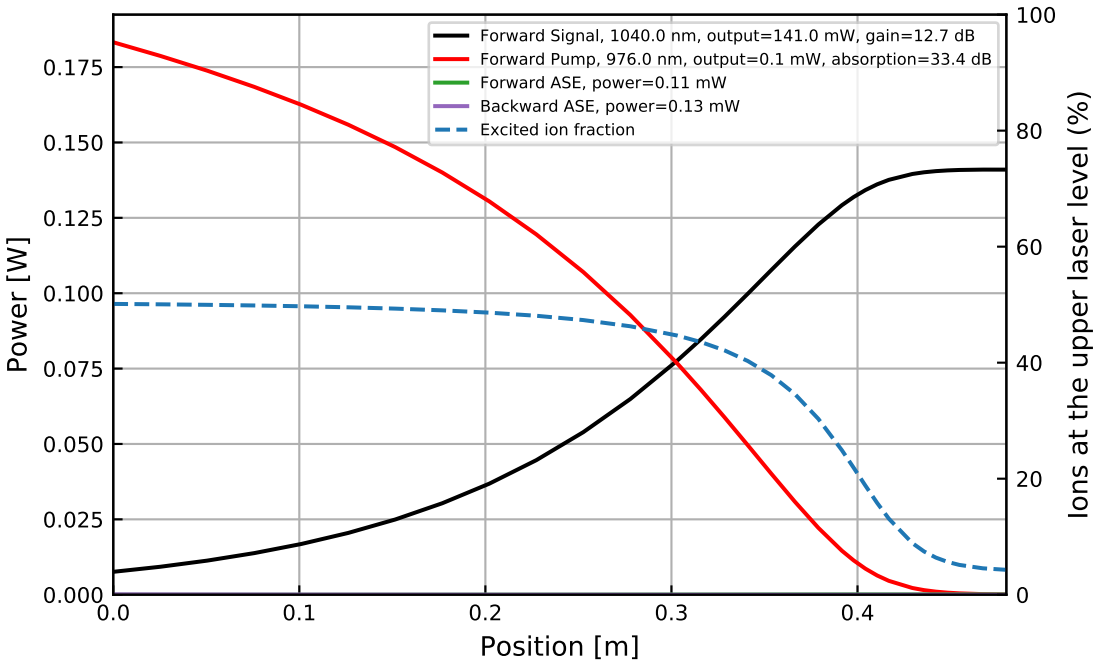

Figure 4.9. *Optical powers and Yb^{3+} ion excitation in the first preamplifier at optimal fiber length for 7.6 mW, 1040 nm signal and 200 mW, 976 nm pumping. ASE is too weak to be visible.*

than that, pump light has not been completely absorbed so using a shorter fiber would effectively mean a drastically lower available output power. At longer lengths, there is no pump light left so the 1040 nm signal starts to be reabsorbed. However, the relatively strong $>$100 mW signal can easily saturate the rather weak absorption and, for that reason, reabsorption causes only a modest downward slope in output power.

The optimum fiber length applies only for the constant pump and signal powers used in the calculations. While the maximum pump power is indeed fixed, and the fiber should be able to absorb it completely, the signal power could vary more easily. If the signal were stronger, a shorter length of fiber would be enough to transfer pump power to signal power, and the signal would experience some reabsorption loss in the rest of the fiber, which would not be too harmful due to the saturation of reabsorption. However, if the input signal were weaker, a longer fiber would be required, so a part of the pump light would pass through unabsorbed when using the fiber length optimized for a stronger signal. As missing gain due to unabsorbed pump is much worse than weak reabsorption, the active fiber length should generally be optimized for the weakest anticipated input signal for best operation at different input powers. In this thesis, only the single input signal strength is considered for simplicity, but the design of a real-world fiber laser system would require more care in this regard. The results of the optimum simulation for the used input signal are shown in greater detail in fig. 4.9.

The figure shows that all the pump is indeed absorbed until the fiber end and that signal reaches its maximum power there. ASE is unsurprisingly weak given the modest 12.7 dB gain in the amplifier and will not be considered in the ultrafast simulation. The most

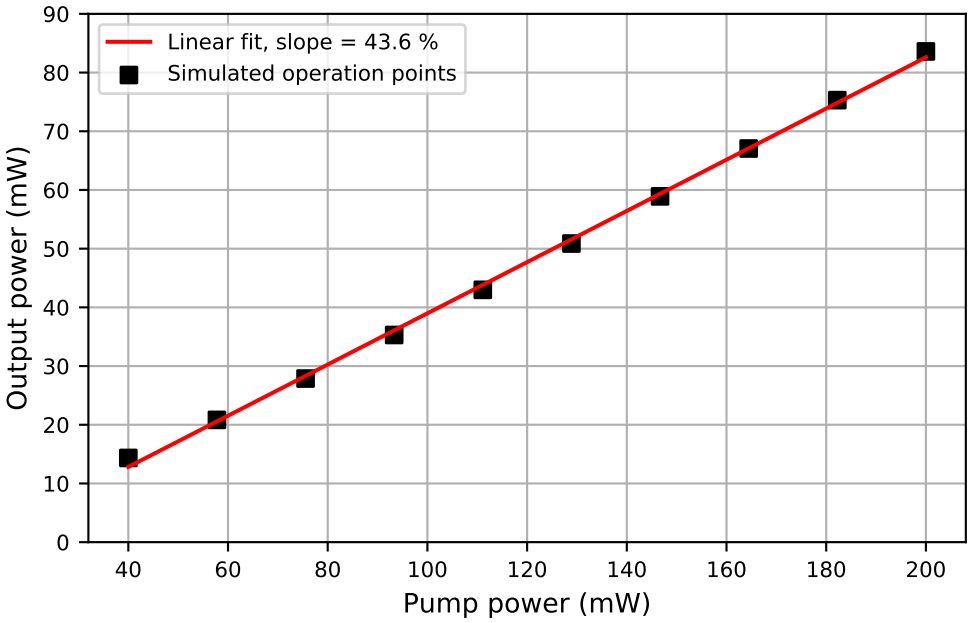

Figure 4.10. *The simulated slope efficiency of the first preamplifier at 48 cm fiber length is 43.6 %.*

useful result of this simulation is the ion excitation marked with the blue dashed line since it can be used to calculate gain and absorption at any wavelength. Naturally, though, the excitation would no longer be valid if the signals propagating in the fiber would change considerably.

Knowing the optimal fiber length, the pump power can now be tuned to find the slope efficiency of the amplifier. To be realistic, this calculation must take into account all the losses in the amplifier's various components, not just what happens inside the active fiber where the low quantum defect leads to an excellent conversion efficiency. The results of the slope efficiency simulations are shown in fig. 4.10. The maximum output power from the amplifier is 83.6 mW after the losses in the isolator, compared to the 141 mW directly after the active fiber in fig. 4.9. This brings the slope efficiency down to an experimentally more realistic value of 43.6 %.

To move towards the ultrafast simulation, the excitation from the maximum pump power (200 mW) and optimal fiber length (48 cm) result was used to calculate the net gain in the active fiber at each of the 2^{14} wavelengths in the propagating pulse's simulation window and at each point in the fiber. To avoid calculating the Bessel mode shape 2^{14} times for as many different wavelengths, the overlap integral Γ was set constant at its 1040 nm value of 0.739. A slightly more accurate method would be to calculate the overlap integral for perhaps 100 wavelengths and then interpolate the results to cover the densely spaced 2^{14} wavelengths. The result of the net gain calculation is shown in fig. 4.11.

Longitudinally, gain is clearly highest at the start of the fiber, consistent with forward pumping. Since this is the optimum fiber length for 1040 nm signal, gain at 1040 nm is exactly zero at the output end of the fiber where the light red and blue regions meet. A

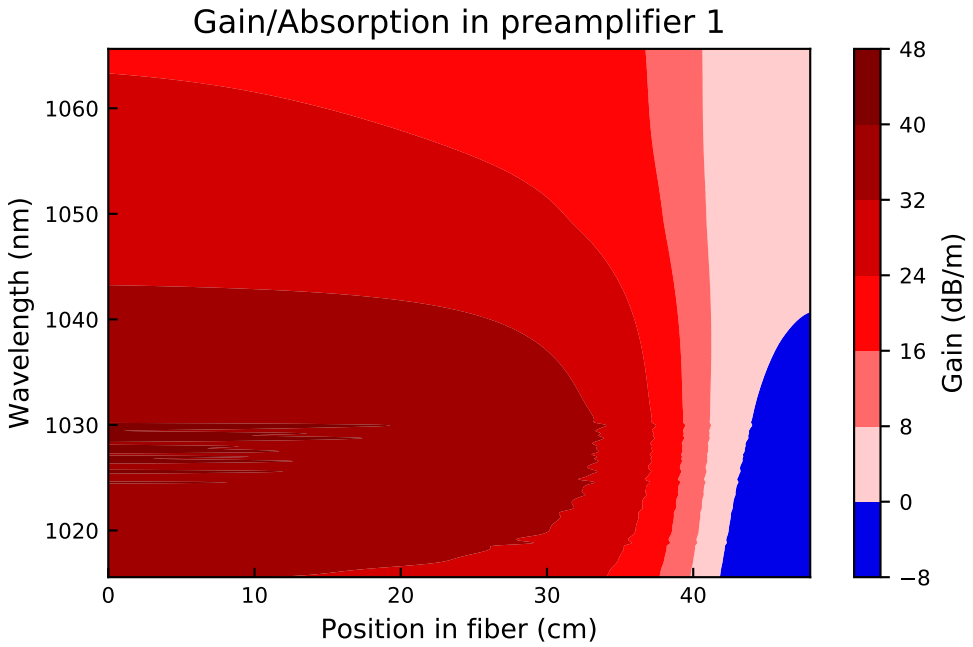

Figure 4.11. *Net gain in the first preamplifier at each wavelength and longitudinal position at 200 mW pumping.*

shorter fiber would have meant missing out on some gain while a longer fiber would have led to reabsorption. Despite the weak reabsorption at the end for wavelengths shorter than 1040 nm, the figure shows that they will experience overall higher gain in the fiber than longer wavelengths owing to the high excitation in the first three fifths of the fiber. In the ultrafast simulation, this can be expected to manifest as gain narrowing of the signal spectrum.

The newly calculated gain values were then used in the GNLSE model to propagate the ultrafast pulse through the first preamplifier, including the passive fibers and component losses in their correct order. The resulting pulse at the output is shown in fig. 4.12 and its parameters are listed in table 4.6.

Table 4.6. *Parameters of the simulated pulse after the first preamplifier.*

Pulse after preamplifier 1	
Energy	2.38 nJ
Peak power	6.35 W
Time duration (FWHM)	465 ps
Spectral width (FWHM)	4.12 nm
Time-bandwidth product	531

The pulse energy after the preamplifier is 2.38 nJ. The total average power calculated by multiplying the pulse energy by the repetition rate is 85.3 mW, which is in good agreement with the 83.6 mW power from the rate equation model. The slight increase in output power is caused by the 1038 nm spectral peak accumulating higher gain than the rate equation

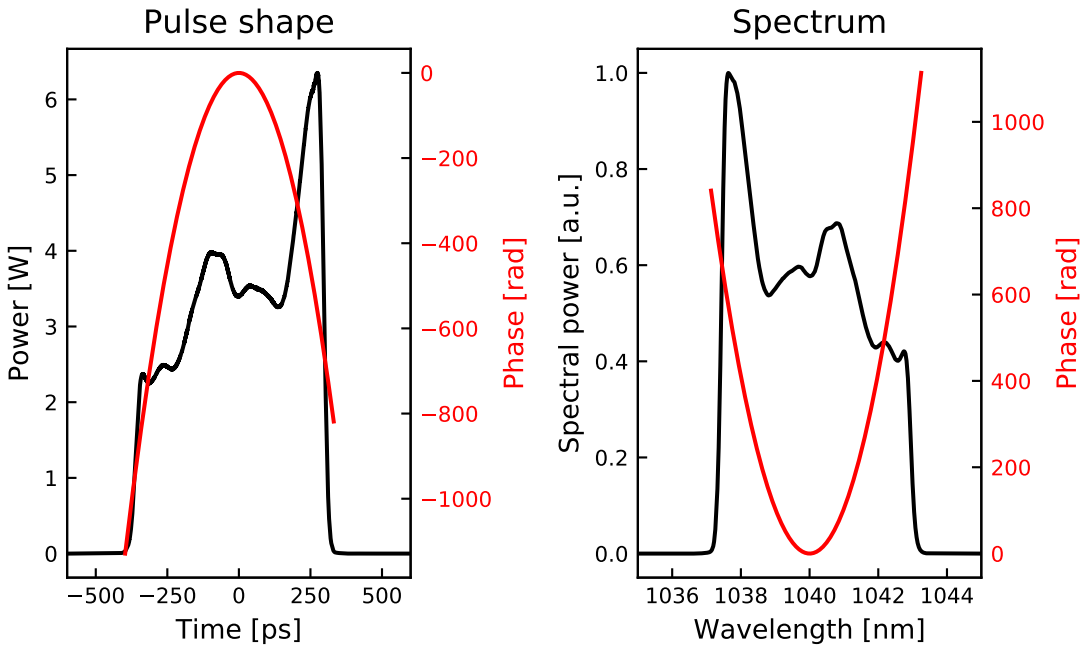

Figure 4.12. *Pulse shape and spectrum after propagating through the first preamplifier.*

model predicts for the 1040 nm signal. Still, the similarity of the output powers suggests that the spectrum does not change too much during amplification to render the chosen simulation method invalid.

The absence of SPM is also clear by looking at the spectrum, since the only effect on its shape is slight narrowing due to unequal gain. The simulated total B-integral accumulated in the first preamplifier is only 28 mrad, which also confirms that nonlinearity does not play any role at this peak power level and these fiber lengths yet. The stretched pulse shape in time domain, which closely mirrors the spectrum, shows equal narrowing caused by the sharp peak (which contains the 1038 nm light) receiving more gain than the rest of the pulse. The spectral and temporal narrowing indicated by the FWHM values in table 4.6 exaggerates the change in pulse shape. For example, the pulse duration has decreased from 568 ps after the stretcher to only 465 ps now which would suggest a major change not visible in fig. 4.12 but this is only because the pulse's leading edge is now slightly below the 50 % threshold and not counted in the FWHM calculation. In this sense, reporting the time window that contains 95 % of the total energy would perhaps be a more accurate method of quantifying the width of an irregular pulse like this.

4.1.4 Pulse picker

The next part of the CPA system is the pulse picker, which gates the pulse train in time domain and effectively reduces its repetition frequency for the purpose of reaching higher pulse energies with the average power divided between fewer pulses.

The scheme is shown in fig. 4.13 and includes the acousto-optic modulator (whose high-

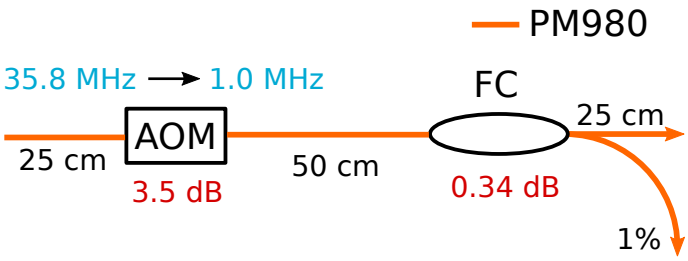

Figure 4.13. *Scheme of the pulse picker including the passive fiber lengths and component losses. AOM = acousto-optic modulator, FC = fused coupler (1/99)*

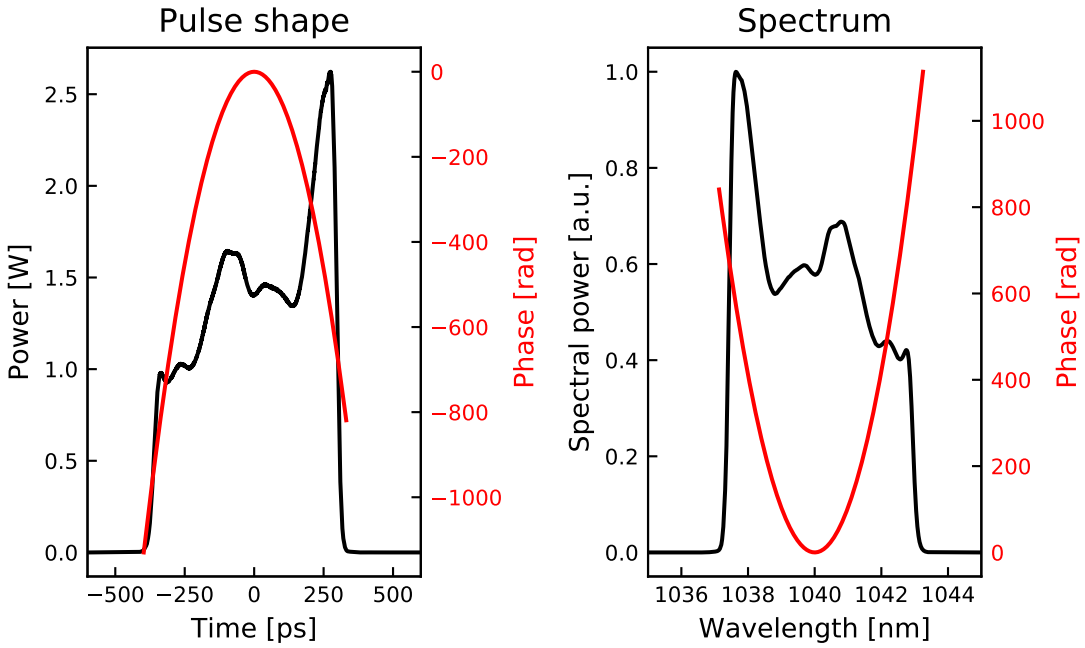

Figure 4.14. *The simulated pulse shape and spectrum after the pulse picker.*

power RF driver and control electronics are omitted) and a 1 % monitor coupler to observe the output repetition frequency. Again, fiber lengths and excess losses of the components are indicated in the figure. The AOM is modelled as lumped loss followed by a change in repetition rate (the exact order does not matter in reality). The loss in fig. 4.13 refers to the loss suffered by transmitted pulses, while the rejected pulses are assumed to be totally eliminated, which is valid as long as the AOM is fast enough.

In this scheme, the repetition rate is dropped from the original 35.8 MHz to 1 MHz. Exactly speaking, it is impossible to pulse-pick a 1 MHz pulse train from a 35.8 MHz one but the closest one can get (by transmitting every 36th pulse) is very close at 0.994 MHz. The difference being so minimal, the final repetition rate has been rounded to 1 MHz in the calculations. The drop in average power due to rejected pulses is also calculated based on the fraction of 1/35.8.

Given the short fiber lengths and the absence of highly dispersive components, the pulse shape can be expected to be mostly unchanged after the pulse picker. For the sake of completeness, the output pulse is still shown in fig. 4.14 and its parameters are listed in

Table 4.7. *Parameters of the simulated pulse after the pulse picker.*

Energy	0.98 nJ
Peak power	2.62 W
Time duration (FWHM)	465 ps
Spectral width (FWHM)	4.12 nm
Time-bandwidth product	531

table 4.7. The only real change is in pulse energy and peak power, which have decreased due to the losses. Average power has dropped even more due to the reduced repetition rate to 0.98 mW.

4.1.5 Preamplifier 2

Next, the pulse arrives in the second preamplifier, whose purpose is to boost the pulse energy to tens of nanojoules before amplification in the large-mode-area tapered power amplifier. Since the peak power becomes relatively high for single-mode fiber, the second preamplifier is designed in counter-pumped configuration where most of the amplification takes place at the output end of the active fiber. Additionally, Nufern PLMA-YSF-10-125 single-clad active fiber with 10 µm core diameter and corresponding PM1060L passive fiber with 8.5 µm core diameter were selected for this amplifier to avoid nonlinear effects. The scheme of the second preamplifier is shown in fig. 4.15 and the fiber parameters used in modelling in table 4.8 and table 4.9.

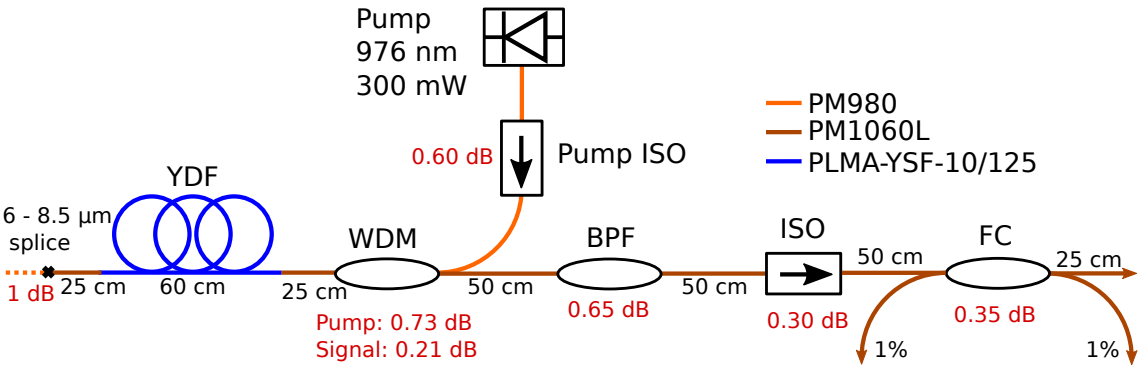

Figure 4.15. *The scheme of the second preamplifier, which is counter-pumped and based on LMA single-mode fibers. BPF = band pass filter, other labels like before*

The first significant point in the scheme is the splice from the 6 µm PM980 fiber to the 8.5 µm PM1060L fiber. Because of the large mismatch between the fibers' geometries, there is going to be significant loss at the splice unless a mode field adapter is used to match the mode shapes. Experimentally, splicing the fibers normally causes a loss of roughly 25 % (1 dB). However, as both fibers are single-mode, there is no loss of beam quality associated with the mismatched splice and the absolute power drop is small and can therefore be tolerated. As a result, the modelling assumes a "naïve" splice without a

Table 4.8. *Parameters used for modelling PM1060L passive fiber in the second preamplifier at 1040 nm.*

Core diameter	8.5 µm
Core NA	0.085
Second order dispersion β_2	$2.3 \cdot 10^{-26}$ s^2
Third order dispersion β_3	$4.4 \cdot 10^{-44}$ s^3
Nonlinear effective area A_{eff}	75 µm^2
Nonlinear coefficient γ	$2.0 \cdot 10^{-3}$ W^{-1} m

Table 4.9. *Parameters used for modelling PLMA-YSF-10/125 active fiber in the second preamplifier at 1040 nm.*

Core diameter	10 µm
Core NA	0.075
Second order dispersion β_2	$2.3 \cdot 10^{-26}$ s^2
Third order dispersion β_3	$4.4 \cdot 10^{-44}$ s^3
Nonlinear effective area A_{eff}	99 µm^2
Nonlinear coefficient γ	$1.5 \cdot 10^{-3}$ W^{-1} m
Yb^{3+} doping concentration	$3.72 \cdot 10^{25}$ m^{-3}
Cross sections	see fig. 2.2

mode-field adapter, which would add to the cost of the system. In principle, there would be some non-negligible splice loss between the passive and active fibers as well owing to their different mode sizes but those minor losses are neglected here. Such additional losses would be easily compensated even in a real-world CPA system by making the preamplifier a bit more powerful.

The fiber parameters in table 4.8 and table 4.9 unfortunately include some guesswork and estimation. The core diameters and numerical apertures are taken from the manufacturer's website [28] and used to calculate the mode shape and then the nonlinear parameters as previously assuming step-index geometry. However, there is no data available on the fibers' dispersion so PM980 dispersion values are used instead. In reality, one would expect the dispersion to be weaker due to the larger core and lower NA reducing the waveguide dispersion effect. Assuming a higher dispersion is therefore the worst case scenario since the additional dispersion must be compensated at the compressor. The active fiber's spectroscopic data and doping concentration are similarly unclear but the simulation uses the same values used for PM-YSF-HI-HP, which should be close to reality.

In total, the second preamplifier is slightly more complex than the first one. Being backward pumped, it starts with the active fiber, followed by a filter based WDM used to couple in pump light. The 976 nm wavelength-stabilized 300 mW pump diode is more powerful than in the first amplifier since the gain requirement is also higher here. A pump isolator

is included to protect the diode, but experimental tests would almost surely confirm that it is unnecessary. The next component is a 12 nm band pass filter centered at 1040 nm, whose purpose is to avoid long-wavelength ASE light going into the tapered amplifier where it might seed stimulated Raman scattering. In this numerical model, the effect of the filter is just loss and an imperceptible reshaping of the spectrum since ASE noise is only considered within each amplifier and Raman is not the limiting factor of the system as hinted in the beginning of this chapter. After the filter, there is a high-power isolator designed to block backward ASE from the power amplifier. Compared to the low-power isolator, this one has a much lower loss of only 0.3 dB, but the downside is its much higher cost and bulkiness. Between the filter and the tapered fiber amplifier, there is a 1 % monitor coupler for diagnostics and a cladding-mode stripper (CMS) made at the splice between the taper and the passive fiber. The CMS is not shown in fig. 4.15 and does not cause extra loss to the signal. The coupler's monitor ports should be angle-polished to avoid back reflection, especially towards the tapered amplifier but, as before, back reflected signals are not considered in the numerical model.

From the modelling point of view, the second preamplifier is handled in much the same way as the first preamplifier by first optimizing the active fiber length, followed by the calculation of the active fiber's ion excitation as well as the amplifier's slope efficiency at the optimal fiber length using the CW rate equation model. The excitation is then used to calculate net gain at each wavelength and at each point in the active fiber, and finally, the ultrashort pulse is propagated through the whole amplifier using the GNLSE model.

Starting with the active fiber length optimization, the signal power reaching the active fiber after the splice loss is 0.74 mW, while the pump light suffers losses both at the pump isolator and at the WDM resulting in 221 mW being finally coupled into the active fiber. As before, 80 channels of both forward and backward ASE were modelled in addition to the signal and pump beams. The results of varying the fiber length are shown in fig. 4.16.

The optimum length is 60 cm, resulting in 60.6 mW output power at the end of the active fiber. The shape of the curve is like the one presented for the first preamplifier but there are some notable differences too. First, the output power is much lower here despite the longer active fiber and higher available pump power. This is due to the weak input power combined with the fiber's larger core size, which makes it more difficult to saturate, leading to more of the pump power being lost to spontaneous emission to maintain inversion in the fiber. Similarly, the reabsorption loss, which takes place at the start of the active fiber in this case, is also more severe here since the thicker fiber can absorb more signal power before reabsorption is saturated. Again, in a real system, the fiber length and the pump power should be selected based on the lowest possible input power, though only the single input power is considered in this thesis. The power evolution and excitation using 60 cm active fiber is shown in fig. 4.17.

The ytterbium excitation is high in most of the fiber expect at the very beginning where the backward-propagating pump has been already depleted. Due to the low signal input power, gain is rather high at 19.1 dB but not high enough to generate significant ASE at

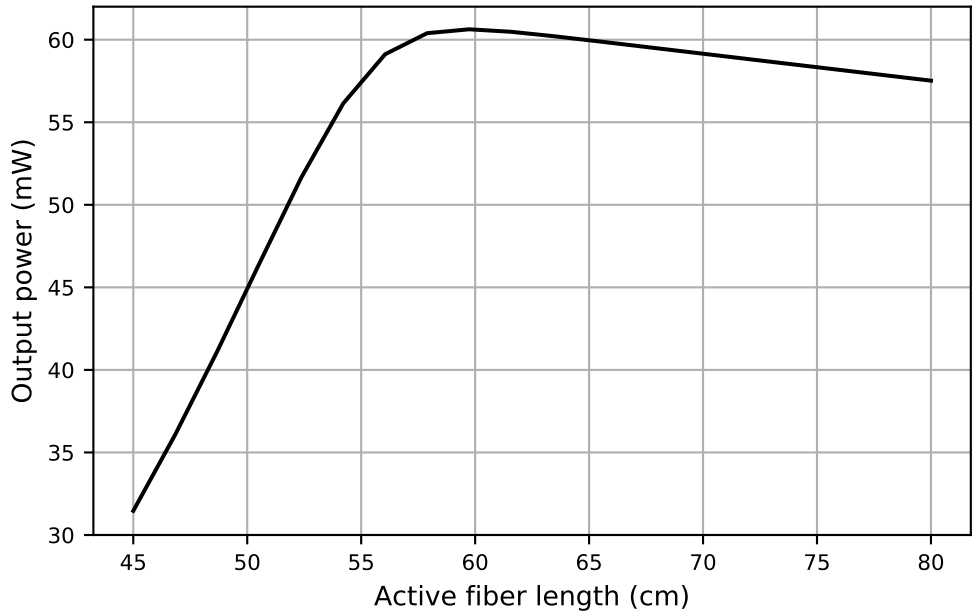

Figure 4.16. *The output power of the second preamplifier as a function of active fiber length obtained from the rate equation simulations while keeping signal and pump powers constant. The optimum fiber length is 60 cm.*

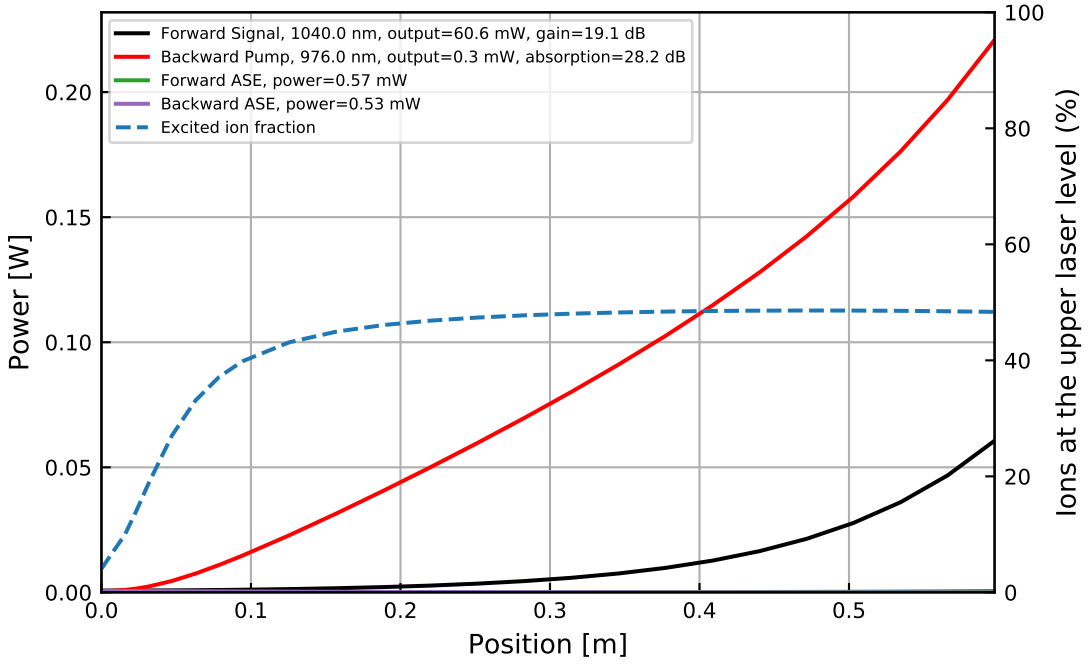

Figure 4.17. *The simulated optical powers and Yb^{3+} ion excitation in the second preamplifier at 60 cm active fiber length and 300 mW pumping before pump losses.*

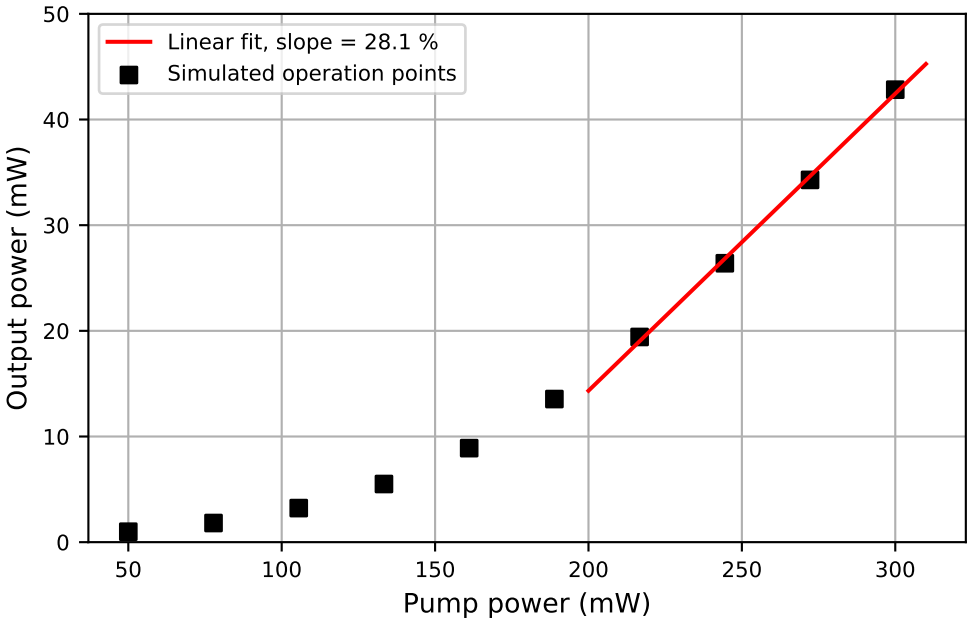

Figure 4.18. *The simulated slope efficiency of the second preamplifier at 60 cm active fiber length is 28.1 %.*

the output since the total forward ASE power of 0.58 mW remains more than two orders of magnitude below the signal power.

Next, the pump power was tuned while keeping the signal power and active fiber length constant to find the slope efficiency of the amplifier. The results of that set of simulations are shown in fig. 4.18. At low pump powers, the relationship between output power and pump power is not linear since pump has not yet reached the input side of the active fiber and, consequently, signal is still being absorbed there. When pump power is increased, the signal absorption is reduced, and efficiency grows until the slope becomes approximately linear at 28.1 %. It is notable, though, that the total conversion efficiency at 300 mW pump power and the corresponding 42.8 mW signal power after the components is only 14 %.

To prepare for the GNLSE simulation, the ion excitation from fig. 4.17 was used to calculate net gain in the second preamplifier at each wavelength of the pulse's spectral window and at each position in the fiber. The result is shown as contour plot in fig. 4.19. The familiar caveat applies that the overlap between signal and the ions was assumed constant at its 1040 nm value of 0.803 to avoid calculating Bessel mode shapes for each of the 2^{14} wavelengths.

Figure 4.19 shows that the start of the active fiber would absorb any signal at wavelengths under 1040 nm, which is consistent with this being the optimal fiber length for exactly 1040 nm amplification. In the rest of the fiber, though, gain at around 1030 nm is much stronger than at 1040 nm, which more than balances out the small initial absorption, and which we can guess will lead to further gain-narrowing of the signal spectrum during amplification.

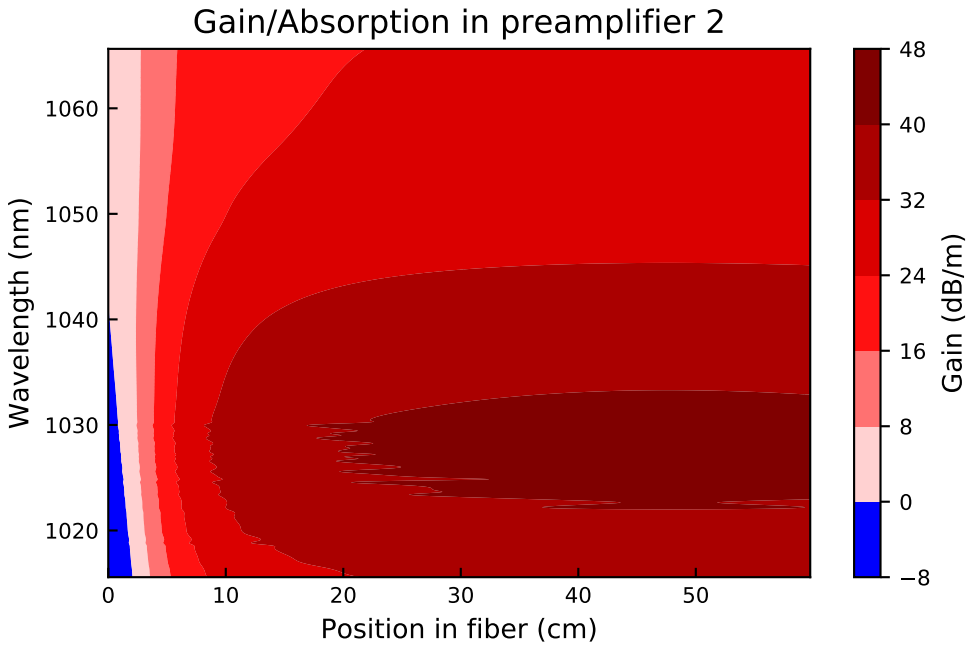

Figure 4.19. *Net gain in the second preamplifier at 300 mW pumping at different wavelengths and positions.*

Table 4.10. *Parameters of the simulated pulse after the second preamplifier.*

Energy	42.8 nJ
Peak power	134.7 W
Time duration (FWHM)	138 ps
Spectral width (FWHM)	3.62 nm
Time-bandwidth product	139

This is indeed what happens when looking at the pulse shape and spectrum after the GNLSE pulse propagation through the whole second preamplifier presented in fig. 4.20 and at the pulse's parameters listed in table 4.10. The short wavelength side of the pulse has received so much more gain that the full-width-at-half-maximum pulse duration has dropped to 138 ps and the spectral width to 3.62 nm. The drastic drop in the FWHM pulse duration overemphasizes the change in pulse shape, though, since most of the pulse energy resides in the broad part, which is now just under the half maximum value due to stronger amplification for the 1038 nm peak. The pulse energy going to the tapered fiber is 42.8 nJ with 135 W peak power at the sharp peak. The average power calculated from the pulse energy and repetition rate is 42.8 mW, which matches exactly the value predicted by the rate equation simulation. The fact that there is no difference could possibly be due to weak nonlinear broadening in the amplifier compensating for the gain narrowing. In any case, this result justifies the use of the excitation values from the rate equation simulation.

The GNLSE simulation also predicts that the pulse accumulates a non-negligible B-

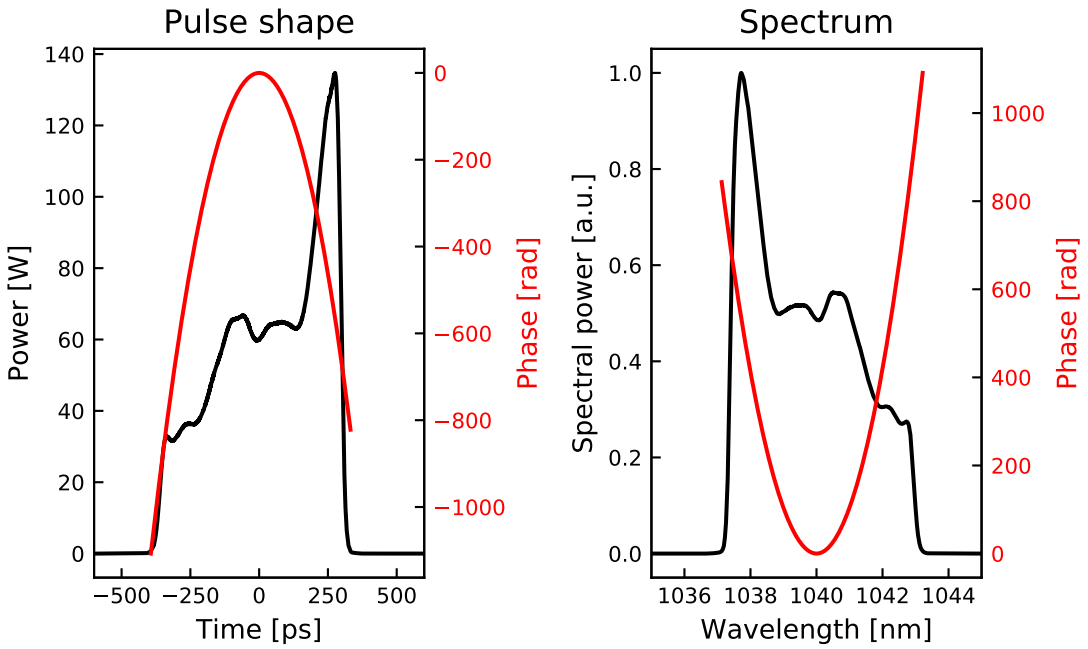

Figure 4.20. *The simulated pulse shape and spectrum after the second preamplifier.*

integral of 0.68 rad during its propagation in the second preamplifier. Therefore, selecting large-mode-area single-mode fibers in the amplifier was the right choice as using 6 µm fibers would have made the B-integral approximately twice larger. The accumulated nonlinear phase (mostly by the sharp 1038 nm peak) is not yet visible in the spectrum but it should optimally be reduced somehow when building the real laser system. One way would be to use a smoother spectrum, which would not give rise to narrow peak in the temporal shape after the stretcher. Also, the necessity of the band-pass filter and the monitor coupler should be considered since removing either of them would reduce the passive fiber length at the output of the second preamplifier by 50 cm and considerably lower the B-integral. Pumping could also be reduced if a lower seed power can saturate the tapered fiber amplifier. Pumping at 200 mW instead of 300 mW reduces the accumulated B-integral in the second preamplifier to 0.23 rad but output power drops too to 15.5 mW. Section 4.2 will evaluate the effect of reducing pump power from the whole system's perspective.

4.1.6 Tapered power amplifier

After the second preamplifier, the pulse enters the power amplifier based on tapered double-clad fiber. The fiber used in these simulations is one from an earlier generation of Ampliconyx tapers, which I have previously experimentally characterized. The longitudinal thickness profile of the 4.27 m long taper is shown in fig. 4.21. The core diameter of the taper varies from 13.5 µm at the narrow side to 42 µm at the wide side. The cladding diameter at the wide side is 391 µm measured with the Vytran glass processing machine, resulting in a core-to-cladding diameter ratio of 0.107.

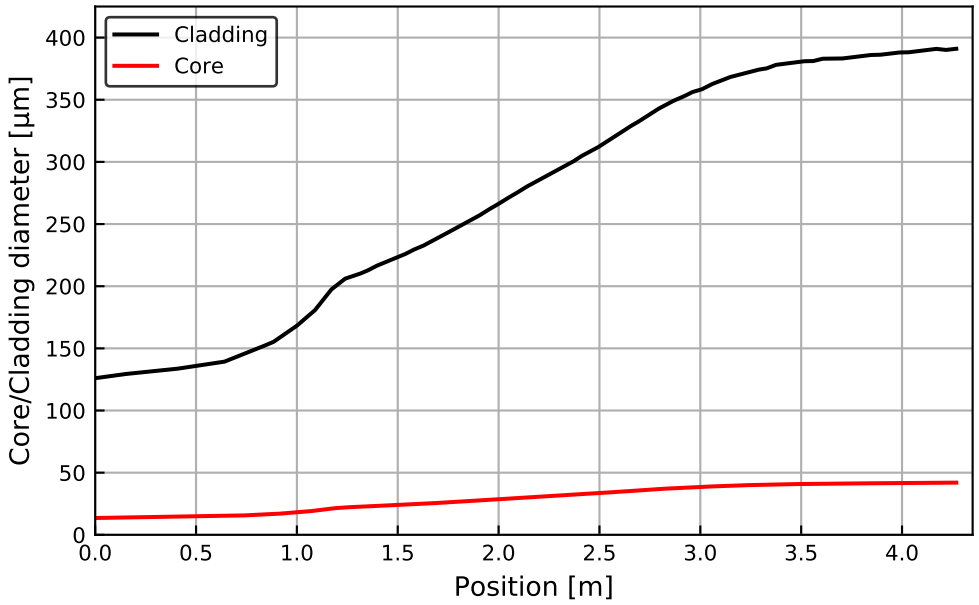

Figure 4.21. *The taper profile, i.e. core and cladding diameters vs. position in the tapered fiber used in this thesis.*

Table 4.11. *Parameters used for modelling the tapered double-clad fiber at 1040 nm.*

Core diameter	13.5 - 42 µm
Core-to-cladding ratio	0.107
Core NA:	0.08
Second order dispersion β_2	$2.3 \cdot 10^{-26}$ s^2
Third order dispersion β_3	$4.4 \cdot 10^{-44}$ s^3
Nonlinear effective area A_{eff}	128 - 800 µm^2
Nonlinear coefficient γ	$1.2 \cdot 10^{-3}$ - $0.2 \cdot 10^{-3}$ W^{-1} m^{-1}
Yb^{3+} doping concentration	$6.7 \cdot 10^{25}$ 1/m^3
Cross sections	see [70]

The taper's parameters required for the numerical simulations are listed in table 4.11. Unfortunately, the values of many of those parameters are uncertain, so some estimation is unavoidable. The core numerical aperture is estimated as 0.08 and, fortunately, any uncertainty concerning it does not have a major effect on the results since the shape of the fundamental mode depends only weakly on NA at large core diameters. Dispersion values have not been measured (and would in fact be difficult to measure locally at each point of the taper), so the PM980 values are again used, representing the worst case scenario. Nonlinear effective area and the coefficient γ are computed based on the fiber's geometry and should be fairly realistic. These parameters are not constant but vary along the length of the taper together with the increasing core size. The fundamental mode shape was calculated at each point in the taper and then used to compute the nonlinear effective area and γ. The maximum and minimum values of those parameters are included in table 4.11, corresponding to the input and output ends of the fiber (the

effective area is at its largest at the output resulting in the minimum value for γ). Since the absorption and emission spectra for the core material are not available, generic spectra from [70] have been used instead. The doping concentration has then been scaled to $6.7 \cdot 10^{25}$ 1/m^3 to match the experimentally measured core absorption of 700 dB m^{-1} at 976 nm at the narrow side of the taper. Not knowing the exact emission cross sections at the signal wavelengths does not prevent obtaining meaningful results in this case since gain in double-clad active fibers is normally limited by the rate of pump absorption and not by the rate of stimulated emission.

In an identical way to the preamplifiers, the taper is first modelled using CW rate equations to obtain the ion excitation. This time, though, it is not possible to vary the fiber length so it is kept fixed. The taper is backward pumped with a wavelength-stabilized multimode 976 nm laser diode. The first simulation uses a pump power of 100 W. Additionally, a pump coupling loss of 10 % is included, caused mostly be Fresnel reflections at the ends of the pump fiber and the taper, neither of which is assumed to have an AR coated end cap at this power level.

Since the pump beam propagates in the cladding, it only partly overlaps with the ions in the core. The simulation uses the simplest possible approximation that the overlap integral between the pump and the ions equals the ratio of core and cladding cross sectional areas. This implies perfect mode mixing in the cladding due to the Panda stress rods. Experimentally, this is not exactly true and there would be some cladding modes that do not overlap with the core and consequently the pump power in those modes would propagate through the taper unabsorbed. Handling the cladding modes in greater detail would likely have a noticeable effect but the effort would have been too large to include such simulations in this thesis. For each signal and ASE channel propagating in the core, the rate equation simulation calculates the correct Bessel mode shape and overlap integral at each point in the taper. The vignetting effect, i.e. pump leaking out as it propagates towards the narrow part of the taper, is modelled after [71] but finer details, such as the effect of the NA of the pump radiation coupled into the taper, are not considered.

The signal average power going into the taper is directly the 42.8 mW generated by the second preamplifier. A single signal channel is used in the rate equation model like in the preamplifiers but due to the earlier gain narrowing of the spectrum the signal wavelength is calculated as the "center of mass" of the pulse's spectrum, which is 1039.6 nm instead of 1040 nm. Single-mode ASE is modelled with 50 channels at equidistant wavelengths going both backward and forward at 1000-1100 nm. Since the thick end of the taper is highly multimode, it can support multimode ASE, and more of the fiber's spontaneous emission captured by the core than in a single-mode fiber, proportional to the number of guided modes. On the other hand, this ASE would mostly leak out of the core when propagating towards the narrow side, having only a limited negative impact on the taper's conversion efficiency. For the sake of simplicity, multimode ASE has been excluded from the rate equation simulations. Experimentally, ASE has not been a problem at input power levels of $>$10 mW. The results of the first simulation with the parameters and

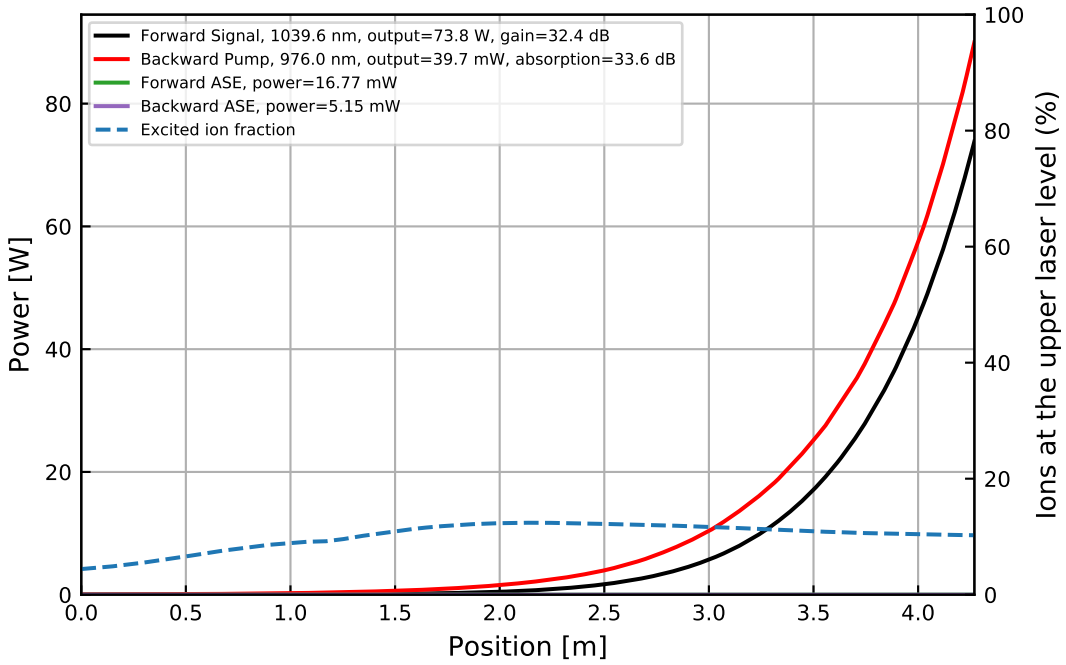

Figure 4.22. *Optical power evolution and ion excitation in the tapered active fiber at 42.8 mW input signal and 100 W pump power (before 10 % coupling loss).*

caveats described above are shown in fig. 4.22.

The signal experiences of total gain of 32.4 dB resulting in an output power of 73.8 W before the Fresnel reflection at the taper's end face and 70.9 W in free space. Practically all pump power has been either absorbed or vignetted out when it reaches the input part of the taper, which is not entirely realistic as clarified above. Due to the limited rate of pump absorption in the double-clad fiber, the ion excitation stays relatively low and even over the whole length of the fiber. The good saturation of the taper also results in single-mode ASE power remaining orders of magnitude lower than the pulsed signal at the output. Consequently, ASE channels are excluded from the rest of the taper rate equation simulations for computational speed.

Next, the tapered fiber amplifier was simulated at different pump powers to obtain its slope efficiency. The result is shown in fig. 4.23. The signal powers include the 4 % loss due to Fresnel reflection at the end of the taper while the collimation lens and the dichroic mirror are assumed to be lossless. The obtained curve is very much linear and the slope efficiency is 75.2 %, which is only slightly higher than the experimentally measured 71.4 % for this taper. A more accurate handling of the pump beam absorption in the taper (= less pump absorbed) would possibly bring the two numbers into an even better agreement.

To compute the gain in the taper for the GNLSE simulation at 100 W pump power, the ion excitation from fig. 4.22 was taken and the net gain calculated in the same way as for the preamplifiers. The wavelength dependence of the overlap integral was excluded by using the 1040 nm values, which varied from 0.917 at the narrow end to 0.996 at the wide end. When the core is this large, it would be more accurate to divide it transversally into

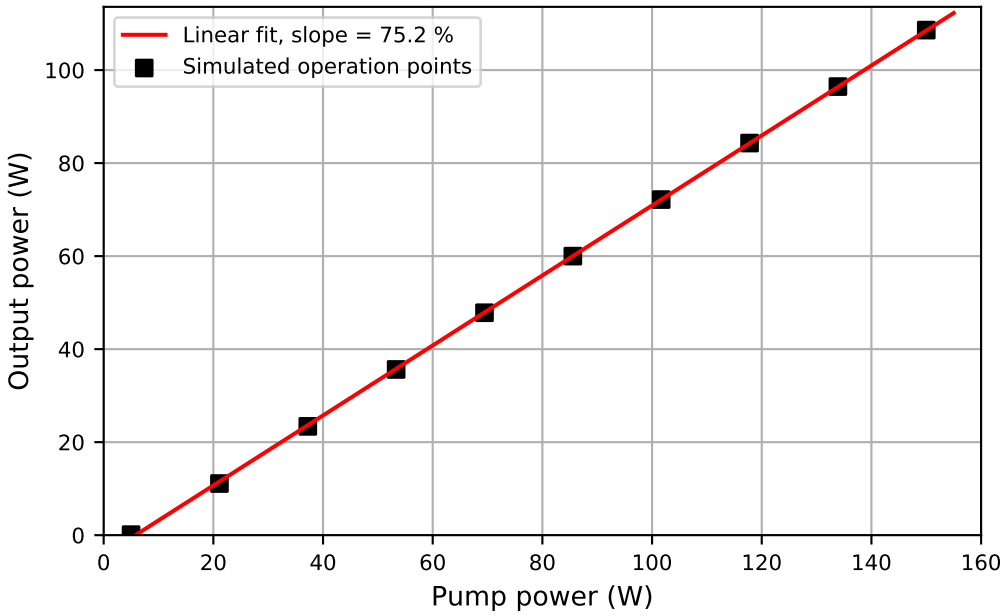

Figure 4.23. *The slope efficiency of the tapered fiber amplifier was 75.2 % at 42.8 mW input signal assuming a 10 % pump coupling loss and 4 % Fresnel reflection loss for the signal.*

multiple concentric rings and handle the ion populations in them separately because the fundamental mode's irradiance (and consequently ability to cause stimulated emission) varies greatly from the center of the core than to the edges. This is not difficult feature to add in principle but was left out to limit the complexity of the numerical algorithm. The gain distribution is depicted as a contour plot in fig. 4.24.

Since the excitation in the tapered fiber is much lower than in the preamplifiers, gain maximum is shifted to longer wavelengths of approximately 1040 nm to 1060 nm. At 1030 nm, the first about 75 cm of the fiber actually absorbs the signal with 1040 nm also experiencing minor absorption at the start of the taper even at this relatively high pump power of 100 W. This gain distribution is positive news for the considered pulse, however, since the pulse's spectrum previously suffered gain narrowing in opposite direction in the preamplifiers. We can expect the gain tilt in the taper to compensate for at least part of the earlier gain narrowing.

Using the precomputed gain, the pulse was next propagated through the taper with the GNLSE model. The result is shown in fig. 4.25. It is evident that part of the gain narrowing has been reversed as the sharp peak has lost in power compared to the rest of the pulse. However, even clearer is that the pulse has suffered from excessive SPM causing the irregular spikes in its spectrum. The accumulated nonlinear phase is masked in the phase plot by the background of massive dispersion from the stretcher but we can expect the compression of this pulse with the grating pair to be difficult, even though the stretched pulse shape is still mostly unchanged. In fact, the simulation shows that the pulse accumulates a total B integral of 17.9 rad in the taper. The parameters of the

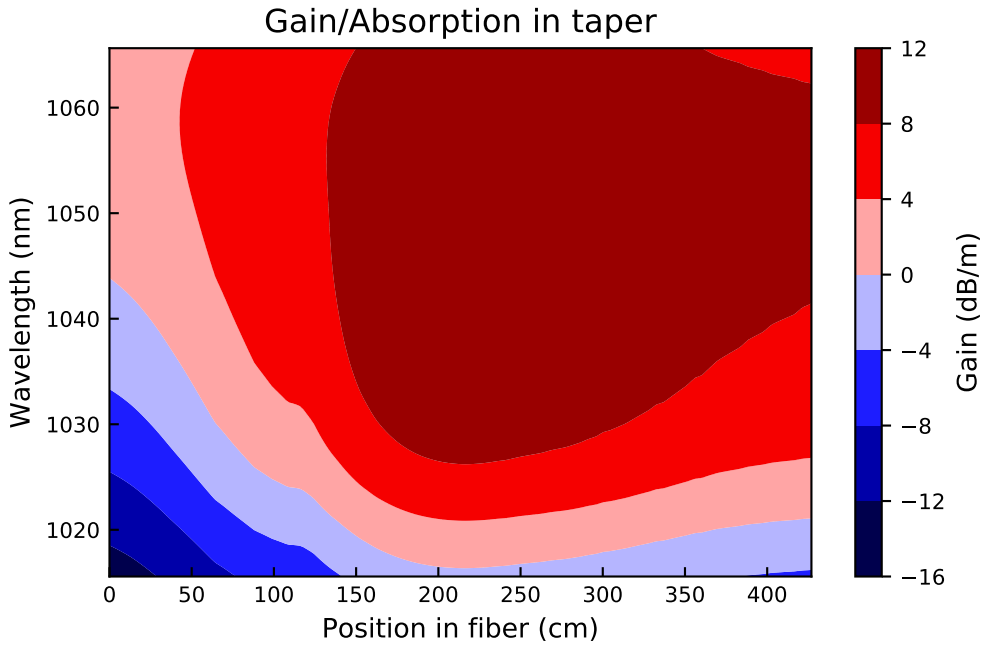

Figure 4.24. *Gain at different wavelengths and positions in the tapered fiber amplifier under 100 W pumping and 42.8 mW, 1039.6 nm input signal.*

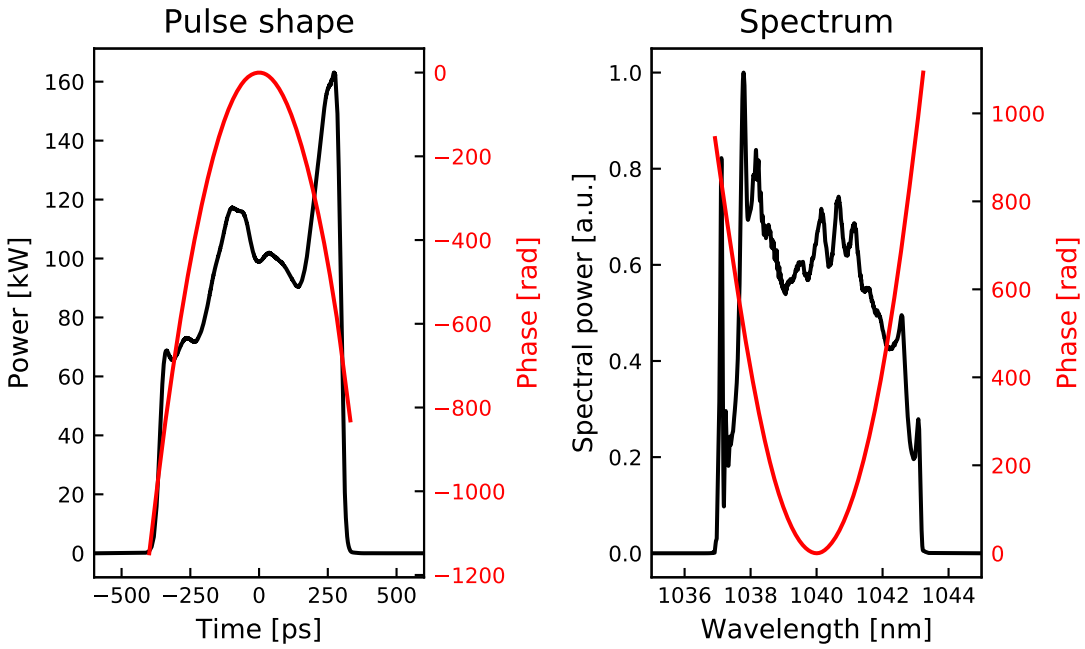

Figure 4.25. *Pulse shape and spectrum after the tapered fiber amplifier assuming 42.8 nJ input pulse energy and 100 W pumping.*

Table 4.12. *Parameters of the simulated pulse after the tapered power amplifier.*

Energy:	67.4 µJ
Peak power:	163 kW
Time duration (FWHM):	491 ps
Spectral width (FWHM):	4.79 nm
Time-bandwidth product:	652

amplified pulse are listed in fig. 4.25 for easy reference.

The average power found by multiplying the pulse energy by the repetition rate is 67.4 W and deviates somewhat from the rate equation simulation result of 70.9 W. However, the deviation affects the pulse energy only by a few percent so it can be deemed acceptable. With stronger self-phase modulation, we would expect this deviation to become larger. Here, even though SPM has modified the spectrum, the newly generated frequencies are still within the original bandwidth not very far from 1040 nm, which justifies using the gain values from the rate equation simulation. Using a larger number of channels corresponding to the pulse's different spectral components in the rate equation simulation might additionally improve the agreement of the two power values.

4.1.7 Compressor

The amplified pulse finally arrives at the last element of the CPA system, which is a free-space grating pair compressor in Treacy configuration. The modelled fused silica transmission gratings are from Lightsmyth with the parameters listed in table 4.13. Their design wavelength is 1030 nm, but their specified diffraction efficiency variation with wavelength confirms that they are usable at 1040 nm too.

Table 4.13. *Parameters of the transmission gratings in the Treacy compressor.*

Line density:	1739.13 mm^{-1}
Diffraction efficiency at 1040 nm:	94 %
Littrow angle at 1040 nm:	64.74°

The grating pair is modelled as a combination of lumped loss and second and third order dispersion similarly to the stretcher. The total transmission is 78.1 % after the four passes through a grating. The mirrors in the compressor are assumed to be perfectly reflective. The variation of diffraction efficiency with wavelength is weak and the spectrum is narrow so the efficiency is assumed to be constant over the pulse spectrum. Similarly, the incidence angle is assumed to be tunable by ±3° around the Littrow angle without affecting the diffraction efficiency. A more accurate model would include the variation of the gratings' efficiency but that would also require measuring or perhaps simulating the gratings themselves to find the necessary parameters. The grating size also matters since the pulse's spectrum would be clipped if the second grating were too small to accommodate

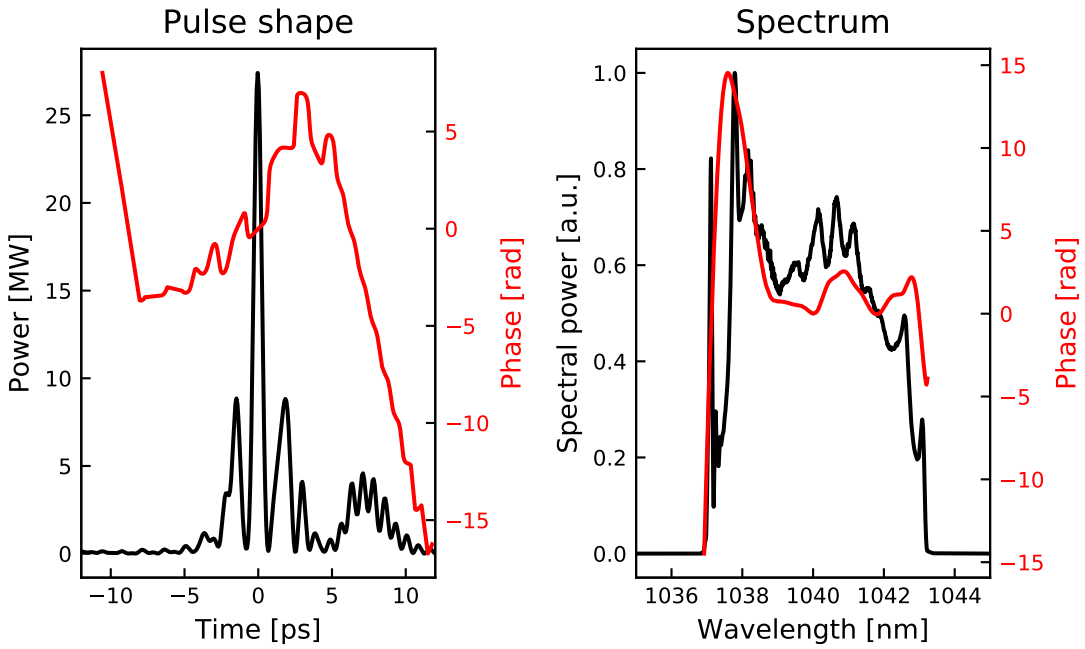

Figure 4.26. *The pulse shape and spectrum after the optimized grating compressor.*

the spatially chirped beam. In this case, large enough gratings have been chosen, and spectral clipping is not considered further. It must be noted that spectral clipping could also have a beneficial effect if the edges of the spectrum were difficult to compress in which case simply filtering them out would be preferable.

The grating compressor has two independently tunable parameters: the distance between the gratings and the incidence angle. The compressor is numerically optimized by tuning both of them until the maximum peak power for the compressed pulse has been found. In practice, the optimization task is given to a global optimizer algorithm (*scipy.optimize.basinhopping* in Python) since there are multiple local maxima due to the complex shape of the pulse and its phase. Peak power has been chosen as the figure of merit because it is straightforward to compute and gives a good indication of the CPA system's performance. Pulse duration would be a poor choice as the optimization target since there is no single always applicable measure of pulse width. Probably some kind of flatness measure of the spectral phase would work but that would be more difficult to interpret than peak power.

In the case of the pulse after the taper in fig. 4.25, the optimization results in an angle of incidence of 67.18° and a grating separation of 55.5 cm, which translates to $\beta_2 = -67.9\,\mathrm{ps}^2$ and $\beta_3 = 0.959\,\mathrm{ps}^3$. The pulse after this optimized compressor is shown in fig. 4.26 and its parameters are listed in table 4.14.

It is clear that the pulse has been compressed poorly. In time domain, there is a sharp peak reaching to 27.4 MW peak power but most of the energy resides in side pulses distributed within a time window of roughly 15 ps in duration. The FWHM pulse duration and time-bandwidth product presented in the table do not therefore properly reflect reality

Table 4.14. *Parameters of the simulated pulse after the optimized compressor.*

Energy:	52.6 µJ
Peak power:	27.4 MW
Time duration (FWHM):	0.63 ps
Spectral width (FWHM):	4.79 nm
Time-bandwidth product:	0.84

since they fail to take the side pulses into account. The earlier section already noted that the nonlinear phase accumulated in the taper would be problematic so the poor compression is not particularly surprising. In fact, looking at the spectral phase of the pulse gives a clear indication that the nonlinear phase is the problem. The uncompensated spectral phase follows quite closely the pulse shape of the input signal, and the stretched pulse in time domain pulse is nearly a one-to-one mapping of the spectrum in this kind of CPA system with strong stretcher dispersion. The fact that the uncompensated nonlinear phase matches the pulse shape also gives a hint that the nonlinear phase of a less irregular seed spectrum/pulse would be more easily compensated for in the compressor. As this poor compressibility is a disappointing result, the rest of this chapter will look into ways to optimize the CPA system for improved operation.

4.2 Performance optimization of the CPA system

In the previous section, the model of the CPA system was covered in detail fiber-by-fiber and component-by-component, including the parameters, assumptions and limitations associated with the simulating each of them. With the complete model, it is now possible to tune some parameters, propagate the pulse through the whole amplifier chain and observe the changes in the compressed output pulse. The purpose of this section is to do just that. Three scenarios will be tested. The first is to tune the pump currents in the second preamplifier and the tapered amplifier. Lower pump currents should self-evidently mitigate nonlinearity and lead to better compressibility of the pulse at the expense of a lower pulse energy, but the effect should be quantified. The second test involves varying the dispersion of the stretcher CFBG within its tuning rage. The third is to consider a different seed laser altogether; one that generates ideal Gaussian pulses with the same spectral width as the original experimental seed used so far. In this section's simulations, the CPA system described earlier is assumed to be unchanged. In other words, the fiber lengths are not reoptimized for each different signal power but the ion excitations and gains in the active fibers are recalculated for each new signal or pump power. Similarly, the compressor's incidence angle and grating separation are reoptimized for each pulse separately.

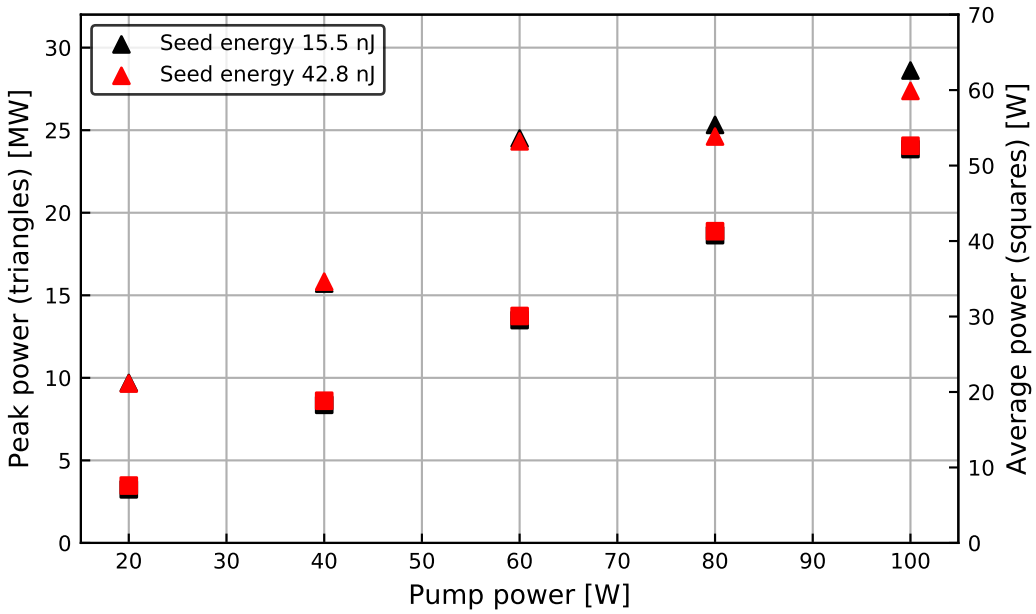

Figure 4.27. *Output average and peak powers as a function of pump power in the power amplifier, including a comparison with two different seed powers going into the tapered amplifier.*

4.2.1 Pump power tuning

Pump powers are the easiest aspect to change, especially to lower, in an existing fiber laser system. The hypothesis is that dropping the seed pulse energy decreases nonlinearity in the taper by shifting amplification more towards the wide end while incurring only a minor loss in slope efficiency. On the other hand, reducing pump power going into the tapered power amplifier has no real prospect of increasing peak power because the output pulse energy also drops as a consequence. However, it makes sense to try to understand how the compressibility of the pulses deteriorates as a function of pump power in the power amplifier. To examine these issues, a set of simulations was performed at pump powers ranging from 20 W to 100 W for the taper and at two different seed pulse energies of 42.8 nJ (original) and 15.5 nJ (lowered) corresponding to 300 mW and 200 mW pump powers in the second preamplifier. The results are shown in fig. 4.27.

Irrespective of the seed pulse energy, the average powers grow linearly and at very similar rates when the multimode pump power is raised from 20 W to 100 W, the slope efficiency matching the one calculated in fig. 4.23. This means that reducing the seed pulse energy does not indeed lead to a notable reduction of power conversion efficiency and the lower seed pulse energy can be used equally well.

The peak powers tell a more interesting story. In the beginning, they also grow linearly in step with the average powers but this behavior comes to an end at 60 W pumping. After that, the growth in peak power flatlines meaning that additional pumping no longer increases the achievable peak power. In other words, the results suggest that the pulses stay reasonably compressible until 60 W pumping but any additional pulse energy beyond

that ends up in the side or satellite pulses after compression. Figure 4.28 shows the result with the best peak power 28.7 MW at 15.5 nJ seed pulse energy and 100 W pumping. Comparing it to the full seed power simulation result in fig. 4.26 shows that the side pulses have marginally different shapes but still contain most of the power in time domain, and the 5 % increase in peak power over the earlier result is almost negligible.

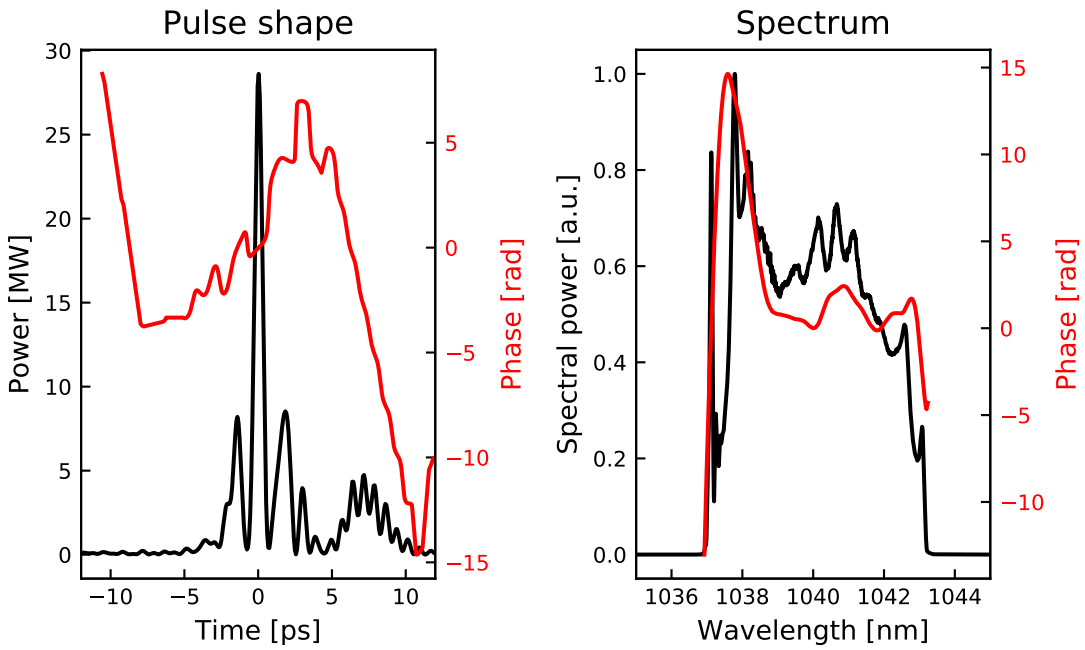

Figure 4.28. *The simulated pulse after the compressor with 15.5 nJ seed energy and 100 W taper pumping.*

In practice, amplifying the side pulses would be wasteful, and the laser should be operated at 60 W pump power instead where the pulse is much more compressible. That pulse after the compressor is shown in fig. 4.29. Its peak power is almost as high as before at 24.5 MW despite the roughly 23 µJ lower pulse energy (29.5 µJ vs. 52 µJ) since the side pulses have been greatly reduced. However, the pulse still accumulates a B-integral of 8.9 rad during propagation in the taper, which is visible in the uncompensated nonlinear spectral phase, which has the same shape but lower magnitude compared to fig. 4.28 and the still evident side pulses.

The most important conclusion from these simulations is that reducing seed pulse energy does not materially affect the power conversion efficiency in the tapered amplifier but is simultaneously unlikely to improve the compressibility of the output pulses. Speaking from experimental experience, the simulations suggests that SPM works differently to stimulated Raman scattering in this regard. SRS normally represents the main limitation to scaling pulse energy in tapered amplifiers when compressibility is not considered. To reduce SRS generation in those cases, a lower seed pulse energy has a moderate positive influence. Since any Raman signal generated in the narrow part of the taper has the whole length of the taper to grow further exponentially, avoiding high peak powers at the narrow side is beneficial in reducing Raman. However, the same does not appear to hold

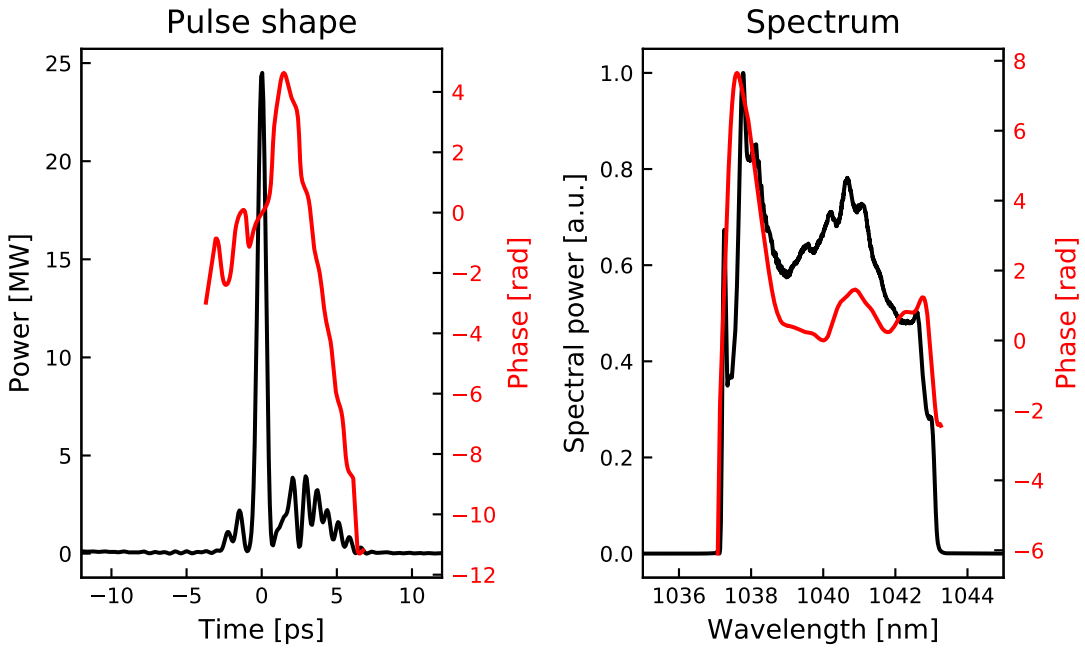

Figure 4.29. *The simulated pulse after the compressor with 15.5 nJ seed energy and 60 W taper pumping.*

for self-phase modulation. At modest pump powers, there is no difference in the achievable peak power between the 15.5 nJ and 42.8 nJ seed pulse energies and at $>$60 W pump power, the difference is still very minimal in favor of the lower seed energy. Physically, this simulation result makes sense since the pulse accumulates most of its nonlinear phase at the end of the taper where the peak power is at its highest and approximately independent of the seed pulse energy. The narrow part, where the pulse energies still differ, has only very limited significance for SPM unlike for Raman generation.

Even though no clear improvement in peak power was obtained based on these simulations, they show that the pulse can be made more compressible at the expense of greatly reduced pulse energy. In total, these results should mostly be considered as finding a better operation point for the CPA system rather than as an actual enhancement in its optical output.

4.2.2 Stretcher dispersion tuning

The next issue investigated with the full system model was tuning the stretcher's dispersion. Both β_2 and β_3 can be tuned and their tuning ranges are 7.0 ps^2 and 1.8 ps^3, respectively. Restricted by the computational load, the simulations first tuned β_2 to its optimum and then did the same for β_3 while keeping β_2 constant instead of optimizing both simultaneously. The results will show, though, that the resulting output peak power behaves smoothly when the dispersion is tuned so we can be relatively certain of finding the overall optimum. The 15.5 nJ seed pulse energy is used in these simulations based on its narrow advantage in the previous section. Pump power is set at 100 W since we

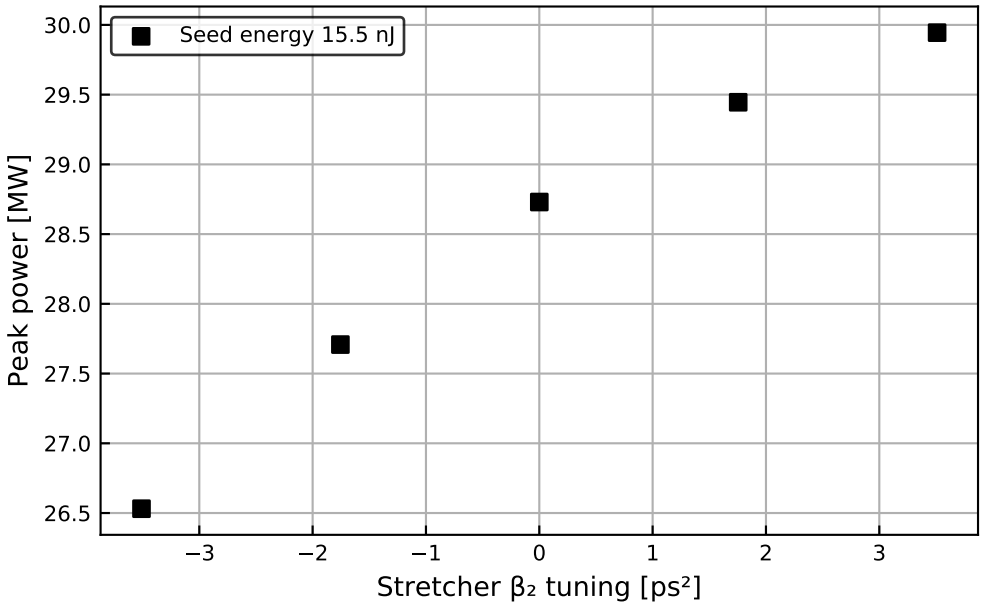

Figure 4.30. *The output peak power at 15.5 nJ seed pulse energy and 100 W taper pumping as a function of the stretcher's second order dispersion tuning.*

would like to determine if reduced or increased dispersion in the stretcher can alleviate the problems with nonlinear phase at full power operation.

The results from varying the stretcher's second order dispersion are shown in fig. 4.30. The output pulse's peak power varies only weakly with β_2, and the relation is an unsurprising one: adding more positive dispersion leads to a higher peak power. Added positive second order dispersion means simply stretching the pulse more and reducing nonlinearity in the amplifiers, but the effect is weak with the additional dispersion being only about 5 % of the stretcher's overall dispersion. The increase in peak power with larger stretching also indicates that the compressor can easily compensate for the additional second order dispersion, and fine tuning the stretcher's β_2 cannot alleviate the problem with nonlinear phase. The resulting optimal pulse with the maximum 3.5 ps^2 second order dispersion setting is shown in fig. 4.31. The peak power has risen a little to 29.9 MW but the pulse shape is still almost identical to the case without stretcher tuning in fig. 4.28.

This tuning test shows that compensating for second order dispersion does not constitute a problem for the CPA system. That being the expected result, the test also contributes to validating that the simulations describe the laser system in a sensible way. When building the laser system in reality, the β_2 tunability will be a real boon by compensating for small errors in the compressor optimization, which is trickier to do in practice than in simulations.

With the stretcher's β_2 fixed at its maximum value (giving the highest peak power), the next task is to optimize the third order dispersion. The outcome of this test is less clear but it makes sense to expect the previously presented pulses to contain some uncompensated third order dispersion component. In fact, this can be shown to be the case by

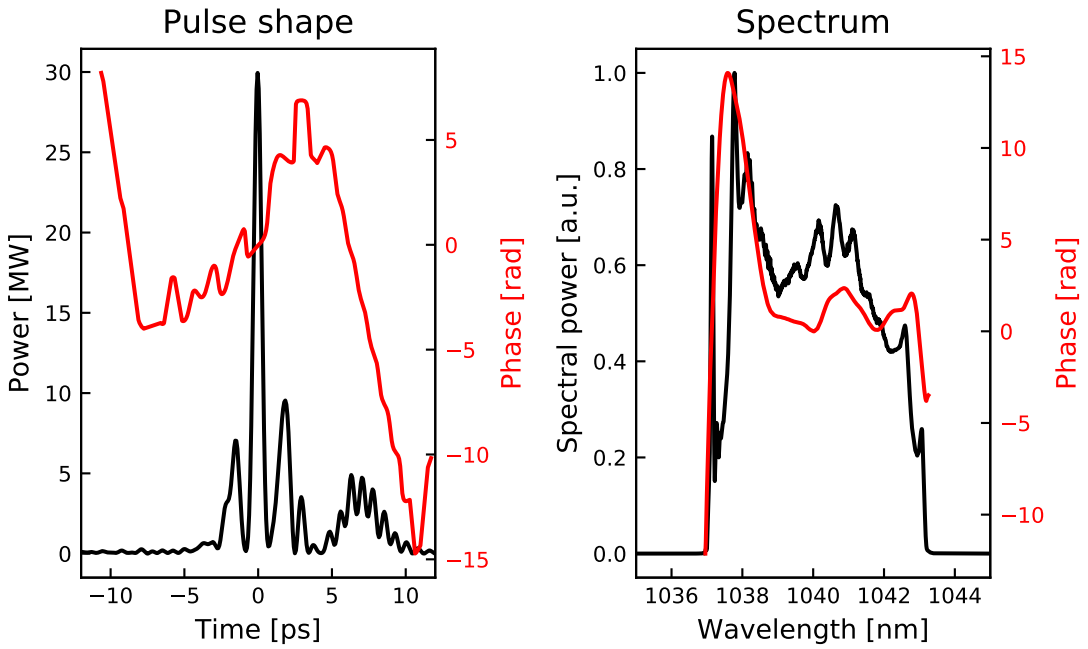

Figure 4.31. *The simulated pulse after the compressor with 15.5 nJ seed energy, 100 W taper pumping and 3.5 ps^2 additional stretcher dispersion.*

fitting a polynomial to the spectral phase curve, but the details of those calculations have been omitted for simplicity and the results of the tuning simulations are presented directly in fig. 4.32.

The relationship between peak power and dispersion tuning resembles again linear but the peak power changes more rapidly than in the β_2 optimization. Clearly, the additional negative third order dispersion in the stretcher better pre-compensates for the positive third order dispersion in the fibers and the compressor (and possibly partly for the SPM phase), leading to higher peak powers after compression. Since third order dispersion has a subtler effect than second order dispersion, which stretches the pulse in proportion to the applied dispersion, one would expect to find an optimal β_3 value after which additional negative β_3 would reduce peak power. The stretcher's tuning range considered here does not appear to extend far enough to reach that optimum. When building the CPA system in the real world, it is worth considering if additional negative β_3 can be introduced somehow.

The optimal pulse after tuning third order dispersion by –0.9 ps^3 is shown in fig. 4.33 and its peak power is 34.0 MW. The pulse's spectrum looks identical to the previous ones, which is unsurprising since fine-tuning should not affect it significantly. However, the sharp peak in the spectral phase has now been compensated and the compressed pulse shape has more of its power in the main peak than before.

Despite the sizeable improvement, this result is far from satisfactory and would remain so even with more negative β_3 due to the complex shape of the nonlinear phase. When running this laser system in practice, the power amplifier's pump diode should be run

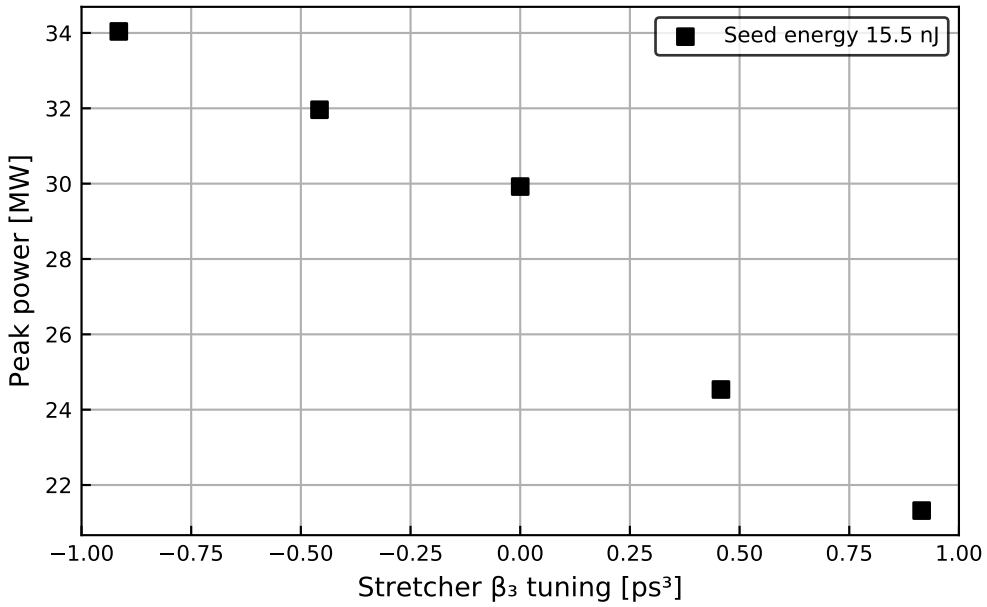

Figure 4.32. *Output peak power at 15.5 nJ seed pulse energy, 100 W taper pumping and 3.5 ps^2 additional stretcher dispersion as a function of the stretcher's third order dispersion tuning.*

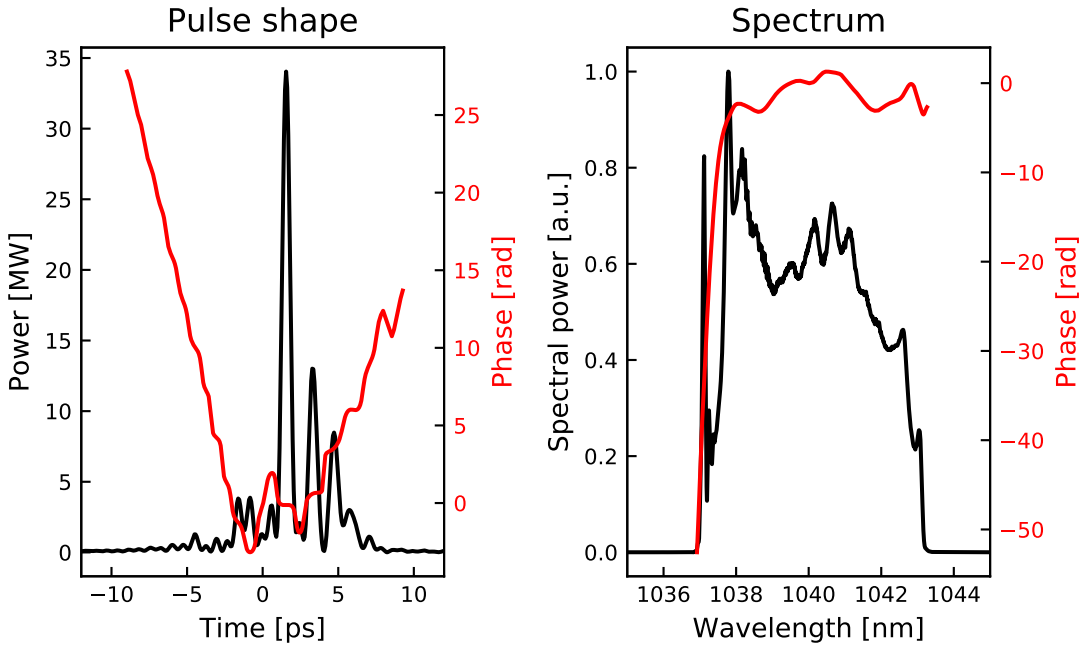

Figure 4.33. *The simulated pulse after the compressor with 15.5 nJ seed energy, 100 W taper pumping and 3.5 ps^2, −0.9 ps^3 stretcher second and third order dispersion tuning.*

at clearly below 100 W to avoid side pulses. Based on the pump tuning results, 60 W pump power might be about the maximum, which would mean an output pulse energy of only about 30 µJ after the compressor's losses. More drastic changes could be made as well, including changing the tapered fiber to another one with better absorption and shorter length, which would reduce the nonlinear phase accumulated by the pulse by some degree. However, based on the fact that the nonlinear phase follows the pulse shape which, coming from the experimental seed laser, is rather irregular, it makes sense to consider whether a more symmetric pulse would tolerate a similar or larger nonlinear phase shift while remaining compressible.

4.2.3 Gaussian seed pulse

This section investigates the effect of using an idealized seed laser in the CPA system instead of the experimental one with an irregular spectrum. Specifically, the seed pulse is assumed to have a Gaussian shape with the same 5.4 nm spectral FWHM as the original seed pulse. Starting with a transform-limited Gaussian, the simulation then adds the same initial chirp that was added to the original seed pulse as mentioned in fig. 4.2 and sets the pulse energy at the same value. The equal spectral widths ensure that the pulses have similar durations after stretching and receive similar amplification in the fiber amplifiers. The Gaussian pulse has more spectral power outside its FWHM than the experimental seed pulse and is consequently stretched slightly more but all in all the main difference between the two seeds is only the spectral shape.

The Gaussian pulse was then propagated numerically through the exact same CPA system whose fiber lengths were those optimized for the original seed pulse. Figure 4.34 shows the results of a set of simulations with 200 mW pumping in the second preamplifier, 20 - 100 W pumping in the tapered power amplifier and zero tuning at the stretcher. Figure 4.34 is therefore directly comparable to the lower seed power data in fig. 4.27.

Where before the growth in the compressed pulse's peak power stalled at 60 W pump power, the Gaussian seed laser allows the peak power to increase linearly in proportion to the average power in the whole simulation range of pump powers, reaching 103 MW peak power and 52 µJ pulse energy at 100 W pumping. This is a clear indication that the seed's spectral shape has a major effect in the designed CPA system and, specifically, that a smooth, regular spectral shape is superior to an irregular one.

The temporal FWHM of the highest energy pulse, shown in fig. 4.35, is 480 fs. The pulse's time-bandwidth product is approx. 1.5 times the theoretical value for a transform-limited Gaussian so the compression, while not perfect, is vastly improved from the results with the experimental seed. The absence of notable side pulses confirms that increased pump power directly raises the generated peak power, and the calculated pulse width matches the time window that contains most of the pulse's energy. The spectral amplitudes in fig. 4.35 show no clear distortion by SPM yet. The figure does show, however, that the spectrum is not a perfect Gaussian since its edges were clipped at the stretcher. This ad-

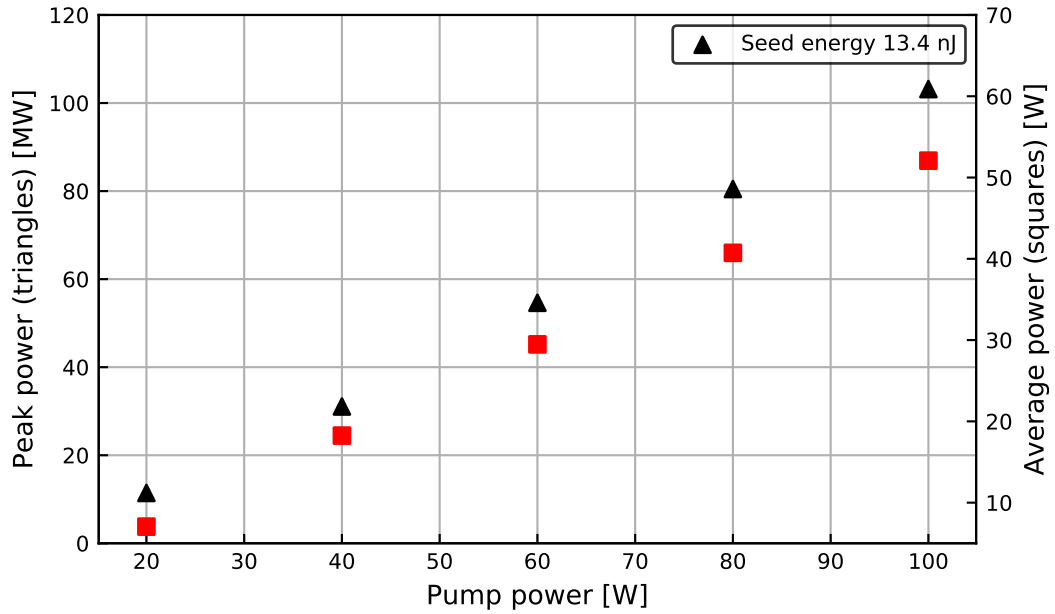

Figure 4.34. *Output average powers (squares) and peak powers (triangles) as a function of pump power in the power amplifier using a Gaussian seed pulse.*

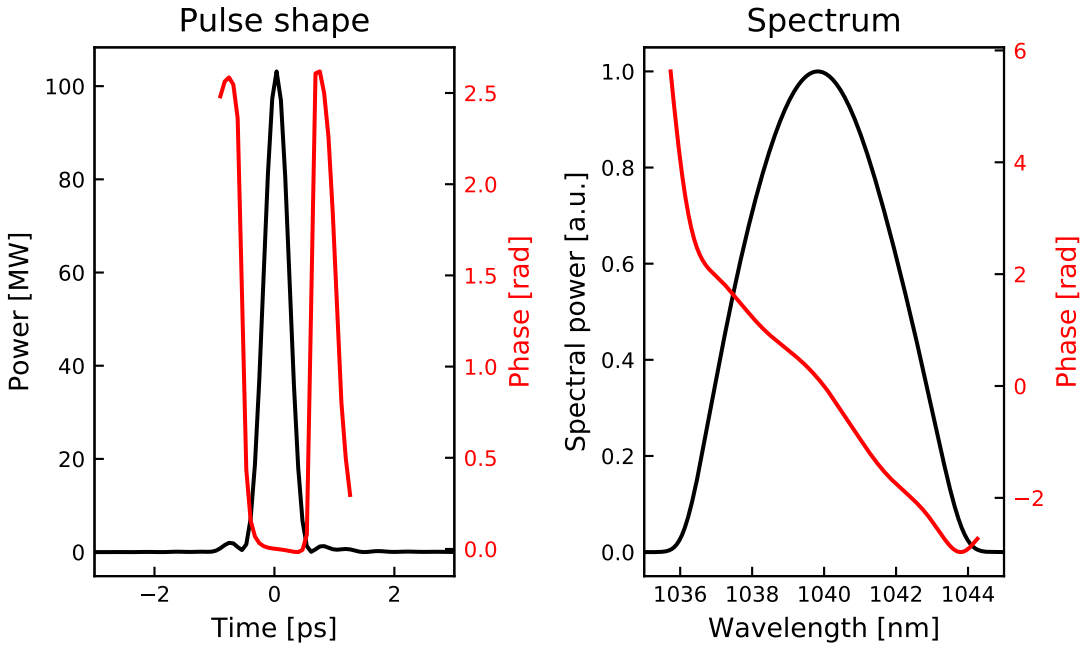

Figure 4.35. *The optimally compressed pulse with 13.4 nJ seed energy from a Gaussian seed followed with preamplifiers and 100 W taper pumping. Note that the time window is much narrower than in the previous comparable figures.*

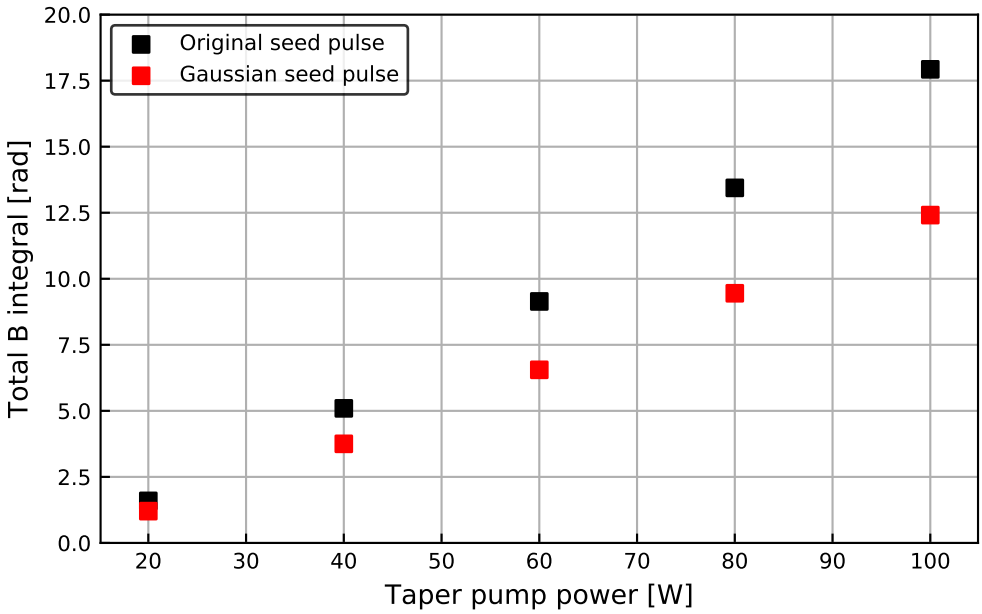

Figure 4.36. *The total B-integral accumulated in the CPA system when using the original experimental seed and the ideal Gaussian seed. The second preamplifier was pumped at 200 mW and the tapered amplifier's pump power was varied.*

ditional loss means that seed pulse energy going into the tapered fiber is 13.4 nJ, slightly lower than the original seed could generate without spectral clipping. However, section 4.2.1 already established that minor variations in seed power have very limited effect on the slope efficiency and the output parameters. The Gaussian pulse's uncompensated residual spectral phase has a much smoother shape and is smaller in magnitude compared to, for example, fig. 4.30, and therefore stretcher tuning might allow some further improvement in compression efficiency, but that is left out of consideration for simplicity.

In addition to accumulating a smoother, easier to compensate nonlinear phase profile than the original pulse, the Gaussian pulse also benefits from a lower total nonlinearity. The reason for this is that the Gaussian pulse's power is more evenly distributed in time domain after stretching, so its peak power remains always lower at any point in the amplifier chain compared to the irregularly shaped pulses. The difference is quantified in fig. 4.36, which shows how the accumulated B-integral grows for both the original pulse and the Gaussian pulse in the CPA system as the tapered amplifier's pump power is raised. The figure includes the contributions of the second preamplifier, which is constant with pump power fixed at 200 mW, and the taper whose contribution varies with pumping. The Gaussian pulse always experiences an overall lower B-integral and the B-integral's rate of growth is also less rapid than for the original seed pulse. The absolute B-integral difference between the different seed reaches 5.5 rad at 100 W pump power where the Gaussian pulse accumulates a B-integral of 12.4 rad and the original seed pulse 17.9 rad.

In total, the simulations with the Gaussian seed pulse implicate the original seed laser as the main limiting factor in the CPA system design. Switching to a seed laser resembling the Gaussian seed would allow generating $>$50 µJ sub-picosecond pulses with minimal

distortion and changing seeds would be much more practical than drastically increasing the stretched pulse duration or the effective mode area in the tapered amplifier.

5 CONCLUSION

In summary, this thesis has demonstrated three main results. The first notable result is the experimentally built and optimized SESAM mode-locked PM fiber laser at 1040 nm. Second, a numerical model was developed for simulating ultrashort pulse propagation in active and passive fibers, fiber-coupled components and especially in tapered double-clad active fiber. Third, this thesis has described a high-power chirped pulse amplification system design based on a fiber Bragg grating stretcher, a tapered fiber power amplifier and a diffraction grating compressor.

While the seed laser's operation originally seemed adequate in terms of spectral width and center wavelength, numerically simulating the whole CPA system revealed that the seed pulses' irregular spectral shape is incompatible with stretching followed by self-phase modulation in the CPA system because the stretched pulse shape mirrors the spectral shape and accumulates irregular nonlinear phase that cannot be compensated by the compressor. Therefore, the seed laser must be improved further before actually building the rest of the CPA setup experimentally. If the future seed is still based on SESAM mode-locking and fiber-based Lyot filtering, also the packaging of those components must be carefully considered to ensure stable operation.

On the more positive side, the experimental seed's output power was found to be easily sufficient for the two-preamplifier design, with even the elimination of one preamplifier being a realistic prospect. Many ultrafast fiber lasers operate around 1030 nm but, in this scheme, the seed wavelength was consciously chosen to be longer at 1040 nm to better match the tapered amplifier's gain maximum based on practical experience. The simulations justify this decision since even the chosen 1040 nm seed spectrum suffered from gain narrowing in the tapered amplifier. A 1030 nm seed spectrum would have narrowed severely causing the stretched pulse to shorten with an accompanying rise in B-integral.

Fortunately for the chosen seed wavelength, opposite side gain narrowing in the power amplifier and the preamplifiers balanced each other out resulting in an output spectrum that was rather close to the seed spectrum except for the SPM-induced ripples. This, however, was a coincidence instead of a conscious design choice. Therefore, the numerical model has exposed both a potential problem but also its potential solution at the same time. In the future, especially if a seed with a broader bandwidth will be used in the real CPA system, gain narrowing compensation using suitable preamplifiers must be considered at the design stage along with the option to move to an even longer wave-

length of perhaps 1045 nm to 1050 nm, where the taper's gain is both higher and flatter with respect to wavelength.

The modelling presented in this thesis included two almost separate parts, the rate equation model for amplification in active fibers and the generalized Schrödinger equation model for ultrafast pulse propagation. The rate equation modelling software, except for the parts related to tapered fibers, has been made available online as the open source Python library PyFiberAmp [72], which has already attracted several users from around the world who have been able to benefit from the work presented here.

A few limitations of the rate equation model became evident during this study, specifically, in the context of tapered fiber amplifier modelling. First, the simple rate equation model exaggerates multimode pump absorption in the tapered fiber, which should be handled more accurately by using a field-based approach, such as the beam propagation method [73]. The current simplified model also fails to take into account the numerical aperture of the launched pump beam and its effect on vignetting. A second major improvement would be to include multimode ASE generated at the thick end of the taper in the model, but this requires implementing a mode solver first to calculate the possible guided ASE modes. Additionally, the reliability of the modelling results would be improved by measuring exact gain and absorption spectra for the tapered fiber's core material for use in the simulations.

The GNLSE ultrafast pulse modelling algorithm was directly based on existing Matlab code from [42] and only had to be translated into Python and extended with tapered active fiber handling capability. The algorithm is rather complete for its originally intended application of supercontinuum simulation and covers physical effects that were not significant for the CPA system in this thesis, such as self-steepening and stimulated Raman scattering. At the same time, the algorithm has deficiencies related to modelling fiber amplifiers. Especially relevant would be to add proper noise simulation, including ASE noise and spontaneous Raman scattering, which would then seed SRS, in order to find the SRS threshold of any simulated tapered fiber amplifier. The code's execution speed also requires optimization to enable efficient exploration of different parameters of the CPA system in a reasonable time. Lastly, the rate equation and ultrafast models should be integrated more tightly, like done in [74, 75] to account for situations where gain saturation or nonlinear spectral broadening play a role. The improved software might be added to PyFiberAmp in the future.

The CPA system design itself was demonstrated to work reasonably well with the main obstacle being the experimental seed laser. With Gaussian seed pulses, the simulations predicted that at least 52 µJ, 480 fs output pulses should be possible with this design with 1 MHz repetition rate meaning 52 W average output power. Based on experiments with higher average power tapered fiber amplifiers, the repetition rate could be multiplied to yield 100 to 200 W of average output power without major changes to the design. The second preamplifier should simply be made more powerful to reach an equivalently higher seed power going into the power amplifier.

In terms of nonlinearity, the preamplifier chain generated only negligible nonlinear phase shift with the single-mode LMA fiber used in the second preamplifier, so basically all the harmful nonlinearity was accumulated in the taper. An older generation tapered fiber was used in the simulations because of existing experimental data for that taper. However, newer generation tapers are shorter and have better longitudinal profiles, which should reduce B-integral compared to the obtained results. The stretcher's tunability was also found to be of modest help for improving pulse compression, though its main purpose in the experimental work will be to counteract imprecise alignment of the compressor. Furthermore, when finalizing this thesis, I became aware of a recent paper [76], which reports a lower value for the nonlinear refractive index than was used in the simulations, $2.19 \cdot 10^{-20}\,\mathrm{m^2\,W^{-1}}$ at 1030 nm compared to $2.5 \cdot 10^{-20}\,\mathrm{m^2\,W^{-1}}$ at 1040 nm. Therefore, it is possible that the numerical model slightly overestimated the nonlinear phase shift accumulated in the tapered fiber.

The results of this thesis can guide future work on the CPA system in several ways. Most importantly, they show that the seed laser must be sent back to the drawing board with the aim of generating a smoother spectral shape that is better compressible after experiencing SPM. Second, gain narrowing should be considered more carefully, especially if the new seed's center wavelength or spectral width will be different. Meanwhile, the numerical model can be used to experiment with alternative stretched pulse durations and repetition rates to optimize the design further. In return, building the CPA system in the laboratory will enable direct comparison between the simulation and the experiment allowing the model to be refined to better match the real world.

REFERENCES

[1] Sugioka, K. and Cheng, Y. Ultrafast lasers—reliable tools for advanced materials processing. en. *Light: Science & Applications* 3.4 (Apr. 2014). Number: 4 Publisher: Nature Publishing Group, e149–e149. ISSN: 2047-7538. DOI: 10.1038/lsa.2014.30. URL: https://www.nature.com/articles/lsa201430 (visited on 04/07/2020).

[2] Eden, J. G. High-order harmonic generation and other intense optical field–matter interactions: review of recent experimental and theoretical advances. en. *Progress in Quantum Electronics* 28.3 (Jan. 2004), 197–246. ISSN: 0079-6727. DOI: 10.1016/j.pquantelec.2004.06.002. URL: http://www.sciencedirect.com/science/article/pii/S0079672704000187 (visited on 04/07/2020).

[3] Krausz, F. and Ivanov, M. Attosecond physics. *Reviews of Modern Physics* 81.1 (Feb. 2009). Publisher: American Physical Society, 163–234. DOI: 10.1103/RevModPhys.81.163. URL: https://link.aps.org/doi/10.1103/RevModPhys.81.163 (visited on 04/07/2020).

[4] Strickland, D. and Mourou, G. Compression of amplified chirped optical pulses. en. *Optics Communications* 56.3 (Dec. 1985), 219–221. ISSN: 0030-4018. DOI: 10.1016/0030-4018(85)90120-8. URL: http://www.sciencedirect.com/science/article/pii/0030401885901208 (visited on 03/28/2020).

[5] Klenke, A., Seise, E., Demmler, S., Rothhardt, J., Breitkopf, S., Limpert, J. and Tünnermann, A. Coherently-combined two channel femtosecond fiber CPA system producing 3 mJ pulse energy. EN. *Optics Express* 19.24 (Nov. 2011), 24280–24285. ISSN: 1094-4087. DOI: 10.1364/OE.19.024280. URL: https://www.osapublishing.org/oe/abstract.cfm?uri=oe-19-24-24280 (visited on 09/11/2018).

[6] Zhou, S., Wise, F. W. and Ouzounov, D. G. Divided-pulse amplification of ultrashort pulses. EN. *Optics Letters* 32.7 (Apr. 2007). Publisher: Optical Society of America, 871–873. ISSN: 1539-4794. DOI: 10.1364/OL.32.000871. URL: https://www.osapublishing.org/ol/abstract.cfm?uri=ol-32-7-871 (visited on 04/07/2020).

[7] Weck, A., Crawford, T., Wilkinson, D., Haugen, H. and Preston, J. Laser drilling of high aspect ratio holes in copper with femtosecond, picosecond and nanosecond pulses. en. *Applied Physics A* 90.3 (Mar. 2008), 537–543. ISSN: 0947-8396, 1432-0630. DOI: 10.1007/s00339-007-4300-6. URL: http://link.springer.com/10.1007/s00339-007-4300-6 (visited on 04/07/2020).

[8] Shah, L. and Fermann, M. High-Power Ultrashort-Pulse Fiber Amplifiers. en. *IEEE Journal of Selected Topics in Quantum Electronics* 13.3 (2007), 552–558. ISSN: 1077-260X. DOI: 10.1109/JSTQE.2007.896096. URL: http://ieeexplore.ieee.org/document/4244456/ (visited on 09/27/2018).

[9] Richardson, D. J., Nilsson, J. and Clarkson, W. A. High power fiber lasers: current status and future perspectives [Invited]. en. *Journal of the Optical Society of America B* 27.11 (Nov. 2010), B63. ISSN: 0740-3224, 1520-8540. DOI: 10.1364/JOSAB.27.000B63. URL: https://www.osapublishing.org/abstract.cfm?URI=josab-27-11-B63 (visited on 07/09/2019).

[10] Koplow, J. P., Kliner, D. A. V. and Goldberg, L. Single-mode operation of a coiled multimode fiber amplifier. en. *Optics Letters* 25.7 (Apr. 2000), 442. ISSN: 0146-9592, 1539-4794. DOI: 10.1364/OL.25.000442. URL: https://www.osapublishing.org/abstract.cfm?URI=ol-25-7-442 (visited on 03/26/2020).

[11] Fermann, M. E. Single-mode excitation of multimode fibers with ultrashort pulses. en. *Optics Letters* 23.1 (Jan. 1998), 52. ISSN: 0146-9592, 1539-4794. DOI: 10.1364/OL.23.000052. URL: https://www.osapublishing.org/abstract.cfm?URI=ol-23-1-52 (visited on 11/03/2018).

[12] Ma, X., Liu, C.-H., Chang, G. and Galvanauskas, A. Angular-momentum coupled optical waves in chirally-coupled-core fibers. en. *Optics Express* 19.27 (Dec. 2011), 26515. ISSN: 1094-4087. DOI: 10.1364/OE.19.026515. URL: https://www.osapublishing.org/oe/abstract.cfm?uri=oe-19-27-26515 (visited on 03/26/2020).

[13] Ma, X., Zhu, C., Hu, I.-N., Kaplan, A. and Galvanauskas, A. Single-mode chirally-coupled-core fibers with larger than 50µm diameter cores. en. *Optics Express* 22.8 (Apr. 2014), 9206. ISSN: 1094-4087. DOI: 10.1364/OE.22.009206. URL: https://www.osapublishing.org/abstract.cfm?URI=oe-22-8-9206 (visited on 03/26/2020).

[14] Limpert, J., Liem, A., Reich, M., Schreiber, T., Nolte, S., Zellmer, H., Tnnermann, A., Broeng, J., Petersson, A. and Jakobsen, C. Low-nonlinearity single-transverse-mode ytterbium-doped photonic crystal fiber amplifier. en. *Optics Express* 12.7 (2004), 1313. ISSN: 1094-4087. DOI: 10.1364/OPEX.12.001313. URL: https://www.osapublishing.org/oe/abstract.cfm?uri=oe-12-7-1313 (visited on 03/26/2020).

[15] Limpert, J., Stutzki, F., Jansen, F., Otto, H.-J., Eidam, T., Jauregui, C. and Tünnermann, A. Yb-doped large-pitch fibres: effective single-mode operation based on higher-order mode delocalisation. en. *Light: Science & Applications* 1.4 (Apr. 2012), e8–e8. ISSN: 2047-7538. DOI: 10.1038/lsa.2012.8. URL: http://www.nature.com/articles/lsa20128 (visited on 03/26/2020).

[16] Želudevičius, J., Danilevičius, R., Viskontas, K., Rusteika, N. and Regelskis, K. Femtosecond fiber CPA system based on picosecond master oscillator and power amplifier with CCC fiber. EN. *Optics Express* 21.5 (Mar. 2013), 5338–5345. ISSN: 1094-4087. DOI: 10.1364/OE.21.005338. URL: https://www.osapublishing.org/oe/abstract.cfm?uri=oe-21-5-5338 (visited on 09/11/2018).

[17] Wan, P., Yang, L.-M. and Liu, J. All fiber-based Yb-doped high energy, high power femtosecond fiber lasers. en. *Optics Express* 21.24 (Dec. 2013), 29854. ISSN:

1094-4087. DOI: 10.1364/OE.21.029854. URL: https://www.osapublishing.org/oe/abstract.cfm?uri=oe-21-24-29854 (visited on 03/28/2020).

[18] Eidam, T., Hanf, S., Seise, E., Andersen, T. V., Gabler, T., Wirth, C., Schreiber, T., Limpert, J. and Tünnermann, A. Femtosecond fiber CPA system emitting 830 W average output power. EN. *Optics Letters* 35.2 (Jan. 2010), 94–96. ISSN: 1539-4794. DOI: 10.1364/OL.35.000094. URL: https://www.osapublishing.org/ol/abstract.cfm?uri=ol-35-2-94 (visited on 09/11/2018).

[19] Eidam, T., Rothhardt, J., Stutzki, F., Jansen, F., Hädrich, S., Carstens, H., Jauregui, C., Limpert, J. and Tünnermann, A. Fiber chirped-pulse amplification system emitting 38 GW peak power. en. *Optics Express* 19.1 (Jan. 2011), 255. ISSN: 1094-4087. DOI: 10.1364/OE.19.000255. URL: https://www.osapublishing.org/oe/abstract.cfm?uri=oe-19-1-255 (visited on 09/27/2018).

[20] Filippov, V., Chamorovskii, Y., Kerttula, J., Golant, K., Pessa, M. and Okhotnikov, O. G. Double clad tapered fiber for high power applications. en. *Optics Express* 16.3 (2008), 1929. ISSN: 1094-4087. DOI: 10.1364/OE.16.001929. URL: https://www.osapublishing.org/oe/abstract.cfm?uri=oe-16-3-1929 (visited on 03/28/2020).

[21] Rashleigh, S. Origins and control of polarization effects in single-mode fibers. *Journal of Lightwave Technology* 1.2 (June 1983). Conference Name: Journal of Lightwave Technology, 312–331. ISSN: 1558-2213. DOI: 10.1109/JLT.1983.1072121.

[22] Gloge, D. Weakly Guiding Fibers. en. *Applied Optics* 10.10 (Oct. 1971), 2252. ISSN: 0003-6935, 1539-4522. DOI: 10.1364/AO.10.002252. URL: https://www.osapublishing.org/abstract.cfm?URI=ao-10-10-2252 (visited on 10/06/2018).

[23] Agrawal, G. P. *Nonlinear fiber optics*. 4th ed. Quantum electronics–principles and applications. Amsterdam ; Boston: Elsevier / Academic Press, 2007. ISBN: 978-0-12-369516-1.

[24] Zervas, M. N. and Codemard, C. A. High Power Fiber Lasers: A Review. en. *IEEE Journal of Selected Topics in Quantum Electronics* 20.5 (Sept. 2014), 219–241. ISSN: 1077-260X, 1558-4542. DOI: 10.1109/JSTQE.2014.2321279. URL: http://ieeexplore.ieee.org/document/6808413/ (visited on 04/09/2020).

[25] Urquhart, P. Review of rare earth doped fibre lasers and amplifiers. en. *IEE Proceedings J Optoelectronics* 135.6 (1988), 385. ISSN: 02673932. DOI: 10.1049/ip-j.1988.0071. URL: https://digital-library.theiet.org/content/journals/10.1049/ip-j.1988.0071 (visited on 04/10/2020).

[26] Digonnet, M. J. F. *Rare-Earth-Doped Fiber Lasers and Amplifiers, Revised and Expanded*. en. CRC Press, May 2001. ISBN: 978-0-8247-4164-8.

[27] Pask, H. M., Carman, R. J., Hanna, D. C., Tropper, A. C., Mackechnie, C. J., Barber, P. R. and Dawes, J. M. Ytterbium-Doped Silica Fiber Lasers: Versatile Sources for the 1-1.2 pm Region. en. *IEEE Journal of Selected Topics in Quantum Electronics* (1995), 12.

[28] *Nufern website*. Mar. 11, 2019. URL: https://www.nufern.com/.

[29] Giles, C. and Desurvire, E. Modeling erbium-doped fiber amplifiers. en. *Journal of Lightwave Technology* 9.2 (Feb. 1991), 271–283. ISSN: 07338724. DOI: 10.1109/50.65886. URL: http://ieeexplore.ieee.org/document/65886/ (visited on 10/06/2018).

[30] Trebino, R. *Frequency-resolved optical gating: the measurement of ultrashort laser pulses*. eng. New York: Springer Science + Business Media, 2000. ISBN: 978-1-4613-5432-1.

[31] Jauregui, C., Limpert, J. and Tünnermann, A. Derivation of Raman threshold formulas for CW double-clad fiber amplifiers. en. (2009), 15.

[32] Schimpf, D. N., Eidam, T., Seise, E., Hädrich, S., Limpert, J. and Tünnermann, A. Circular versus linear polarization in laser-amplifiers with Kerr-nonlinearity. en. *Optics Express* 17.21 (Oct. 2009), 18774. ISSN: 1094-4087. DOI: 10.1364/OE.17.018774. URL: https://www.osapublishing.org/oe/abstract.cfm?uri=oe-17-21-18774 (visited on 10/20/2019).

[33] Stolen, R. Polarization effects in fiber Raman and Brillouin lasers. en. *IEEE Journal of Quantum Electronics* 15.10 (Oct. 1979), 1157–1160. ISSN: 0018-9197. DOI: 10.1109/JQE.1979.1069913. URL: http://ieeexplore.ieee.org/document/1069913/ (visited on 04/10/2020).

[34] Farrow, R. L., Kliner, D. A. V., Hadley, G. R. and Smith, A. V. Peak-power limits on fiber amplifiers imposed by self-focusing. en. *Optics Letters* 31.23 (Dec. 2006), 3423. ISSN: 0146-9592, 1539-4794. DOI: 10.1364/OL.31.003423. URL: https://www.osapublishing.org/abstract.cfm?URI=ol-31-23-3423 (visited on 03/31/2020).

[35] Backus, S., Durfee, C. G., Murnane, M. M. and Kapteyn, H. C. High power ultrafast lasers. en. *Review of Scientific Instruments* 69.3 (Mar. 1998), 1207–1223. ISSN: 0034-6748, 1089-7623. DOI: 10.1063/1.1148795. URL: http://aip.scitation.org/doi/10.1063/1.1148795 (visited on 09/27/2018).

[36] Zhou, S., Kuznetsova, L., Chong, A. and Wise, F. W. Compensation of nonlinear phase shifts with third-order dispersion in short-pulse fiber amplifiers. en. *Optics Express* 13.13 (2005), 4869. ISSN: 1094-4087. DOI: 10.1364/OPEX.13.004869. URL: https://www.osapublishing.org/oe/abstract.cfm?uri=oe-13-13-4869 (visited on 09/30/2018).

[37] Ilday, F. Ö., Buckley, J. R., Clark, W. G. and Wise, F. W. Self-Similar Evolution of Parabolic Pulses in a Laser. en. *Physical Review Letters* 92.21 (May 2004), 213902. ISSN: 0031-9007, 1079-7114. DOI: 10.1103/PhysRevLett.92.213902. URL: https://link.aps.org/doi/10.1103/PhysRevLett.92.213902 (visited on 07/09/2019).

[38] Hult, J. A Fourth-Order Runge–Kutta in the Interaction Picture Method for Simulating Supercontinuum Generation in Optical Fibers. en. *Journal of Lightwave Technology* 25.12 (Dec. 2007), 3770–3775. ISSN: 0733-8724. DOI: 10.1109/JLT.2007.909373. URL: http://ieeexplore.ieee.org/document/4397001/ (visited on 07/09/2019).

[39] Heidt, A. Efficient Adaptive Step Size Method for the Simulation of Supercontinuum Generation in Optical Fibers. en. *Journal of Lightwave Technology* 27.18 (Sept. 2009), 3984–3991. ISSN: 0733-8724, 1558-2213. DOI: 10.1109/JLT.2009.2021538. URL: http://ieeexplore.ieee.org/document/4907035/ (visited on 07/10/2019).

[40] Sinkin, O., Holzlohner, R., Zweck, J. and Menyuk, C. Optimization of the split-step fourier method in modeling optical-fiber communications systems. en. *Journal of Lightwave Technology* 21.1 (Jan. 2003), 61–68. ISSN: 0733-8724. DOI: 10.1109/JLT.2003.808628. URL: http://ieeexplore.ieee.org/document/1190149/ (visited on 09/27/2018).

[41] Rieznik, A. A., Heidt, A. M., Konig, P. G., Bettachini, V. A. and Grosz, D. F. Optimum Integration Procedures for Supercontinuum Simulation. en. *IEEE Photonics Journal* 4.2 (Apr. 2012), 552–560. ISSN: 1943-0655. DOI: 10.1109/JPHOT.2012.2188281. URL: http://ieeexplore.ieee.org/document/6153336/ (visited on 07/18/2019).

[42] *Free Optics Project*. Mar. 29, 2020. URL: https://www.freeopticsproject.org.

[43] Hanna, M., Papadopoulos, D., Druon, F. and Georges, P. Distributed nonlinear fiber chirped-pulse amplifier system. en. *Optics Express* 17.13 (June 2009), 10835. ISSN: 1094-4087. DOI: 10.1364/OE.17.010835. URL: https://www.osapublishing.org/oe/abstract.cfm?uri=oe-17-13-10835 (visited on 09/26/2018).

[44] Hill, K. and Meltz, G. Fiber Bragg grating technology fundamentals and overview. en. *Journal of Lightwave Technology* 15.8 (Aug. 1997), 1263–1276. ISSN: 07338724. DOI: 10.1109/50.618320. URL: http://ieeexplore.ieee.org/document/618320/ (visited on 09/23/2018).

[45] Meltz, G., Morey, W. W. and Glenn, W. H. Formation of Bragg gratings in optical fibers by a transverse holographic method. en. *Optics Letters* 14.15 (Aug. 1989), 823. ISSN: 0146-9592, 1539-4794. DOI: 10.1364/OL.14.000823. URL: https://www.osapublishing.org/abstract.cfm?URI=ol-14-15-823 (visited on 04/11/2020).

[46] Martinez, A., Dubov, M., Khrushchev, I. and Bennion, I. Direct writing of fibre Bragg gratings by femtosecond laser. en. *Electronics Letters* 40.19 (2004), 1170. ISSN: 00135194. DOI: 10.1049/el:20046050. URL: https://digital-library.theiet.org/content/journals/10.1049/el_20046050 (visited on 04/11/2020).

[47] Othonos, A. Fiber Bragg gratings. *Review of Scientific Instruments* 68.12 (Dec. 1997). Publisher: American Institute of Physics, 4309–4341. ISSN: 0034-6748. DOI: 10.1063/1.1148392. URL: https://aip.scitation.org/doi/10.1063/1.1148392 (visited on 04/11/2020).

[48] Imeshev, G., Hartl, I. and Fermann, M. E. Chirped pulse amplification with a nonlinearly chirped fiber Bragg grating matched to the Treacy compressor. en. *Optics Letters* 29.7 (Apr. 2004), 679. ISSN: 0146-9592, 1539-4794. DOI: 10.1364/OL.29.000679. URL: https://www.osapublishing.org/abstract.cfm?URI=ol-29-7-679 (visited on 04/11/2020).

[49] Liao, K.-H., Cheng, M.-Y., Flecher, E., Smirnov, V. I., Glebov, L. B. and Galvanauskas, A. Large-aperture chirped volume Bragg grating based fiber CPA system. EN. *Optics Express* 15.8 (Apr. 2007), 4876–4882. ISSN: 1094-4087. DOI: 10.1364/OE.15.004876. URL: https://www.osapublishing.org/oe/abstract.cfm?uri=oe-15-8-4876 (visited on 09/11/2018).

[50] Bartulevicius, T., Frankinas, S., Michailovas, A., Vasilyeu, R., Smirnov, V., Trepanier, F. and Rusteika, N. Compact fiber CPA system based on a CFBG stretcher and CVBG compressor with matched dispersion profile. en. *Optics Express* 25.17 (Aug. 2017), 19856. ISSN: 1094-4087. DOI: 10.1364/OE.25.019856. URL: https://www.osapublishing.org/abstract.cfm?URI=oe-25-17-19856 (visited on 10/20/2019).

[51] Glebov, L., Smirnov, V., Rotari, E., Cohanoschi, I., Glebova, L., Smolski, O., Lumeau, J., Lantigua, C. and Glebov, A. Volume-chirped Bragg gratings: monolithic components for stretching and compression of ultrashort laser pulses. en. *Optical Engineering* 53.5 (Feb. 2014), 051514. ISSN: 0091-3286. DOI: 10.1117/1.OE.53.5.051514. URL: http://opticalengineering.spiedigitallibrary.org/article.aspx?doi=10.1117/1.OE.53.5.051514 (visited on 09/26/2018).

[52] *Thorlabs Diffraction Grating Tutorial*. Apr. 11, 2020. URL: https://www.thorlabs.com/newgrouppage9.cfm?objectgroup_id=9026.

[53] Palmer, C. and Loewen, E. *Diffraction Grating Handbook*. 6th edition. Newport Corporation, 2005.

[54] Buchwald, K. *Fused Silica Transmission Gratings*. en. 2007. URL: https://ibsen.com/wp-content/uploads/White-paper-Fused-Silica-Transmission-Gratings-v1.0.pdf.

[55] Treacy, E. Optical pulse compression with diffraction gratings. *IEEE Journal of Quantum Electronics* 5.9 (Sept. 1969), 454–458. ISSN: 0018-9197. DOI: 10.1109/JQE.1969.1076303.

[56] Johnson, A. M., Stolen, R. H. and Simpson, W. M. 80× single-stage compression of frequency doubled Nd:yttrium aluminum garnet laser pulses. en. *Applied Physics Letters* 44.8 (Apr. 1984), 729–731. ISSN: 0003-6951, 1077-3118. DOI: 10.1063/1.94897. URL: http://aip.scitation.org/doi/10.1063/1.94897 (visited on 03/26/2020).

[57] Martinez, O. 3000 times grating compressor with positive group velocity dispersion: Application to fiber compensation in 1.3-1.6 μm region. *IEEE Journal of Quantum Electronics* 23.1 (Jan. 1987). Conference Name: IEEE Journal of Quantum Electronics, 59–64. ISSN: 1558-1713. DOI: 10.1109/JQE.1987.1073201.

[58] Cheriaux, G., Walker, B., Dimauro, L. F., Rousseau, P., Salin, F. and Chambaret, J. P. Aberration-free stretcher design for ultrashort-pulse amplification. en. *Optics Letters* 21.6 (Mar. 1996), 414. ISSN: 0146-9592, 1539-4794. DOI: 10.1364/OL.21.000414. URL: https://www.osapublishing.org/abstract.cfm?URI=ol-21-6-414 (visited on 09/27/2018).

[59] Martinez, O. E., Gordon, J. P. and Fork, R. L. Negative group-velocity dispersion using refraction. en. *Journal of the Optical Society of America A* 1.10 (Oct. 1984),

1003. ISSN: 1084-7529, 1520-8532. DOI: 10.1364/JOSAA.1.001003. URL: https://www.osapublishing.org/abstract.cfm?URI=josaa-1-10-1003 (visited on 02/13/2019).

[60] Kane, S. and Squier, J. Grism-pair stretcher–compressor system for simultaneous second- and third-order dispersion compensation in chirped-pulse amplification. en. *Journal of the Optical Society of America B* 14.3 (Mar. 1997), 661. ISSN: 0740-3224, 1520-8540. DOI: 10.1364/JOSAB.14.000661. URL: https://www.osapublishing.org/abstract.cfm?URI=josab-14-3-661 (visited on 04/11/2020).

[61] Zaouter, Y., Boullet, J., Mottay, E. and Cormier, E. Transform-limited 100 μJ, 340 MW pulses from a nonlinear-fiber chirped-pulse amplifier using a mismatched grating stretcher–compressor. EN. *Optics Letters* 33.13 (July 2008). Publisher: Optical Society of America, 1527–1529. ISSN: 1539-4794. DOI: 10.1364/OL.33.001527. URL: https://www.osapublishing.org/ol/abstract.cfm?uri=ol-33-13-1527 (visited on 04/14/2020).

[62] Chong, A., Buckley, J., Renninger, W. and Wise, F. All-normal-dispersion femtosecond fiber laser. EN. *Optics Express* 14.21 (Oct. 2006). Publisher: Optical Society of America, 10095–10100. ISSN: 1094-4087. DOI: 10.1364/OE.14.010095. URL: https://www.osapublishing.org/oe/abstract.cfm?uri=oe-14-21-10095 (visited on 04/05/2020).

[63] Aguergaray, C., Hawker, R., Runge, A. F. J., Erkintalo, M. and Broderick, N. G. R. 120 fs, 4.2 nJ pulses from an all-normal-dispersion, polarization-maintaining, fiber laser. en. *Applied Physics Letters* 103.12 (Sept. 2013), 121111. ISSN: 0003-6951, 1077-3118. DOI: 10.1063/1.4821776. URL: http://aip.scitation.org/doi/10.1063/1.4821776 (visited on 09/26/2018).

[64] Regelskis, K., Želudevičius, J., Viskontas, K. and Račiukaitis, G. Ytterbium-doped fiber ultrashort pulse generator based on self-phase modulation and alternating spectral filtering. EN. *Optics Letters* 40.22 (Nov. 2015). Publisher: Optical Society of America, 5255–5258. ISSN: 1539-4794. DOI: 10.1364/OL.40.005255. URL: https://www.osapublishing.org/ol/abstract.cfm?uri=ol-40-22-5255 (visited on 04/05/2020).

[65] Lecourt, J.-B., Duterte, C., Narbonneau, F., Kinet, D., Hernandez, Y. and Giannone, D. All-normal dispersion, all-fibered PM laser mode-locked by SESAM. en. *Optics Express* 20.11 (May 2012), 11918. ISSN: 1094-4087. DOI: 10.1364/OE.20.011918. URL: https://www.osapublishing.org/oe/abstract.cfm?uri=oe-20-11-11918 (visited on 09/26/2018).

[66] Grüner-Nielsen, L., Jakobsen, D., Jespersen, K. G. and Pálsdóttir, B. A stretcher fiber for use in fs chirped pulse Yb amplifiers. en. *Optics Express* 18.4 (Feb. 2010), 3768. ISSN: 1094-4087. DOI: 10.1364/OE.18.003768. URL: https://www.osapublishing.org/oe/abstract.cfm?uri=oe-18-4-3768 (visited on 03/15/2020).

[67] Kane, D. and Trebino, R. Characterization of arbitrary femtosecond pulses using frequency-resolved optical gating. en. *IEEE Journal of Quantum Electronics* 29.2

(Feb. 1993), 571–579. ISSN: 00189197. DOI: 10.1109/3.199311. URL: http://ieeexplore.ieee.org/document/199311/ (visited on 04/02/2020).

[68] *Corning PANDA PM Specialty Optical Fibers*. Mar. 29, 2020. URL: https://www.corning.com/media/worldwide/csm/documents/PANDA%20PM%20and%20RC%20PANDA%20Specialty%20Fiber.pdf.

[69] Verhoef, A., Zhu, L., Israelsen, S. M., Grüner-Nielsen, L., Unterhuber, A., Kautek, W., Rottwitt, K., Baltuška, A. and Fernández, A. Sub-100 fs pulses from an all-polarization maintaining Yb-fiber oscillator with an anomalous dispersion higher-order-mode fiber. en. *Optics Express* 23.20 (Oct. 2015), 26139. ISSN: 1094-4087. DOI: 10.1364/OE.23.026139. URL: https://www.osapublishing.org/abstract.cfm?URI=oe-23-20-26139 (visited on 09/27/2018).

[70] Paschotta, R., Nilsson, J., Tropper, A. and Hanna, D. Ytterbium-doped fiber amplifiers. en. *IEEE Journal of Quantum Electronics* 33.7 (July 1997), 1049–1056. ISSN: 00189197. DOI: 10.1109/3.594865. URL: http://ieeexplore.ieee.org/document/594865/ (visited on 10/07/2018).

[71] Kerttula, J., Filippov, V., Chamorovskii, Y., Ustimchik, V., Golant, K. and Okhotnikov, O. G. Principles and performance of tapered fiber lasers: from uniform to flared geometry. en. *Applied Optics* 51.29 (Oct. 2012), 7025. ISSN: 1559-128X, 2155-3165. DOI: 10.1364/AO.51.007025. URL: https://www.osapublishing.org/abstract.cfm?URI=ao-51-29-7025 (visited on 09/26/2018).

[72] *PyFiberAmp*. Mar. 28, 2020. URL: https://github.com/Jomiri/pyfiberamp.

[73] Van Roey, J., Donk, J. van der and Lagasse, P. E. Beam-propagation method: analysis and assessment. en. *Journal of the Optical Society of America* 71.7 (July 1981), 803. ISSN: 0030-3941. DOI: 10.1364/JOSA.71.000803. URL: https://www.osapublishing.org/abstract.cfm?URI=josa-71-7-803 (visited on 04/15/2020).

[74] Lindberg, R., Zeil, P., Malmström, M., Laurell, F. and Pasiskevicius, V. Accurate modeling of high-repetition rate ultrashort pulse amplification in optical fibers. en. *Scientific Reports* 6.1 (Dec. 2016), 34742. ISSN: 2045-2322. DOI: 10.1038/srep34742. URL: http://www.nature.com/articles/srep34742 (visited on 07/09/2019).

[75] Chen, H.-W., Lim, J., Huang, S.-W., Schimpf, D. N., Kärtner, F. X. and Chang, G. Optimization of femtosecond Yb-doped fiber amplifiers for high-quality pulse compression. en. *Optics Express* 20.27 (Dec. 2012), 28672. ISSN: 1094-4087. DOI: 10.1364/OE.20.028672. URL: https://www.osapublishing.org/oe/abstract.cfm?uri=oe-20-27-28672 (visited on 07/09/2019).

[76] Kabaciński, P., Kardaś, T. M., Stepanenko, Y. and Radzewicz, C. Nonlinear refractive index measurement by SPM-induced phase regression. en. *Optics Express* 27.8 (Apr. 2019), 11018. ISSN: 1094-4087. DOI: 10.1364/OE.27.011018. URL: https://www.osapublishing.org/abstract.cfm?URI=oe-27-8-11018 (visited on 03/29/2020).

A GNLSE SIMULATION CODE

Program A.1. *This Python code is an implementation of the fourth order Runge Kutta in the interaction picture method integration algorithm with conserved quantity error method stepper used in this thesis for solving the generalized nonlinear Schrödinger equation. The code has been translated into Python from the original Matlab code available on [42]. Active and tapered fiber handling as well as dense output capability have been added afterwards by the author.*

```
1  import numpy as np
2  from scipy.fftpack import fft, ifft, fftshift
3
4
5  def gnlse_dense_active(Aw, hr, fr, dt,
6                         dense_z, w0, betas,
7                         alpha_func, gamma_func,
8                         dz=1e-7, tol=1e-6):
9      """
10     This function solves the generalized nonlinear Schrödinger
11     equation using the conserved quantity error method with
12     the nonlinear part integrated in frequency domain.
13     Suitable for nonuniform active fibers.
14     Modified to Python from A. Rieznik's Matlab code on
15     http://www.freeopticsproject.org/
16
17     Parameters:
18
19     Aw: Frequency domain amplitudes describing the startin pulse
20         (numpy complex array)
21     hr: time domain Raman response function of the fiber
22         (numpy float array)
23     fr: Raman contribution parameter
24         (float, 0-1)
25     dt: simulation time grid resolution
26         (float)
27     dense_z: positions in the fiber where output is required
28         (sorted float array or list)
```

```
29      w0: carrier angular frequency
30          (float)
31      betas: Taylor coefficiencts of the propagation constant
32             starting form second order dispersion
33             (list of floats)
34      alpha_func: function that takes position z as input
35                  and returns an array containing net gain
36                  at all the spectral bins
37                  (function)
38      gamma_func: function that takes position z as input
39                  and returns an array containing
40                  the nonlinear parameter gamma
41                  at all the spectral bins
42                  (function)
43      dz: initial spatial step size
44          (float)
45      tol: relative local error tolerance
46          (float)
47
48      Returns:
49
50      At: time domain complex amplitudes at locations
51          set by dense_z
52          (numpy complex array)
53      n_it: number of iterations performed
54          (int)
55      """
56
57      N = Aw.size
58      Aw_dense_out = np.zeros((len(dense_z), N), dtype=complex)
59      w_diff = 2*np.pi/(N*dt)*np.arange(-N/2, N/2)
60      w_diff = fftshift(w_diff)
61      w = w_diff + w0
62      hrw = fft(hr)
63      d = 0
64      for i, beta in enumerate(betas):
65          d += -1j*beta*w_diff**(i+2) / np.math.factorial(i+2)
66
67      def NA(A):
68          return fft(A*((1-fr)*np.abs(A)**2)
69                     + fr*dt*A*ifft(hrw*fft(np.abs(A)**2)))
70
```

```
71      def photon_number(A_w):
72          return np.sum(np.abs(A_w)**2 / w)
73
74      z_curr = 0
75      n_it = 0
76      for idx, z_target in enumerate(dense_z):
77          add_output = False
78          while z_curr < z_target:
79              if (z_curr + dz) > z_target:
80                  # Save suggested step size, which can be reused
81                  # for the step after this one
82                  dz_prev = dz
83                  dz = z_target - z_curr
84                  add_output = True
85              D = -alpha_func(z_curr) / 2 + d
86              K = -dz * 1j * gamma_func(z_curr)*(w/w0)
87
88              # save starting point for the case that the step fails
89              Aw0 = Aw
90              exp_D = np.exp(D * dz/2)
91              Aw_ip = exp_D * Aw
92              k1 = exp_D * K*NA(ifft(Aw))
93              k2 = K*NA(ifft(Aw_ip + k1/2))
94              k3 = K*NA(ifft(Aw_ip + k2/2))
95              k4 = K*NA(ifft(exp_D * (Aw_ip + k3)))
96              Aw = exp_D * (Aw_ip + k1/6 + k2/3 + k3/3) + k4/6
97
98              n_photons_start = photon_number(Aw0*np.exp(D * dz))
99              n_photons_end = photon_number(Aw)
100             error = (np.abs(n_photons_end - n_photons_start)
101                     / n_photons_start)
102             z_curr += dz
103             if error > 2 * tol:  # step failed
104                 z_curr -= dz
105                 dz /= 2
106                 Aw = Aw0
107                 continue
108             elif error > tol:
109                 dz /= 2**0.2
110             elif error < 0.1 * tol:
111                 dz *= 2**0.2
112
```

```
113             n_it += 1
114             if add_output:
115                 Aw_dense_out[idx, :] = Aw
116                 dz = dz_prev
117
118     return ifft(Aw_dense_out, axis=1), n_it
```